Photoacoustic Tomography Opening New Paradigms in Biomedical Imaging

Joon-Mo Yang and Cheol-Min Ghim

Introduction

Photoacoustic (PA) tomography (PAT), also known as optoacoustic tomography (OAT) or thermoacoustic tomography (TAT), is indeed an invaluable imaging technique that provides new opportunities in biomedical imaging (Xu and Wang 2006a; Wang 2008, 2009; Ntziachristos 2010; Beard 2011; Cox et al. 2012; Wang and Hu 2012; Mehrmohammadi et al. 2013; Yao and Wang 2014a; Nie and Chen 2014; Manohar and Razansky 2016; Weber et al. 2016; Gujrati et al. 2017; Deán-Ben et al. 2017b; Omar et al. 2019). Since its first image demonstration and seminal reports presented by Kruger et al. (Kruger 1994; Kruger and Liu 1994; Kruger et al. 1995) and Oraevsky et al. (Oraevsky et al. 1993; 1994a; Oraevsky et al. 1994b) in the mid-1990s, the technique has greatly advanced, and currently, it is awaiting full maturation as another major clinical imaging technique following conventional mainstream imaging modalities, such as ultrasound (US) imaging, X-ray computed tomography (CT), positron emission tomography (PET), and magnetic resonance imaging (MRI). This evaluation may not be an exaggeration because, among newly emerged imaging techniques after the advent of the aforementioned mainstream imaging techniques, PAT is currently the only imaging modality that permits high-resolution tomographic imaging even in depths of several centimeters. Although other types of imaging techniques (optical or not) (Denk et al. 1990; Helmchen and

J.-M. Yang (✉)
Center for Photoacoustic Medical Instruments, Department of Biomedical Engineering, Ulsan National Institute of Science and Technology, Ulsan, Republic of Korea
e-mail: jmyang@unist.ac.kr

C.-M. Ghim
Department of Physics, School of Natural Science, Ulsan National Institute of Science and Technology, Ulsan, Republic of Korea
e-mail: cmghim@unist.ac.kr

J. K. Kim et al. (eds.), *Advanced Imaging and Bio Techniques for Convergence Science*, Advances in Experimental Medicine and Biology,
https://doi.org/10.1007/978-981-33-6064-8_11

Denk 2005; Drexler and Fujimoto 2015; Boas et al. 2001; Cheney et al. 1999) have also been proposed and even their biomedical utilities have been successfully demonstrated in comparison to the aforementioned mainstream imaging techniques, their effective imaging depths—while conserving a high spatial resolution—do not match that of PAT.

In addition to the high-resolution deep imaging capability, another key feature of PAT is that it can provide a variety of different image contrasts based on the wide selectivity of the wavelength of an excitation laser beam, depending on the endogenous or exogenous contrast agents of interest. Based on this principle, PAT is capable of visualizing various anatomical structures or biological constituents, such as blood vessels (Wang 2009; Beard 2011; Wang and Hu 2012; Deán-Ben et al. 2017b; Omar et al. 2019) and cell nuclei (Yao et al. 2010a), without the aid of any contrast agent (i.e., only using a laser pulse). Moreover, a variety of physiological and functional information, such as the total hemoglobin concentration (Zhang et al. 2006a; Hu et al. 2011), oxygen saturation of hemoglobin (sO_2) (Zhang et al. 2006a; Hu et al. 2011; Yang et al. 2012a), and blood flow (Fang et al. 2007; Yao et al. 2010b), can also be imaged or measured by the endogenous contrast mechanism. In addition, by injecting an appropriate contrast agent, it is possible to produce additional exogenous contrasts, depending on the targeted biomolecule or biomarker of interest (Mehrmohammadi et al. 2013; Nie and Chen 2014; Weber et al. 2016; Gujrati et al. 2017). This wide range of degrees of freedom in contrast creation simply originates from the unique contrast mechanism that utilizes "optical absorption," which forms the core of PAT and makes it versatile. In recent years, the listed imaging capabilities of PAT have been more significantly recognized, as related systems can also be embodied in an integrated form with conventional US imaging, thereby complementing the limitations of US imaging.

After the completion of laying the cornerstones for PAT, such as in terms of the basic theory and instrumentation, major directions for the biological applications of PAT have also been roughly outlined over the previous two decades. Moreover, as has been made evident in recent multiple reports of clinical trials, several areas of clinical applications appear to be promising for their successful translations into actual practice if more specific roles or distinctive contributions are defined. For example, when it comes to biological applications, subjects related to brain imaging and cancer research are currently most popular, and when it comes to clinical applications, breast cancer diagnosis, and endoscopy or minimally invasive imaging applications are dominant in terms of the number of documented papers. Of course, on the basis of the aforementioned versatility of PAT, numerous other notable applications have also been proposed, and completely new concepts or applications that may form a new important area in the future continue to be presented.

In this chapter, we review the technology developments related to PAT in a chronological order for the following seven areas of biological and clinical applications: (1) small animal brain imaging, (2) small animal whole-body imaging, (3) cancer research, (4) breast cancer diagnosis, (5) dermatological applications, (6) endoscopy or minimally invasive imaging applications, and (7) angiography and lymphangiography, which were selected based on their dominancy in terms of the number of publications or their distinctive potentials evaluated subjectively by the

authors*. Thus far, a large number of review articles on PAT have been reported (Xu and Wang 2006a; Wang 2008, 2009; Ntziachristos 2010; Beard 2011; Cox et al. 2012; Wang and Hu 2012; Mehrmohammadi et al. 2013; Yao and Wang 2014a; Nie and Chen 2014; Manohar and Razansky 2016; Weber et al. 2016; Gujrati et al. 2017; Deán-Ben et al. 2017b; Omar et al. 2019). However, by reviewing the development histories of the selected areas in chronological order, it would be possible to obtain a certain sense or knowledge with regard to how such application areas have been developed thus far, how fast they have been evolving in recent years, and how they will evolve in the future. Thus, after explaining the basic principles and key imaging features of PAT, we retrace major events achieved over the past two decades and provide rough projections on the future appearances of PAT for the selected areas.

Principles

PAT is often compared to or regarded as a relative of conventional US imaging because it also produces an image by using acoustic waves as a signal mediating medium. However, the main feature of PAT lies in the use of a pulsed laser beam or electromagnetic wave with a duration of ~a few nanoseconds, which induces PA waves within the tissue to be imaged in accordance with the PA effect (Wang 2009; Manohar and Razansky 2016). Thus, unlike conventional US imaging, in which a tomographic image is produced by sending a short pulse of acoustic waves to a target tissue and then detecting some of the acoustic waves reflected from the tissue, PAT produces an image by sending a laser pulse to a target tissue first in order to induce PA waves and then capturing some of the induced PA waves approaching the US sensor that is pre-positioned around the tissue. Due to the distinctive imaging principle, PAT creates an image with a completely different type of image contrast as compared to conventional US imaging, as illustrated in Fig. 1a.

In terms of image contrast that is yielded, US imaging is a technique that maps the magnitude or amplitude of the echo waves that bounce back from each spatial point (but, mostly at a boundary), where the reflection intensity (R_I) is approximately proportional to the square of the spatial variation of the acoustic impedance Z [kg m^{-2} s^{-1} or rayl]—which is defined as the product of tissue density ρ [kg m^{-3}] and acoustic speed c [m s^{-1}] at a particular point (Fig. 1a). Thus, any boundary where acoustic impedance shows a sharp change appears as a hyperechoic region in the acquired image. In contrast, PAT maps the initial pressure distribution p_0 [N m^{-2} or Pa] induced by a deposited laser pulse, which eventually renders information on the spatial distribution of the optical absorption; this is typically represented by the absorption coefficient μ_a [cm^{-1}] and created by the presence of light-absorbing

*This chapter is an opinionated review on the development and prospects of photoacoustic tomography with a view to pedagogical practicality. It has never meant to be comprehensive in scope or authoritative in any way. Rather, we start with fundamental concepts and principles underlying the state-of-the-art technologies, from which selected achievements are reviewed along the chronological progression of the field with an emphasis on the potential breakthrough innovations.

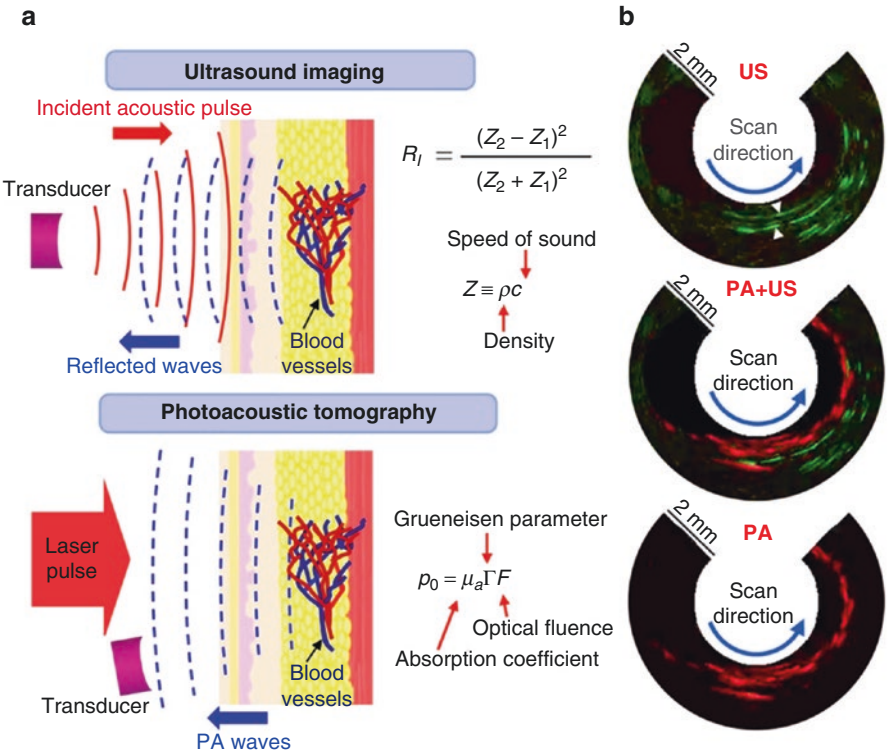

Fig. 1 Comparison of PAT and US imaging. (**a**) Principles of US imaging (upper) and PAT (lower). (**b**) A set of co-registered PA (top), US (bottom), and their combined (middle) images acquired from a rat intestine in vivo using a single-element focused US transducer-based mechanical scanning PA and US dual-modality endoscopic probe (Yang et al. 2012a). These images showcase the contrast difference between the two imaging modalities. During mechanical scanning (see the denoted scanning direction), laser pulses and acoustic pulses were fired radially in turn; subsequent response signals (i.e., PA waves and US echo waves) were captured by a single-element focused US transducer. Note that the US image (top) more clearly visualized the boundary of the rat intestine (see the white arrow heads), whose thickness was less than 500 μm, whereas the PA image visualized the blood vessels distributed inside the intestine wall

biomolecules—that is, chromophores. According to the PAT theory, the initial PA pressure distribution induced at a specific point right after a laser pulse deposition is proportional to the product of the optical fluence and absorption coefficient of the point (Wang 2009; Beard 2011; Cox et al. 2012; Manohar and Razansky 2016). Thus, if the optical fluence is known, which is occasionally assumed to be uniform over an imaged region, the spatial distribution of not only the absorption coefficient but also the gross concentration of chromophores can be recovered in image form.

Due to the explained contrast difference, if, for example, an intestine is imaged using the two techniques, US imaging would more clearly visualize the boundary profile of the intestine wall, whereas PAT would visualize the blood vessels within, as blood is a dominant light absorber (Fig. 1b).

Sending Laser Pulses to Target Tissue in Order to Generate PA Waves

When a target tissue is irradiated by a pulsed laser beam, whether it is focused (Fig. 2a) or broadly (Fig. 2b) illuminated at the surface, the photons carried in the beam are quickly diffused and de-correlated after traveling ~one transport mean free path (l_t') (typically ~1 mm) in the tissue due to the strong scattering nature of biological tissues (Welch and van Gemert 2011). Thus, if we consider the optical fluence $\Phi(r)$ [J/cm^2]—which is defined as the total number of photons (i.e., energy) passing a unit area regardless of the flow directions and over a period of time—at position (r), which is much deeper than the transport mean free path (l_t') from the tissue surface, it shows a broad distribution rather than a localized one (Figs. 2a and b) (Welch and van Gemert 2011). Such a deep region is referred to as a diffusion regime, while the shallow one less than

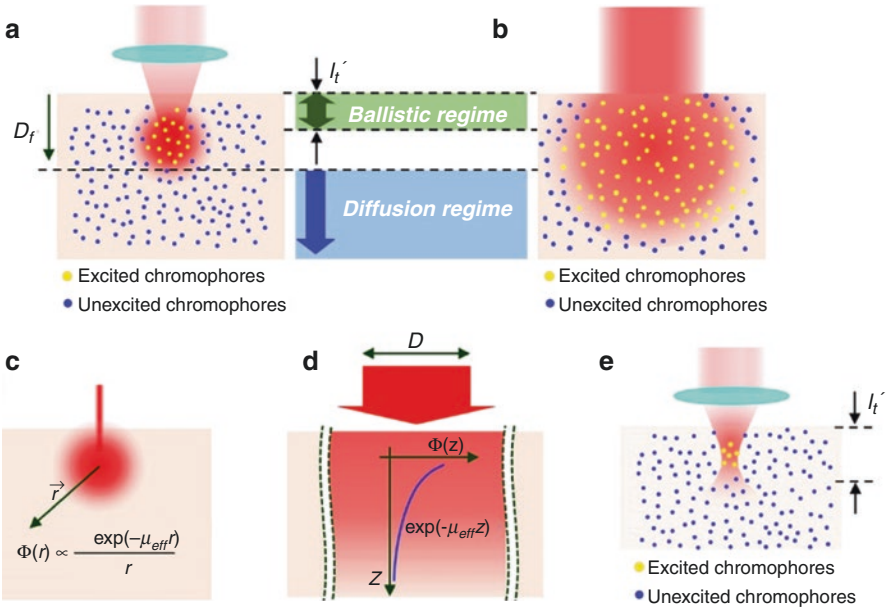

Fig. 2 Depiction of light delivery into a biological tissue and typical optical excitation mechanisms of PAT. Illustrations present the excited chromophores by a focused optical illumination (**a**) and broad optical illumination (**b**). As depicted in (**a**), if the location (D_f) of an aimed optical focus is deeper than one transport mean free path (l_t'), it is impossible to achieve a tight focus by only employing a traditional objective; this is due to the strong light scattering of biological tissues. Note that in (**a**) and (**b**), all the chromophores covered by the optical illumination (i.e., depicted in yellow) generate PA waves. In numerous AR-PAM and PACT systems, a broad optical illumination scheme as that depicted in (**b**) is typically employed. (**c**) Approximate fluence distribution ($\Phi(r)$) for an infinitely narrow beam (i.e., pencil beam), which is incident onto a semi-infinite homogenous medium. (**d**) Approximate fluence distribution ($\Phi(z)$) for a laser beam with an infinitely large beam diameter (i.e., $D \rightarrow \infty$) impinging onto a semi-infinite homogenous medium. (**e**) An illustration depicting excited chromophores (i.e., depicted in yellow) within the focal spot of a focused laser beam. This illumination scheme is typically utilized for OR-PAM

$l_t^{'}$ is referred to as a ballistic regime. In PAT, this implies that all and only the light absorbers included in the illumination zone can generate PA signals in proportion to the optical fluence ($\Phi(r)$) (Fig. 2). Of course, although the PA signal generation in a diffusion regime cannot be localized, PAT can still achieve adequate spatial resolution (the method for achieving this resolution is explained later).

Here, the prediction of exact optical fluence distribution at large depths is not simple if the tissue is complex (i.e., inhomogeneous), and it becomes tougher as the depth of the point under consideration increases because the total number of possible paths of photons that reach the point also increases proportionally. Applying a Monte Carlo simulation (Welch and van Gemert 2011) would be the best option for the prediction, although it is necessary to have a set of data on the optical properties of the tissue. Otherwise, one can use a diffusion approximation (Welch and van Gemert 2011) if the area of interest is located much deeper than the ballistic regime; moreover, the optical properties of the tissue can be assumed to be macroscopically homogenous. According to the diffusion theory, the optical fluence ($\Phi(r)$) at large depths ($>> l_t^{'}$) in a semi-infinite homogenous medium for the illumination with an infinitely narrow beam (Fig. 2c) roughly follows the distribution expressed in Eq. (1); it approaches that expressed in Eq. (2) as the beam diameter (D) increases (Fig. 2d), where μ_{eff} represents the effective attenuation coefficient and is defined as $\mu_{eff} \equiv \sqrt{3\mu_a\left(\mu_a + \mu_s^{'}\right)}$ (for more precise mathematical expression, refer to ref. (Welch and van Gemert 2011).

$$\Phi(r) \propto \frac{\exp\left(-\mu_{eff} r\right)}{r} \tag{1}$$

$$\Phi(z) \propto \exp\left(-\mu_{eff} z\right) \tag{2}$$

Thus far, we have discussed the light delivery mechanism in large depths. However, if the targeted area is located in a shallow area—that is, less than ~one transport mean free path—tight focusing of a laser beam can still be achieved, as illustrated in Figure 2e. In this case, by appropriately adjusting the incident pulse energy, one can create a condition in which PA waves with a detectable magnitude are only induced within the focal spot where the optical fluence is the highest. In fact, a related concept is applied to optical resolution PA microscopy (OR-PAM) (Maslov et al. 2008), which is explained later, to achieve a typical optical microscopy-level lateral resolution.

Detecting PA Waves to Produce an Image

Once a short laser pulse is absorbed by chromophores, it causes a temperature rise on account of instant heating, and the thermal energy is converted into PA waves that propagate omni-directionally rather than travel toward a specific direction (e.g., the original laser beam propagation direction); this is because monopole radiation is

dominant during the generation of PA waves (Wang 2009). According to the PAT theory, the center frequency of the generated PA waves is inversely proportional to the time duration of the deposited laser pulse. Thus, the shorter the duration, the wider and higher the bandwidth and frequency (refers to ref. (Wang 2009) for the mathematical formalism). Moreover, the propagation of the PA waves can be mathematical modeled by the same wave equation that is typically utilized for US imaging, in which the speed of sound for soft tissues is usually assumed to be constant (~1.55 mm/μs at room temperature). Then, some of the PA waves that approach the US transducer placed near the target object are captured by the transducer and converted into an image.

Due to the involvement of the conventional US technique, although the irradiated laser beam does not focus on a deep tissue region, PAT can still achieve an adequate spatial resolution by ultrasonically resolving the locations of PA signal sources. Of course, considering the time duration of the deposited laser pulse, which is typically in a nanosecond range, the initial PA waves generated immediately after the optical excitation include broad frequency components (sub to hundreds MHz). However, in reality, only a partial frequency range is detected by the employed transducer due to its limited bandwidth characteristics as well as the frequency-dependent acoustic attenuation during wave propagation. Hereafter, several methods for localizing the origins of PA signals are explained, with illustrations in Fig. 3.

The first method is to use a single-element US transducer, in which any type of transducer—that is, either focused or unfocused—could be employed. However, in order to avoid a complex image reconstruction process, like the computed tomographic reconstruction, a focused US transducer is more frequently adopted in numerous PAT systems. For example, although the imaged area is located much deeper than the ballistic regime, such a focused US transducer can easily achieve an adequate lateral resolution by excluding all the PA signals approaching from its off-axial points, which can be attributed to the benefit of the geometrically curved surface (Fig. 3a). Consequently, in this case, the lateral resolution is entirely determined by the acoustic parameters of the employed US transducer and it is known to be inversely proportional to the product of the center frequency and acoustic numerical aperture (NA).

On the other hand, if the imaged area is limited to the ballistic regime (i.e., less than ~1 mm), it is possible to induce PA waves only within the focal spot of a laser beam by appropriately adjusting its pulse energy, as previously mentioned (Fig. 2e). In this case, irrespective of the employed acoustic beam diameter of a US transducer, which is usually wider than that of the focused laser beam, the lateral resolution of the related PAT system is determined by the beam diameter of the optical focus rather than the acoustic beam diameter of the employed transducer (Fig. 3b). Consequently, the optical parameters of the illumination optics, such as the wavelength and optical NA, determine the lateral resolution of the system and, thus, a typical optical microscopy-level lateral resolution (i.e., ~a few micrometers) is achievable by applying this principle.

In fact, the two imaging concepts were applied for the first time in the acoustic-resolution PA microscopy (AR-PAM) and OR-PAM systems reported by Maslov

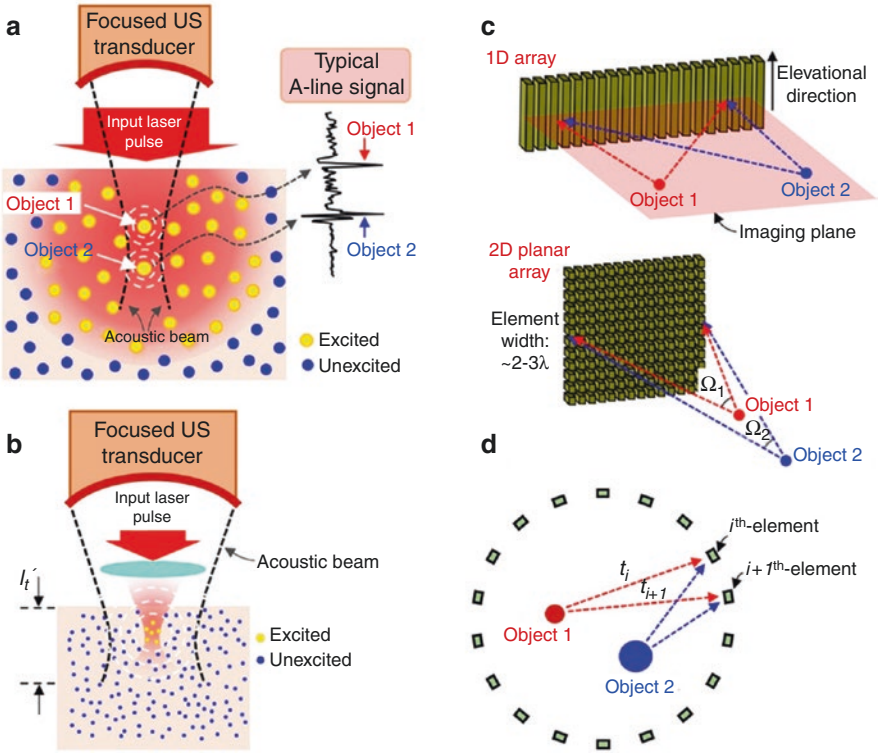

Fig. 3 Typical US signal detection mechanisms in PAT. (**a**) Single-element focused US transducer-based signal detection mechanism typically utilized in AR-PAM. Note that although all the chromophores within the optical illumination zone generate PA signals, only those chromophores located within the acoustic beam axis and the acoustic depth of focus exert a detectable pressure to the US transducer. (**b**) A single-element focused US transducer-based signal detection mechanism typically utilized in OR-PAM. Note that only the chromophores within the optical focus, which is much narrower than the waist of the acoustic beam, generate PA signals, and the optical and acoustic foci must overlap with each other. (**c**) 1D (upper) and 2D (lower) planar array transducer-based signal detection mechanisms, in which optical excitation laser beams are not depicted. Note that Ω_1 is larger than Ω_2. (**d**) Ring array transducer-based signal detection mechanism. t_i denotes the arrival time of the pressure wave originating from Object 1 to i^{th}-element. Note that t_{i+1} is greater than t_i. The depicted signal detection configuration can also be achieved by performing a circular mechanical scanning using a single-element US transducer

et al. of the Wang group in 2005 (Maslov et al. 2005) and 2008 (Maslov et al. 2008), respectively. However, unfortunately, irrespective of whether the optical focusing is employed, the axial resolutions of the AR- and OR-PAM are both determined by the acoustic parameters of an employed US transducer, as the performances are achieved based on the acquired time-resolved signals (see the typical A-line signal presented in Figure 3a). Thus, the axial resolution has an inverse relationship with the product of the center frequency and bandwidth of an employed US transducer—that is, the greater the product, the better the axial resolution.

Although the use of such a focused US transducer can benefit the lateral resolving power, in order to produce an image, both the OR- and the AR-PAM require a mechanical scanning mechanism—for example, raster scanning, because the US transducer can detect only the one-dimensional (i.e., A-line) signal that is localized along the acoustic axis. Consequently, the data acquisition (DAQ) process must be repeated by changing the location of signal detection after each laser pulse firing, which is a time-consuming process. Nevertheless, numerous OR- and AR-PAM systems still adopt the single-element focused US transducer-based mechanical scanning mechanism because they can be implemented more economically compared to an array transducer-based detection mechanism, which is explained next.

The second method for spatially resolving the origins of detected PA signals is to use an array transducer in which a number of piezoelectric elements or its equivalent are arranged in a 1D linear or 2D planar fashion (Fig. 3c). The key advantage of this mechanism is that an array transducer can capture multiple A-line signals simultaneously after firing a single laser pulse only. This implies that it is possible to acquire a two- or three-dimensional image—which is only determined by the spatial configuration of an employed array transducer—at every laser pulse firing process, thereby requiring no additional mechanical scanning process. Consequently, the frame rate for a 2D cross-sectional or 3D volumetric imaging is usually limited by the pulse repetition rate (PRR) of an employed laser system. Nevertheless, it can virtually reach or even exceed the real-time imaging speed of 30 Hz, although the related system cost increases proportionally to the number of channels due to the high cost of the array transducer and parallel DAQ system.

Here, it must be noted that, although a single-element US transducer is mostly employed in a mechanical scanning PAT system, if the employed transducer is unfocused and if its aperture has a size that is slightly larger than the center wavelength of the transducer, the recorded PA data set at multiple different locations renders an almost equivalent effect as that in the case of employing an array transducer with the same center wavelength. Of course, in this discussion, we ignore the fact that the mechanical scanning requires a much larger number of laser pulses as well as the corresponding amount of scanning time. Nevertheless, there is an equivalency because an array transducer could be understood as the spatial iteration of the same type of single-element US transducer. In fact, Wang et al. demonstrated the first in vivo PA imaging for a rat brain by applying a similar concept in 2003 (Wang et al. 2003), even though an array transducer-based PAT system was not available at that time. Figure 3d illustrates the geometric configuration of a ring-type array transducer, although an equivalent data set also could be acquired using a single-element transducer in accordance with the method explained above.

However, irrespective of the method utilized, a sophisticated image reconstruction algorithm must be applied to resolve objects in the imaged area, because each A-line signal is captured at a position by an element in an array transducer or by an unfocused US transducer does not include any information on its angular origin. Only the arrival time of each spike is resolvable in a recorded 1D data set (i.e., no resolving power along a transverse direction because all signals are mixed into a 1D signal). Nevertheless, by employing such an image reconstruction algorithm, an

adequate lateral resolution can be achieved, because the presence of an object in a reconstructed image is eventually unveiled by the cumulative projection effect of the PA signals included in a corresponding time point in the A-line signal acquired at each detection position. Note that, as depicted in Figure 3c and d, the arrival time of PA waves originating from a point object (e.g., Object 1) to each transducer element shows a gradual variance due to the corresponding variation of the distance between them (in relation to this principle, it is helpful to refer to ref. (Beard 2011).

In PAT, such an image reconstruction method is usually referred to as a back projection algorithm, which forms the theoretical basis of PA-computed tomography (PACT). Note that this principle is similar to the well-known beam forming process of a phased array transducer in conventional US imaging. In addition to the back projection, other image reconstruction algorithms or concepts—such as time-reversal reconstruction and synthetic focusing (Wang 2009)—are also presented, although the underlying principles are the same.

In the case of a PACT system that employs 1D linear or 2D planar array transducers, as depicted in Figure 3c, it must also be noted that the lateral resolution is usually degraded as the target distance increases because the solid angle subtended by a point object to the entire array elements decreases: in other words, the effective acoustic NA created by the synthetic aperture decreases. The related issue is known as the "limited-view problem," as with the case of conventional US imaging; thus, most of the array transducers with such a limited span area suffer from a similar issue. Thus, in order to achieve a better lateral resolution, the effective acoustic NA must be maximized by increasing the span dimension and the number of array elements, although it is not always possible due to the allowed probe dimension and the correspondingly increasing device cost.

On the other hand, if PA signals are captured by such a ring array transducer or its equivalent—such as the circular-scan 2D PACT imaging, as illustrated in Figure 3d—there is no limited-view problem at least within the detection plane; thus, the in-plane resolution can be almost constant over the imaged area (Li et al. 2017). In this case, like the axial resolution of a single-element US transducer, it approximately has an inverse relationship to the product of the center frequency and bandwidth of the array transducer.

Thus far, we have explained the general principles of PAT. However, before moving to the main part, we briefly review the key imaging features and attainable performances of PAT in terms of the five technical elements—that is, the contrast, imaging depth, resolution, imaging speed, and safety—all of which are importantly evaluated as core factors for an imaging technique to be accepted as a viable biomedical imaging technique.

Contrast

The contrast of an imaging technique is the aspect that represents what kind of image information can be provided by the technique and also accounts for the reason why the technique is necessary as another imaging modality in biomedical

imaging. In such an aspect, PAT has a great versatility based on the unique contrast mechanism of the optical absorption and due to which huge possibilities in creating a variety of different image contrasts are provided. In conventional US imaging, for example, available contrast mechanisms are almost fixed and they all basically rely on the reflectivity of acoustic waves. Thus, although the frequency (or wavelength) of an acoustic pulse changes, it does not affect the produced image contrast but only the spatial resolution and penetration depth. However, in PAT, the change in frequency (i.e., wavelength) of a laser beam implies the creation of a different image contrast.

In biological tissues, there are a large number of biomolecules (i.e., chromophores) that absorb light and have their own absorption spectra with different spectral behavior. Figure 4a represents absorption spectra of related examples, such as oxy- or deoxy-hemoglobin (i.e., HbO_2, HbR), DNA and RNA, melanin, lipid, bilirubin, myoglobin (Mb), and water. Thus, if one selects an appropriate laser wavelength considering the absorption peaks of a specific chromophore of interest, it is possible to selectively visualize the spatial distribution of the chromophores by using only the laser pulse. Indeed, this is the key principle spanning the endogenous contrast mechanism of PAT; thus far, actual imaging demonstrations for the mentioned chromophores and other biological constituents, such as methemoglobin, cytochrome *c*, and glucose, have been presented in multiple papers (Yao et al. 2010a; Zhang et al. 2006a, 2011, 2013; Hu et al. 2011; Yang et al. 2012a; Viator et al. 2004; Allen et al. 2012; Wilson et al. 2014; Zhou et al. 2012; Lin et al. 2016; Xu et al. 2010; Tang et al. 2015a; Kottmann et al. 2012; Pleitez et al. 2013).

Notably, since hemoglobin is the core composition of a blood vessel, its presence is usually revealed as a form of vasculature image when a PA imaging is performed for in vivo biological tissue. Moreover, if one harnesses the different absorption properties of oxy- and deoxy-hemoglobin (Fig. 4a), it is also possible to acquire a map of oxygen saturation of hemoglobin (sO_2) based on multiwavelength imaging (Fig. 4b), which constitutes the core of PAT functional imaging. In a similar manner, there have also been reports that demonstrated the visualization of other anatomic structures or biological constituents, such as cell nuclei (Yao et al. 2010a), tissue hydration (Xu et al. 2010), lipid (Allen et al. 2012; Wilson et al. 2014), and nerve (Matthews et al. 2014; Li et al. 2016). In addition, it is also possible to acquire additional physiological and functional information such as blood flow (Fang et al. 2007; Yao et al. 2010b), temperature (Larina et al. 2005; Shah et al. 2008; Pramanik and Wang 2009; Landa et al. 2019), and metabolism (Wang 2008; Hu et al. 2011; Pleitez et al. 2020; Ntziachristos et al. 2019).

The above examples are cases that are all achievable by the endogenous contrast mechanism. However, by using (i.e., administrating) an appropriate contrast agent to target or label the specific molecule or biomarker of interest (Mehrmohammadi et al. 2013; Nie and Chen 2014; Weber et al. 2016; Gujrati et al. 2017), it is also possible to produce additional exogenous image contrasts for numerous important anatomical structures and markers, such as the lymphatic system (Yang et al. 2012a; Song et al. 2008), amyloid-β (Hu et al. 2009b), integrin $\alpha_v\beta_3$ (De la Zerda et al. 2008), epidermal growth factor receptor (EGFR) (Hudson et al. 2014), and reporter

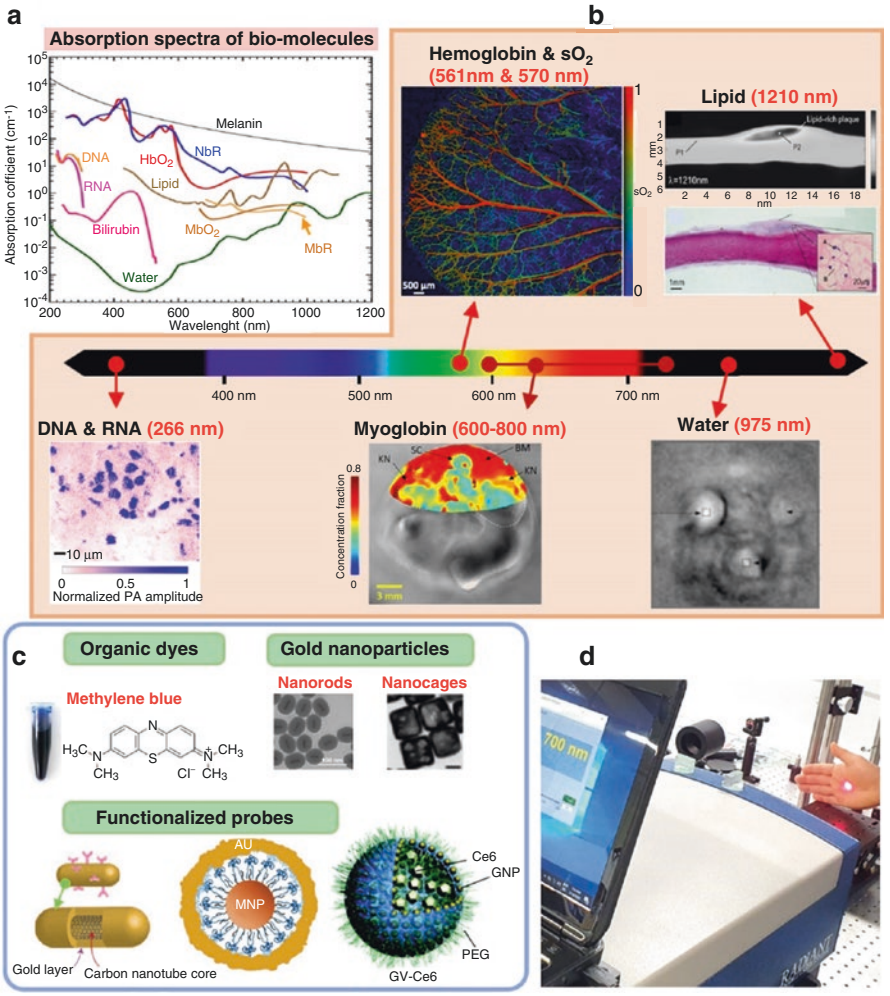

Fig. 4 Examples of available image contrasts in PAT. (**a**) Absorption spectra of various chromophores (Yao and Wang 2014a). (**b**) Examples of PAT images acquired based on the endogenous contrast mechanism (Yao et al. 2010a; Hu et al. 2011; Allen et al. 2012; Lin et al. 2016; Xu et al. 2010). The hemoglobin and sO_2 maximum amplitude projection (MAP) image were acquired from a mouse ear using dual-wavelength laser beams. (**c**) Examples of contrast agents applicable for PAT to produce exogenous image contrasts (Chen et al. 2011; Yang et al. 2007; Kim et al. 2009; Jin et al. 2010; Lin et al. 2013). Note that the presented images are very few examples of PA contrast agents developed thus far (for more detailed information, refer to refs. (Mehrmohammadi et al. 2013; Nie and Chen 2014; Weber et al. 2016; Gujrati et al. 2017). (**d**) A photo showing a human hand directly exposed to a 700-nm laser beam with an energy of 20 mJ and a beam diameter of ~6.5 mm (operating at the PRR of 20 Hz), which yields an approximate optical fluence of 60 mJ/cm^2 for a single laser pulse on the surface of the skin (note that although this value is three times greater than that of the ANSI safety limit, there was no damage to the skin)

genes (Brunker et al. 2017). Thus far, a variety of contrast agents or molecular probes have been developed for the purpose (Mehrmohammadi et al. 2013; Nie and Chen 2014; Weber et al. 2016; Gujrati et al. 2017), and Figure 4c presents a few examples of related contrast agents, which can be roughly classified as organic dyes, nanoparticles (Chen et al. 2011; Yang et al. 2007), and functionalized probes (Kim et al. 2009; Jin et al. 2010; Lin et al. 2013; Huynh et al. 2015). Related to the physiological or functional imaging of PAT, there were also reports that demonstrated a pH mapping in phantoms (Chatni et al. 2011) and tumors (Jo et al. 2017) by using a pH-sensitive fluorescent dye (SNARF-5F carboxylic acid). Moreover, in 2017, Knox et al. of the Chan group presented a novel N-oxide-based probe (named HyP-1) developed for PAT imaging of hypoxia in ischemia and cancer (Knox et al. 2017).

Of course, it might be a general situation that there are several different types of chromophores that are distributed over a region of interest rather than only a single type that exists independently. Although such a situation occurs, PAT can differentiate the spatial distribution of each chromophore by applying the spectral unmixing technique in which multiple wavelength imaging is performed to separate out the necessary information only. As presented, PAT has a wide range of freedom in creating contrasts, which must be importantly evaluated as the core aspect of how PAT can complement conventional US imaging if the two techniques are combined in a single imaging system.

Imaging Depth

Adding to the unique contrast mechanism, PAT's deep imaging capability is another important aspect that highlights its technical value. Although PAT is openly classified as an optical imaging modality owing to the use of a pulsed laser illumination, its imaging depth can reach up to several centimeters, thereby overtaking the well-known, ballistic optical imaging modalities—such as confocal microscopy (CFM) or two-photon microscopy (TPM) (Denk et al. 1990; Helmchen and Denk 2005) and optical coherence tomography (OCT) (Drexler and Fujimoto 2015)—by also being able to employ diffused light as an energy deliverer to deep tissues.

Thus, if deep imaging is the major goal of a PAT system, like the case of a PACT system, more care must be given to achieve an effective light energy delivery to deep tissues because only those chromophores covered by an optical illumination can generate PA waves, as explained earlier (Figs. 2a and b). Of course, employing a US transducer with a better sensitivity is also important. However, the maximum imaging depth of a PAT system is more affected by the light illumination parameters because, due to the highly scattering and light-absorbing nature of biological tissue, the optical fluence distribution ($\Phi(r)$) of photons within a biological tissue shows a sharper decay than the amplitude of the acoustic waves propagating in biological tissue. For example, acoustic waves with a center frequency of 3 MHz have an acoustic penetration depth of approximately 2.9 cm for soft tissue, like muscle, whereas photons with a wavelength of 720 nm, at which the penetration is highest,

have an optical penetration depth of only 0.57 cm (here, the penetration depth was defined as $1/\mu_{eff}$).

Of course, a deeper imaging could be achieved by exciting a target surface with a higher laser pulse energy. However, the achievable maximum imaging depth does not have a simple linear relationship to the input energy; moreover, the associated safety issue, which is presented later, must be considered. Thus far, a penetration depth of ~4 cm has been demonstrated in actual female breasts and a male prostate in vivo by broadly illuminating a target region while regulating the maximum permissible exposure (MPE)—that is, 20 mJ/cm^2 (Kruger et al. 2010, 2013; Lin et al. 2018; Kothapalli et al. 2019).

Resolution

As explained earlier, spatial resolutions of typical AR-PAM and PACT are mostly determined by the three acoustic parameters—that is, center frequency, bandwidth, and acoustic NA (or viewing angle)—of an employed US transducer because the two techniques employ a broad optical illumination to achieve deep imaging. In accordance with the principle, the first AR-PAM system achieved an axial resolution of ~15 μm and a lateral resolution of ~45 μm by employing a 50-MHz transducer with an acoustic NA of 0.44 and a fractional bandwidth of 70% (Maslov et al. 2005), which provides a rough estimation for the resolution performance of other AR-PAM systems. In the case of a circular-scan PACT system, implemented based on either a single-element transducer or ring array transducer, its in-plane resolution exhibits an isotropic and quasi-uniform performance (Li et al. 2017; Razansky et al. 2011), provided that the total viewing angle created by an entire scan is greater than ~180° (Razansky et al. 2011) and is typically at a hundreds-of-micrometers level.

The lateral resolution of a typical OR-PAM system is in the range of sub-microns to a few microns, whereas the axial resolution has a larger value, like a few ten microns (in general, >15 μm) (Hu et al. 2011; Maslov et al. 2008; Zhang et al. 2010). Thus, in order to overcome this limitation, several new concepts—such as the use of an even higher frequency US transducer (e.g., 125 MHz) (Zhang et al. 2012) and the capitalization of the Grueneisen effect (Wang et al. 2014a; Ma et al. 2016)—have been proposed since 2012, which eventually further dragged down the axial resolution to 2.3–12.5 μm. Similarly, in order to push the lateral resolution limit of OR-PAM, a few studies considered the nonlinear effects in the PA wave generation (Danielli et al. 2014; Yao et al. 2014) or harnessed the Grueneisen effect along with the use of dual-laser pulses with different wavelengths, etc. (Shi et al. 2019).

Moreover, since 2015, multiple reports have been presented to achieve a PA super-resolution imaging even in an optical diffusion regime, in which the spatial resolution is known to be limited by the acoustic diffraction of an employed US transducer (Conkey et al. 2015; Chaigne et al. 2016; Chaigne et al. 2017; Murray et al. 2017; Vilov et al. 2017; Deán-Ben and Razansky 2018). Eventually,

sub-acoustic spatial resolutions were achieved by applying the concepts of exploiting a PA feedback for wave front optimization (Conkey et al. 2015), multiple speckle illumination (Chaigne et al. 2016), temporal PA signal fluctuations caused by the dynamics of flowing absorbers (Chaigne et al. 2017), optical speckle pattern-aided structured illumination (Murray et al. 2017), PA signal localization based on injected microbeads (Vilov et al. 2017; Deán-Ben and Razansky 2018), etc.

Imaging Speed

As with conventional US imaging, PAT is classified as a real-time imaging modality. Although a single-element US transducer-based mechanical scanning PAT system requires a relatively longer scanning time due to the involvement of a point or raster scanning mechanism, an array transducer-based state-of-the-art PAT system—in which a simultaneous signal capturing is possible—can easily achieve a real time (~30 Hz) or even higher imaging speed provided that an employed laser system permits corresponding PRR (Li et al. 2017; Deán-Ben et al. 2017a). For example, in a report presented by Deán-Ben et al. of the Razansky group in 2017 (Deán-Ben et al. 2017a), a 100-Hz frame rate was achieved even for performing volumetric imaging by employing a 510-element hemispherical matrix array transducer.

In the case of OR-PAM, although there were a few exceptions (Song et al. 2011; Li et al. 2013; Xia et al. 2013), most related embodiments have been embodied based on single-element US transducer-based mechanical scanning mechanisms, which inherently require a relatively longer scanning time than that of an AR-PAM system, as it requires much denser scanning steps. In fact, in the first OR-PAM system reported in 2008 (Maslov et al. 2008), in which a stepper motor was employed, its B-scan imaging could be performed only at ~1.3 Hz for a 1-mm scan range with a step size of 1.25 μm. However, in the demonstration presented in ref. (Lan et al. 2018), a B-scan imaging speed as high as 900 Hz was achieved for a much wider scan range (12 mm) by utilizing a fast rotating hexagonal mirror-based mechanical scanning mechanism.

As shown, the imaging speed of a mechanical scanning PAM system is mostly affected by the employed scanning mechanism; thus, the speed could be further increased by employing a more advanced scanning mechanism. However, it must be noted that there is a fundamental limitation on the maximum imaging speed. Unlike pure optical imaging techniques, PAT requires a much longer gate time to capture all the PA signals necessary to cover a desired imaging depth. Note that the speed of sound in biological tissues is merely ~1.55 mm/μm, whereas the tissue penetration time of a fired laser beam is almost negligible. Consequently, if the distance between the detector and a tissue sample increases or the total depth to be imaged increases, a corresponding amount of time is required to wait for all the arrivals of necessary signals. Nevertheless, it is true that the theoretical imaging speed of PAT could be approximately twice as fast than that of US imaging because, unlike US imaging, PAT only involves one-wave propagation of acoustic waves.

Safety

In the inception of PAT, there was a concern regarding the safety issue, as PAT utilizes a nanosecond level pulsed laser radiation in which its instant peak power is extremely high, although its average power is within a reasonable range. In fact, one may also encounter a situation in which a laser beam emitted from a laser head generates a strong sound when it directly hits the surface of a metallic object, such as optical table. Although the sound is rather frightening, like that of linagraph paper, it is not a general case but a rather exceptional one, because metal is a conductive material in which numerous free electrons are included and the incident laser beam is coherent and polarized. Thus, unlike such a conductive material, no damage occurs when it is incidental on a biological tissue surface, as it is closer to a dielectric material than a conductive material; moreover, a laser beam incident on tissue is quickly diffused and de-correlated, losing its original polarization after traveling a few transport mean free paths. Figure 4d presents a human hand directly exposed to an unexpanded 760-nm laser beam with a single pulse energy of 20 mJ and beam diameter of 6 mm (operating at 20 Hz PRR). More importantly, it must also be noted that the energy of a single photon in the visible range, where PAT is typically performed, is in the range 1.6–3.3 eV, which is much less than that of X-ray radiation and, thus, makes PAT fall into a nonionizing imaging modality.

In conclusion, if the intensity of the laser beam is well regulated within a safety limit, it does not cause any tissue damage. Currently, related safety for a nanosecond laser is guided by the ANSI standards in terms of the MPE and the mean irradiance (Laser Institute of America 2007). Thus, in the spectral region of 400–700 nm, the MPE on the tissue surface must not exceed 20 mJ/cm^2, whereas it becomes looser as the wavelength increases and can go up to even 100 mJ/cm^2 at 1050 nm. In addition, if the same area is exposed to a laser beam for over 10 s, the mean irradiance must not exceed 200 mW/cm^2 in the visible and 1 W/cm^2 in the NIR. Nevertheless, complying with the safety guideline, a PA signal detection even from a depth of ~4 cm has been demonstrated in an actual human subject (Kruger et al. 2010; 2013; Lin et al. 2018; Kothapalli et al. 2019), as previously mentioned.

Biological Applications

Reviewing the initial papers of PAT, it is evident that the PAT technology originally emerged to mainly target several clinical applications, such as breast imaging, dermatological applications, and endoscopy (Oraevsky et al. 1994b; Esenaliev et al. 1997; Oraevsky et al. 1997). Although the related research outcomes reported to date have been very successful, most of them are still ongoing, whereas PAT has already successfully demonstrated its utility in various biological applications, as many of the systems developed for these applications were already commercialized. Thus, in this section, we introduce the development histories of PAT biological applications in three main subjects: (1) brain imaging, (2) small animal whole-body imaging, and (3) cancer research.

Brain Imaging

The brain imaging application of PAT was the subject where the in vivo imaging capability of PAT was first demonstrated in 2003 by Wang et al. of the Wang group (Wang et al. 2003). Currently, the related research activities account for one of the most active and rapidly advancing research subjects of PAT. Although the earlier works reported in the mid-1990s by Kruger et al. and Oraevsky et al. demonstrated the feasibility of PAT's in vivo imaging, their studies were limited to phantom or ex vivo animal studies (Kruger 1994; Kruger and Liu 1994; Kruger et al. 1995; Oraevsky et al. 1993; Oraevsky et al. 1994a; Oraevsky et al. 1994b). However, after the in vivo imaging capability of PAT was clearly demonstrated (Wang et al. 2003), the entire area of PAT, as well as the brain imaging application, has begun to grow in earnest. In addition, the report presented several prototypical experimental demonstrations that suggested that PAT could be further developed as a new tool for both functional and structural imaging.

Figure 5a depicts the system that they utilized for the experiment. They guided a 532-nm laser beam from a Q-switched Nd:YAG laser to the central zone of a rat brain, where the scanning axis of a single-element US transducer (3.5 MHz) was also set to perform a rotational scanning around the animal head. Thus, after the firing of each laser pulse, the transducer detected PA waves at a certain distance apart from the brain and achieved a full 360° scanning that included 240 steps of the employed stepper motor (~16 min was required for one full scanning due to a signal averaging at the given 10-Hz pulse PRR of the employed laser system).

By performing a circular mechanical scanning under the orthogonal configuration between the laser illumination and acoustic detection, they could acquire the first in vivo image of a rat brain. In particular, after applying physical stimulations to left and right whisker of a rat, they successfully mapped the corresponding hemodynamic responses of the rat brain via the intact scalp and skull, as depicted in Figure 5b. At that time, the removal of both or at least one of the scalp and skull layers was typical in numerous optical microscopies. Moreover, they were also able to capture a blood volume increase in accordance with the alteration of the oxygen level from hypoxia to hyperoxia in the inhaled gas.

Although the experiments were performed in a water tank to provide acoustic matching between the brain and US transducer, the study was the first case that demonstrated the functional brain imaging capability of PAT by applying the circular-scanning PACT concept. After the in vivo demonstration, the same PACT concept presented in Figure 5a, or its modified versions, were continuously applied to most of the PAT brain imaging studies reported by the Wang group until ~2010, except one case that imaged a Rhesus monkey brain ex vivo by replacing the Q-switched laser source with a 3-GHz microwave source, as reported by Y. Xu et al. in 2006 (Xu and Wang 2006b). The following account describes several notable outcomes reported in the period.

In 2004, the first in vivo imaging demonstrator, Wang et al. presented another report that applied several exogenous contrast agents, such as indocyanine green (ICG) polyethylene glycol (Wang et al. 2004b), and Y. Wang et al. applied

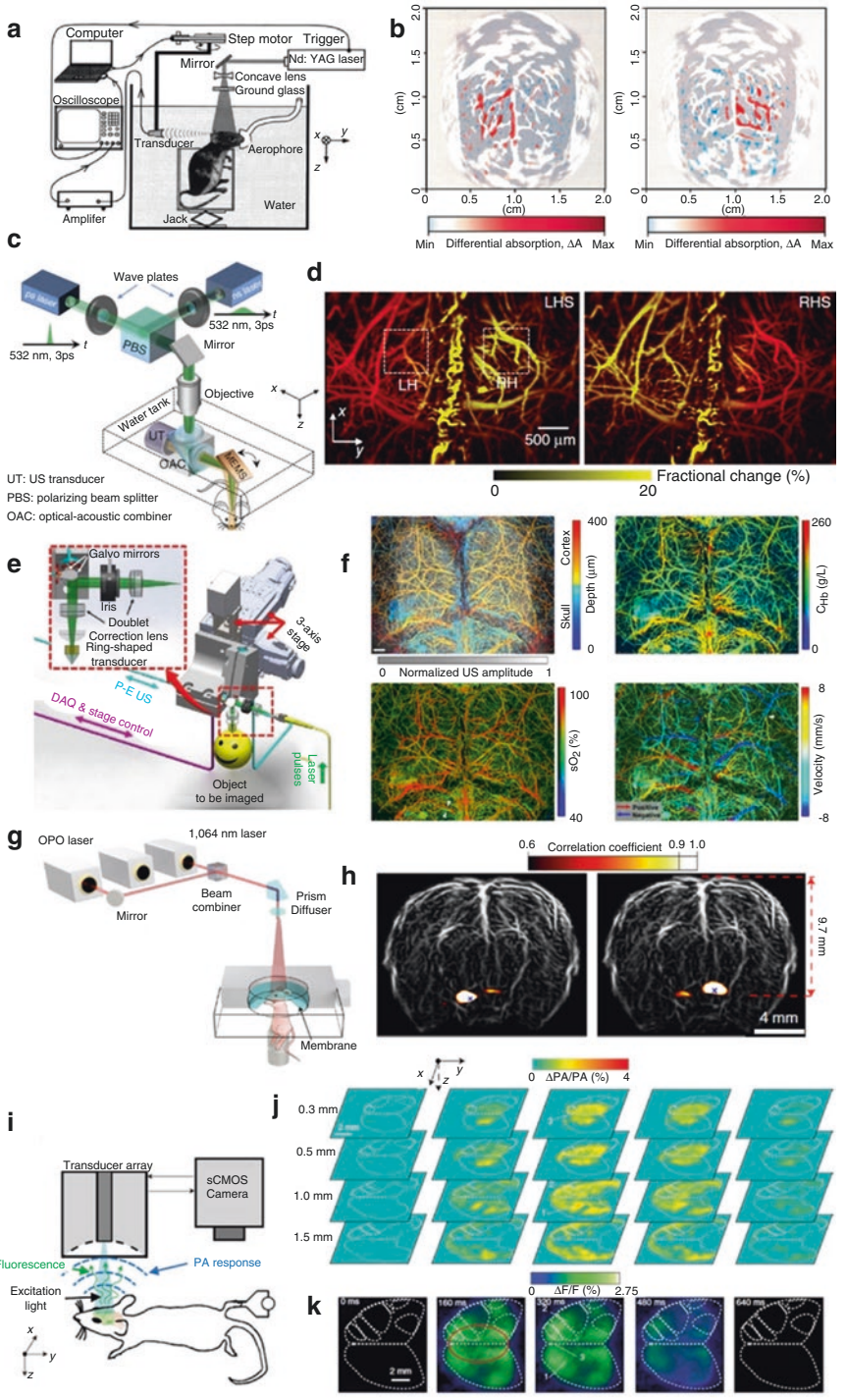
a
Computer
Step motor
Trigger
Nd: YAG laser
Mirror
Concave lens
Ground glass
Oscilloscope
Transducer
Aerophore
Water
Amplifer
Jack
b
(cm)
Min
Differential absorption, ΔA
Max
c
Wave plates
532 nm, 3ps
PBS
Mirror
Objective
Water tank
UT
OAC
UT: US transducer
PBS: polarizing beam splitter
OAC: optical-acoustic combiner
d
LHS
RHS
LH
RH
500 μm
Fractional change (%)
0
20
e
Galvo mirrors
Iris
Doublet
Correction lens
Ring-shaped transducer
3-axis stage
P-E US
DAQ & stage control
Laser pulses
Object to be imaged
f
Cortex
Skull
Depth (μm)
Normalized US amplitude
C_{Hb} (g/L)
sO_2 (%)
Velocity (mm/s)
g
OPO laser
1,064 nm laser
Mirror
Beam combiner
Prism
Diffuser
Membrane
h
Correlation coefficient
4 mm
i
Transducer array
sCMOS Camera
Fluorescence
PA response
Excitation light
j
0.3 mm
0.5 mm
1.0 mm
1.5 mm
ΔPA/PA (%)
k
ΔF/F (%)
2 mm

Fig. 5 PAT small animal brain imaging systems and produced images. (**a**, **b**) A circular-scan PAT system (a) for transdermal and transcranial rat brain imaging and corresponding PACT images (**b**) depicting the cerebral hemodynamic changes in response to left- and right-side whisker stimulation (Wang et al. 2003). (**c**, **d**) MEMS scanner-based fast scan OR-PAM brain imaging system (**c**), and corresponding OR-PAM images (**d**) depicting fractional PA amplitude changes (shown in yellow) in response to left hindlimb stimulation (LHS) and right hindlimb stimulation (RHS), superimposed on the vascular image (shown in red) (Yao et al. 2015b). LH, left hemisphere; RH, right hemisphere. (**e**, **f**) Schematic of a US-aided multi-parametric PAM system (**e**) and corresponding PAM images (**f**) of the mouse brain through the intact skull (Ning et al. 2015). Left top image: Depth-encoded skull vasculature (indicated by a cool color) and cortical vasculature (indicated by a warm color) separated by the ultrasonically determined skull (in gray). Other images (clockwise): Simultaneously acquired high-resolution maps of C_{Hb}, sO_2, and CBF (both speed and direction), respectively. Scale bar: 0.5 mm. (**g**, **h**) Schematics of a SIP-PACT system (**g**), and corresponding PACT image (**h**) depicting a rat whole-brain vasculature in the coronal plane and seed-based functional connectivity analyses of the thalamus region on both sides of the brain (Li et al. 2017). (**i**) Bimodal PA and fluorescence imaging setup for noninvasive imaging of the GcaMP6f brain in vivo *(*Gottschalk et al. 2019*)*. (**j**) Noninvasive imaging of somatosensory-evoked rapid calcium transients in the GcaMP6f brain in vivo. Four-dimensional photoacoustically recorded brain activation maps ($\Delta PA/PA$) in response to the current stimulus at $t = 0$ at the right hind paw. Slices across the entire brain are shown to be located at different depths from the brain surface. Functional regions of the brain are indicated as dashed white lines. (**k**) Temporal sequence of fluorescence recorded brain activation maps ($\Delta F/F$) in response to the stimulus at $t = 0$

poly(ethylene glycol)-coated nanoshells (Wang et al. 2004a), in order to increase the signals from the cortical vasculature. In the next year (2005), Ku et al. reported the first PAT-based tumor imaging result using the rat mammary adenocarcinoma cell line (Br7-C5) and successfully visualized angiogenesis around the tumor tissues developed in a cerebral hemisphere after the inoculation (Ku et al. 2005). Thereafter, in 2006, Wang et al. demonstrated the feasibility of PAT-based sO_2 mapping, which subsequently played a central role in the functional imaging capability of PAT throughout the entire PAT area (Wang et al. 2006). By using 584- and 600-nm wavelengths, they successfully visualized the sO_2 change in the brain cortex according to the artificial modulation of the oxygen level in the inhaled gas (i.e., between hyperoxia and normoxia or hypoxia and normoxia). Further, in 2008, Li et al. demonstrated the first tumor molecular imaging by using an ICG derivative contrast agent, IRDye800-c(KRGDf), which was developed to target integrin $\alpha_v\beta_3$ overexpressed in human U87 glioblastomas in nude mouse brains (Li et al. 2008c).

Meanwhile, in the late 2000s, two new PAT technical platforms—called the AR- and OR-PAM—were presented in the field (Maslov et al. 2005, 2008) and began to be applied to the brain imaging application as well. Since the techniques could provide much finer vasculature images at also an increased imaging speed compared to the conventional PACT, research progress of the brain application could be boosted and also widened in terms of the spectrum. The three reports presented by Stein et al. (Stein et al. 2009a, b) and Li et al. (Li et al. 2009) in 2009 were the first cases that applied the AR-PAM technique to the brain imaging study, in which more detailed views of the vasculature in a brain cortex (Stein et al. 2009a, b) and solid brain tumor (Li et al. 2009) were presented, respectively. In addition, in the same

year, Hu et al. (Hu et al. 2009a) presented the first report that applied the OR-PAM technique for brain imaging. In the paper, they presented a transcranial mouse brain imaging result that achieved a much finer visualization of the vasculature with a spatial resolution of ~5–10 μm, which enabled a capillary-level visualization, and also demonstrated an sO_2 map for the single capillary-level blood vessels distributed in a local brain cortex.

In addition to the two technical platforms, there was another important technical platform presented in 2009, which thereafter has continuously had a great impact on the brain imaging study thus far. It was the 512-element-based full-ring array transducer-based PACT system (Gamelin et al. 2009), constructed by Gamelin et al. of the Zhu group, and was an upgraded version of the previous partial ring system reported in 2008 (Gamelin et al. 2008). Since the array system could capture all the PA waves diverging from a source along the detection plane simultaneously, unlike the previous mechanical scanning PACT system, it enabled cross-sectional images with a frame rate of up to 8 Hz, which was almost 200 times faster than that of the mechanical scanning PACT system (Wang et al. 2003). Due to the emergence of the array technique, most of the later PACT-based brain imaging studies were replaced with it; finally, the array transducer-based PACT, as well as the AR- and OR-PAM, became the three major technical platforms for brain imaging as well as other applications.

Based on the techniques, PAT brain imaging studies began to show a more active progress in the beginning of the 2010s, as the related concepts were popularized among other groups. Although, consequently, related research outcomes were also presented from other groups, most key achievements reported until 2015 appeared to be only from the Wang group. In particular, in the period between 2010 and 2015, the Wang group also presented several notable techniques and methods, such as the flow speed measurement based on the Doppler principle (Yao et al. 2010b), visualization of a single-RBC blood flow based on high-speed OR-PAM (Wang et al. 2013), glucose metabolic imaging of a mouse brain based on 2-NBDG (Yao et al. 2013), and investigation of the functional connectivity of a rat brain based on PACT (Nasiriavanaki et al. 2014). Although some of these techniques were not directly related to the brain imaging application, they made the related research spectrum expand further.

Overall, entering the 2010s, PAT techniques have been steadily improved in terms of the imaging speed, imaging depth, sensitivity, and functional or molecular imaging capability, thereby resulting in various research outcomes. However, among numerous reports, here, we introduce several recent key papers that well represented the imaging capabilities of the state-of-the-art PAT brain imaging systems.

First, in the report presented by Yao et al. of the Wang group in 2015, the authors showcased how fast a brain imaging could be performed using a state-of-the-art OR-PAM system (Yao et al. 2015b). Although the imaging speed of a mechanical scanning OR-PAM is generally lower than that of an array transducer-based PAT system, when they are compared in terms of a volumetric imaging, it can do much better in terms of a B-scan imaging if an adequate scanning mechanism is employed.

As demonstrated in the report, they achieved a B-scan imaging as fast as 400-Hz over a ~ 3 mm scanning range, which was ~200-times faster than that of the second-generation OR-PAM system, by employing a fast-oscillating MEMS mirror scanner that reflected and steered both the excitation laser beam and the detection acoustic axis (Fig. 5c).

Most of all, due to the greatly improved imaging speed, they were able to reproduce the brain hemodynamic response imaging experiment presented in ref. (Wang et al. 2003) at a more detailed (~3 μm spatial resolution) and sensitive level. As depicted in Figure 5d, which are transcranial PA maximum amplitude projection (MAP) images, they successfully recorded the contralateral hemodynamic responses in the somatosensory regions of a mouse brain according to the electrical stimulations alternatingly applied to the left and right hindlimbs in a much faster imaging speed. Moreover, it was also notable that the system's sensitivity was sufficient to capture the increase in blood volume in the ipsilateral somatosensory region, which might be a phenomenon that hemodynamically represented the functional interconnection of blood vessels distributed in the two hemispheres.

In addition to this, for the first time in the paper, they presented a new method that mapped the sO_2 of a mouse brain in action in vivo based on the single-wavelength, pulse-width-based sO_2 measurement. Unlike conventional dual-wavelength-based sO_2 mapping (Zhang et al. 2006a; Hu et al. 2011; Yang et al. 2012a), this new method featured the use of two laser pulses with a different pulse length (nano- and pico-second) but with the same wavelength of 532 nm, thereby capitalizing the different absorption saturation effect of both oxy- and deoxy-hemoglobin at the two pulse lengths. Since the method is not affected by the unknown fluence information typically occurring in the conventional sO_2 measurement method, it also could have an impact on numerous other applications. Overall, the demonstrated high-speed, high-resolution, label-free functional hemodynamic imaging capability suggests that PAT could be a new powerful tool for understanding the neurovascular coupling phenomenon (i.e., hemodynamic response associated with neuronal activity).

The B-scan imaging speed demonstrated in the study could be understood as a kind of speed limit achievable by the MEMS scanner-based scanning mechanism. However, in a report presented by Lan et al. of the Yao group in 2018 (Lan et al. 2018), an even faster brain imaging was demonstrated by adopting a different scanning mechanism that employed a fast rotating hexagonal mirror. In the schematic presented in Figure 5c, the MEMS mirror performed a mechanical scanning based on its mechanical oscillation, in which acceleration and deceleration were involved. However, in the new system (Lan et al. 2018), they steered a coaxially aligned laser beam and acoustic waves by employing a hexagonal mirror that constantly rotated only in one direction with a rather fast rotational speed of 150 Hz. Since the hexagonal mirror was actuated by a DC motor with no directional change, it was possible to achieve a B-scan imaging speed that was ~two times faster than the MEMS scanner-based method (Yao et al. 2015b)—actually, it was an area scanning speed that was ~10 times faster when considering the scanning range augmentation widened up to ~12 mm.

Thus far, we have introduced the two papers that showcased a technical extreme in terms of B-scan imaging speed. As presented, OR-PAM can visualize cortical vasculature based on the endogenous contrast mechanism, because PAT is very sensitive to hemoglobin absorption. Although the presented examples were mostly focused on related image productions, it is also well known in the PAT field that from the acquired vasculature image, one can extract quantitative information on the following five anatomical and physiological parameters—tissue volume, vessel diameter, total hemoglobin concentration (C_{Hb}), sO_2, and cerebral blood flow (CBF) of a blood vessel distributed in a mouse brain cortex (Wang 2008; Hu and Wang 2010). Since ~2008, the Wang group has been solidifying the related technique formalisms to establish a method to quantitatively measure how much oxygen is consumed in a specific or entire area of a brain cortex—that is, the cerebral metabolic rate of oxygen ($CMRO_2$) (Wang 2008; Hu and Wang 2010). Although the group presented multiple reports related to the issue, here, we introduce one of the recent reports presented by Ning et al. of the Hu group in 2015, as it discussed a more accurate measurement method for the mentioned parameters (Ning et al. 2015).

Unlike previous reports (Hu et al. 2011; Yao et al. 2015b), in the study, they paid attention to the optical and acoustic wave distortion effect caused by the skull, which eventually hindered the accurate mapping of the aforementioned physiological data set. Thus, in order to address the issue, they constructed a new version of the OR-PAM system that was combined with the conventional US imaging function (Fig. 5e) and performed an OR-PAM imaging by applying a dynamic optical focusing to a target tissue during its scanning based on the skull contour information provided by the US imaging. Consequently, based on the method, they could acquire much clearer and more precise data on C_{Hb}, sO_2, and CBF simultaneously and also at the same spatial scale of 10 μm, as illustrated in Figure 5f. Although the imaging speed had to be lowered due to the intervening of the dynamic focusing process and actual estimation of $CMRO_2$ in a brain cortex was not exemplified, the achievement was considered important progress in the practical implementation of the related goal.

Apart from the presented cortical imaging, PAT also can be utilized for small animal whole-brain imaging. In the paper by Li et al. of the Wang group in 2017, they demonstrated an ~11 mm image penetration, which can potentially cover the entire volume of an adult rat brain (Li et al. 2017). Based on their advanced PACT theory and technology termed "single-impulse panoramic PACT" (SIP-PACT), they demonstrated the small animal whole-brain imaging capability of PAT by using the 512-element full-ring array system (5 MHz) (Fig. 5g), which was upgraded from its earlier version (Gamelin et al. 2009). As previously mentioned, the prototype of the 512-element full-ring array transducer-based PACT technology was originally presented by the Zhu group (Gamelin et al. 2009). However, the Wang group continuously improved the technology in terms of the illumination optics, DAQ hardware, and image reconstruction algorithm. In particular, by developing a simultaneous one-to-one mapped DAQ system engaged with the array transducer and a half-time dual-speed-of-sound universal back-projection algorithm, they achieved a 2D panoramic acoustic detection completable within 50 μs and 125 μm isotropic in-plane resolution within a field of view (FOV) of ~16 mm in diameter for a single laser pulse.

The performance of the system was surprising. As illustrated in Figure 5h, they could acquire detailed vasculature images of a whole rat brain with a penetration extended up to 11 mm. Moreover, by analyzing the spontaneous hemodynamic responses between 16 contralateral regions distributed in the coronal plane (~bregma −2.16 mm) of the rat brain, they found a clear correlation (i.e., functional connectivity) between the corresponding regions across the left and right hemispheres, which was consistent with previous research on both fMRI and power Doppler US. Notably, they were able to observe a left–right correlation even at the thalamus regions located at 9.7 mm depth from the surface. Previously, a report presented by Nasiriavanaki et al. of the same group provided a similar PACT-based functional connectivity analysis study for the first time (Nasiriavanaki et al. 2014). However, this new study performed related analysis over a more global brain area and also with a much improved spatial resolution.

Indeed, the demonstrated in vivo high-resolution deep brain imaging was a great achievement that far exceeded the capabilities of previous PAT studies, which were mostly limited to visualizing only cortical vasculatures (Hu et al. 2009a, 2011; Wang et al. 2003, 2013; Gamelin et al. 2009; Gamelin et al. 2008; Yao et al. 2013; Nasiriavanaki et al. 2014; Yao et al. 2015b; Hu and Wang 2010; Ning et al. 2015). Since the deep brain area is recently recognized as being important in relation to understanding the origin of memory and numerous neurological diseases, such as Alzheimer's and Parkinson's, while functional MRI (fMRI) and power Doppler US are only currently available tools for such deep brain functional studies, the presented demonstration is a good example showcasing the importance of PAT for such an application.

Although the presented real-time and label-free brain vasculature and hemodynamics imaging capability of PAT is the core technical contribution to neuroscience, it has also been a long-standing question whether PAT has the ability to directly map a neuronal activity because it is undeniably the major function of the brain. In the paper by Gottschalk et al. of the Razansky group in 2019, a result that answered this question was presented (Gottschalk et al. 2019).

By using a mouse model that expressed a genetically encoded calcium indicator GCaMP6f, the group demonstrated the real-time and brain-wide mapping capability of PAT for the calcium dynamics in vivo for the first time. Figure 5i illustrates the imaging system that they developed and customized to perform the study. First, the system featured the dual-mode imaging capability, presenting conventional planar fluorescence and three-dimensional (3D) PA images simultaneously or sequentially. In addition, it performed a rather fast volumetric PA imaging, as high as 100 Hz, over the entire imaging volume (~2 cm^3) based on the 512-element spherical matrix transducer array with a 5-MHz central frequency and produced a PA image with an almost isotropic 3D spatial resolution of ~150 μm.

Surprisingly, with the system, they were able to successfully acquire the first snapshots of the spatiotemporal propagation profiles of the calcium transient waves based on the PA imaging function, as illustrated in Figure 5j. Notably, the calcium signals could be photoacoustically differentiated even in the presence of strong hemoglobin background absorption, and the GCaMP6f's responses were evoked by

the electric stimulations applied to the right hind paw (one pulse with a 50-ms duration at every 20 s). A set of sequentially acquired planar fluorescence images also visualized the wave propagation (Fig. 5k). However, it was less clear compared to the PA imaging in terms of the initial cortical localization and depth-wise entanglements of the waves around the corresponding somatosensory region and thereafter propagation. Moreover, in the PA imaging mode, it was observed that the peak response appeared after a delay of ~360 ms from the stimulation, which is in accordance with known knowledge; clear bilateral activations were detectable at a depth of approximately 1 mm.

In the presented PA images (Fig. 5j), in order to effectively differentiate the calcium waves, they presented the results in a differential mode normalized by a reference image (i.e., ΔPA/PA); this is because when the peak excitation wavelength of GCaMP6f (488 nm) was applied to the GCaMP6f-expressing mouse for a PA excitation, the acquired PA images mostly exhibited vascular contrasts rather than GCaMP6f's contrasts (note that hemoglobin was still the dominant absorber at the wavelength). In addition, the PA imaging experiment was performed at a relatively lowered frame rate of 25 Hz, which, however, was still sufficient for capturing the calcium spikes that typically disappeared after ~0.8 s; moreover, the pulse duration of the electric stimulation was set at as short as 50 ms to minimize background hemodynamic responses.

Indeed, the reported results are great achievements that evidence that PAT is capable of providing 3D neuronal activity with unparalleled spatiotemporal resolution and sensitivity over conventional planar fluorescence imaging and also that no other currently available imaging modality can replace the ability of PAT in terms of the versatile contrast, speed, resolution, and FOV, all of which are critical for studying neurodynamics.

Thus far, we have introduced several representative examples showcasing the current forefronts of the PAT brain imaging study. Although it is true that these are currently the dominant research directions highlighting the core advantages of PAT in neuroscience, a couple of notable papers presenting a new approach have been reported in recent years (Tang et al. 2015b, 2016; Cao et al. 2017). Unlike the presented conventional brain imaging studies (Xu and Wang 2006b; Wang et al. 2004a, b; Ku et al. 2005; Wang et al. 2006, 2013; Li et al. 2008c, 2009; Stein et al. 2009a, b; Hu et al. 2009a; Gamelin et al. 2009; Gamelin et al. 2008; Yao et al. 2013, 2015b; Nasiriavanaki et al. 2014; Hu and Wang 2010; Ning et al. 2015; Gottschalk et al. 2019), in which an animal was imaged in a resting and restrained state, the new approach is related to imaging an awake (Cao et al. 2017) or moving animal (Tang et al. 2015b, 2016). Figure 6 depicts the related examples that imaged a freely behaving mouse brain based on a wearable device (Fig. 6a) and a head-restrained OR-PAM system (Fig. 6c), which provided a lower degree of freedom compared to the first.

Actually, such an imaging approach was first proposed by researchers in the CFM and TPM field to understand how neural circuits produce animal behavior by directly monitoring related cellular events that occur in small animal brain in situ and real time (Wilt et al. 2009). Currently, in the reported PA images (Fig. 6b and d), meaningful signals directly reflecting the animal's behavior were hardly captured

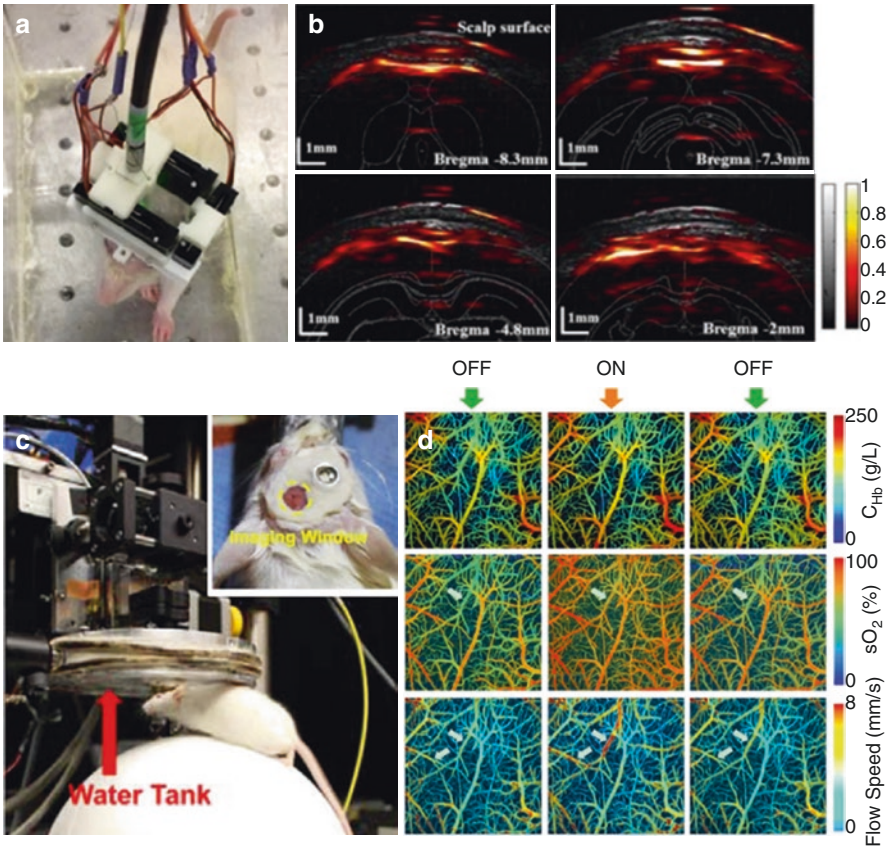

Fig. 6 Wearable and head-mounted PAT systems and produced images. (**a**, **b**) A wearable PA imaging device (**a**) for imaging the brain of a freely behaving mouse and acquired B-scan image (**b**) (Tang et al. 2016). (**c**) Photo of a head-restrained PAM system (Cao et al. 2017). The inset shows the photo of a mouse brain with a thinned skull window and a nut attached using dental cement. (**d**) Head-restrained PAM of cerebral C_{Hb}, sO_2, and blood flow speed in the absence (OFF) and presence (ON) of isoflurane. The white arrows in the second and third rows highlight the isoflurane-induced changes in the average sO_2 values of the draining veins and blood flow speed

because there was a tricky technical issue related to stable light delivery and US detection that must be overcome. The first paper only presented a 2D cross-sectional image of blood vessels, and the second study was also limited to several hemodynamic parameter changes according to the variation of inhaled anesthesia gas (isoflurane). Nevertheless, it is an undeniably important research direction to ultimately answer the mentioned question; in this regard, it is expected that PAT could make a valuable contribution to the study because PAT can provide real-time image information on the hemo- and neurodynamics of a brain in action at unprecedented imaging depth compared to other optical neuroimaging modalities.

In this section, we reviewed several notable research outcomes reported in the PAT brain imaging application. As presented, PAT has a unique advantage for the

brain imaging application in terms of the label-free visualization of vasculature and real-time hemodynamic imaging. Again, it is the only method that can provide five anatomic and physiological parameters—that is, the tissue volume, vessel diameter, concentration of hemoglobin, sO_2, and blood flow—quantitatively based on a single imaging system (Wang 2008; Hu and Wang 2010; Yao and Wang 2014b). In addition, by optimizing necessary optical illumination and acoustic detection parameters, it is also possible to image the deep brain area of a small animal (Li et al. 2017). Further, global neuronal dynamics also can be imaged in real time with the aid of existing calcium indicators (Gottschalk et al. 2019). Based on the listed strengths, it is highly expected that PAT could make a crucial contribution to understanding the complex mechanism of a whole brain's in vivo dynamics as well as its neurovascular coupling, thereby complementing conventional neuroimaging modalities.

Small Animal Whole-Body Imaging

The feasibility of PAT-based small animal whole-body imaging and molecular imaging was first demonstrated in the two papers reported by Kruger et al. in 2003, in which several TAT image slices of a mouse's head and body trunk were well presented (Kruger et al. 2003a; b). However, earnest research interest appeared after Brecht et al. of the Oraevsky group reported the first 3D whole-body image of a mouse in vivo in 2009 (Brecht et al. 2009). As the paper presented a detailed 3D image of internal organs visualized noninvasively, the related application became one of the major areas of PAT and also became associated with numerous biological or preclinical studies in conjunction with various disease models like cancer and models like gene expression.

Needless to say, such a small animal-based whole-body imaging approach is a valuable methodology for both preclinical and fundamental biological studies, as it may provide us with a better understanding or new findings on numerous important biological processes and deeper insights on disease development mechanisms on a whole-body scale. In addition, it could enable the testing of a custom-designed disease model or a treatment effect of a new drug or therapeutic method. Although MRI, X-ray, and US imaging are the major imaging tools presented in related studies, there are numerous unique benefits of PAT. Thus, in this section, we introduce several notable achievements that showcase the current capabilities of PAT for small animal whole-body imaging, focusing on the papers reported from 2009 onward.

Figure 7a depicts a photo of the system, with which the Oraevsky group acquired the first small animal whole-body image in vivo (Brecht et al. 2009) and that was embodied in the form of an array transducer-based PACT. In particular, the system features the use of a concave arc-shaped array transducer comprising 64 piezo-elements with a center frequency of 3.1 MHz (−6 dB bandwidth: >80%). However, by adding additional rotational scanning with 150 steps to the animal along its mounting axis, it was possible to create a virtual spherical array with 9600 detection positions, thereby achieving a spatial resolution of ~0.5 mm. In the reported imaging demonstration, although the PRR of their laser system was 10 Hz, a complete

scanning time for producing a whole-body 3D imaged required ~8 min due to the signal averaging over 32 laser pulses.

Figure 7b depicts the exquisite performance of the system, revealed through the 3D whole-body imaging of two mice. Both images were acquired using a 755-nm excitation, but each was from a female (left) and male (right) mouse, respectively. In the left image, both kidneys, as well as the spleen and a partial lobe of the liver, were clearly imaged. In addition, the ovarian vessels, as well as the inferior vena cava and its bifurcation into the femoral veins, were visible. Similar structures were also imaged in the right image. However, the kidneys appeared obscured, whereas the spine—in which numerous small vessels are distributed—was visualized more clearly than in the left image.

In 2011, Razansky and Ntziachristos et al. reported another type of whole-body imaging system that employed a similar arc-shaped 1D curved array transducer with 64 elements (5 MHz center frequency) (Fig. 7c) (Razansky et al. 2011). However, their transducer was different from that of the Oraevsky group in that it had an additional focusing capability along the longitudinal direction (i.e., *z*-direction) owing to its spherically concaved surface along the mentioned direction, which resulted in a geometrical focal length of 4 cm. In addition, they utilized a different animal positioning strategy that placed an animal inside a horizontally arranged holder to avoid direct contact of the animal with the surrounding matching medium, and illuminated the animal at 10 different positions to more uniformly excite the trunk during PA imaging, which eventually enabled a simultaneous DAQ. Notably, although the geometrical spanning of the array transducer only covered the animal by 172°, no rotational scanning of the transducer around the animal's trunk nor the rotation of the animal itself was added. Only the animal was translated along the *z*-axis to image different body sites. Nevertheless, an in-plane resolution of 150 μm was guaranteed, while the elevation resolution—whose value was determined by the aforementioned geometric focusing—was ~800 μm.

Such horizontal placement provided for a more comfortable imaging condition for the animal, and the DAQ system that they constructed enabled a cross-section imaging speed as fast as <1 ms/frame, although the actual imaging speed demonstration was imposed by the PRR of the employed laser system to ~10 Hz. Unlike the system of the Oraevsky group, whose imaging was mostly limited to the trunk, this system was capable of imaging even the thoracic and head regions in a 2D fashion (Fig. 7d) by simply positioning the area of interest along the horizontal direction (i.e., *z*-axis); moreover, it also featured a real-time imaging capability by aligning the imaging plane of the arc-shaped transducer across the body trunk (Fig. 7c). Further, in order to demonstrate the system's fast B-scan imaging capability, they imaged the perfusion of ICG in vivo after its injection into a mouse kidney (Fig. 7e) and also indicated the dynamic imaging of the respiratory motion at a frame rate of 10 Hz. In addition to this paper, there also were two notable preceding reports that showcased the system's more detailed imaging capability for renal and cardiovascular systems (Buehler et al. 2010; Taruttis et al. 2010). Moreover, in 2012, Taruttis et al. of the group also demonstrated its more comprehensive imaging capability for the pharmacokinetics of an injected drug (Taruttis et al. 2012).

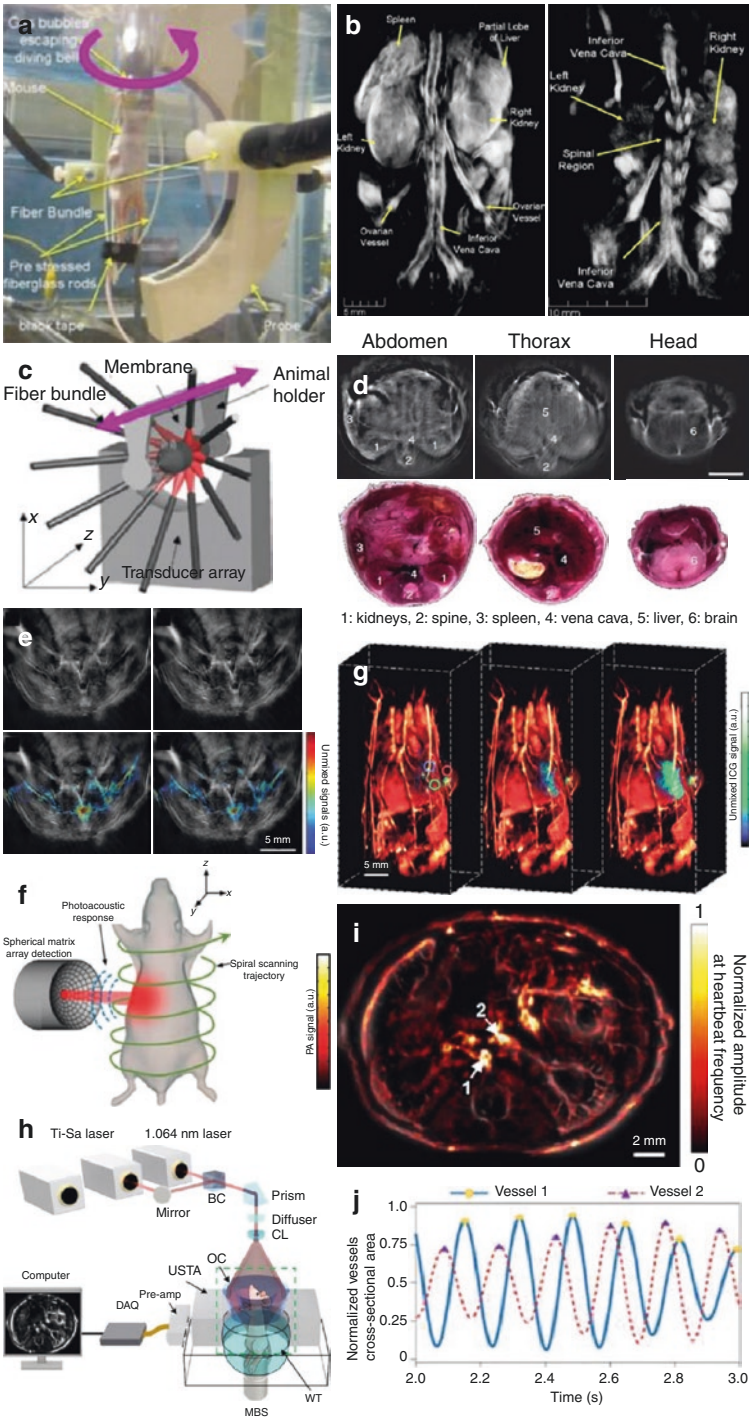
a
Fiber Bundle
Pre stressed fiberglass rods
black tape
Probe
b
Spleen
Partial Lobe of Liver
Right Kidney
Left Kidney
Ovarian Vessel
Inferior Vena Cava
Inferior Vena Cava
Left Kidney
Right Kidney
Spinal Region
Inferior Vena Cava
c
Membrane
Fiber bundle
Animal holder
x
z
y
Transducer array
Abdomen
Thorax
Head
d
1: kidneys, 2: spine, 3: spleen, 4: vena cava, 5: liver, 6: brain
e
5 mm
Unmixed signals (a.u.)
f
Photoacoustic response
Spherical matrix array detection
Spiral scanning trajectory
PA signal (a.u.)
g
5 mm
Unmixed OCI signal (a.u.)
h
Ti-Sa laser
1.064 nm laser
Mirror
BC
Prism
Diffuser
CL
OC
USTA
Computer
Pre-amp
DAQ
WT
MBS
i
2 mm
1
0
Normalized amplitude at heartbeat frequency
j
Vessel 1
Vessel 2
Normalized vessels cross-sectional area
1.0
0.75
0.5
0.25
0
2.0
2.2
2.4
2.6
2.8
3.0
Time (s)

Fig. 7 PAT small animal whole-body imaging systems and produced images. (a, b) An arc-array transducer-based PACT system (**a**), and corresponding 3D PA images (**b**) acquired from nude mice using a 755-nm laser excitation (Brecht et al. 2009). (**c**, **d**) A 64-element (5 MHz) curved array transducer-based PACT system (**c**) in which an animal could be translated horizontally over a 15-cm range to acquire a 3D image and corresponding PA images (**d**) showing the cross-sections (upper row) acquired at the abdominal, thoracic, and head levels using a 750-nm laser excitation (Razansky et al. 2011). Below photos are corresponding ex vivo cryoslices images. (**e**) In vivo tracking of systemic ICG injection into a mouse. The upper left image depicts a single-wavelength (810 nm) PA image of the lower abdomen before intravenous injection of 40 nmol of ICG, and the upper right image depicts the same region 2 min after administering the injection. The lower two images depict spectrally unmixed ICG signals (in color), superimposed onto a single-wavelength image, captured at 2 min (left) and 4 min (right) after the injection. (**f**) Schematic of the SVOT system (Deán-Ben et al. 2017c). (**g**) Spectrally unmixed images (green) for three representative instants following tail vein injection of 100 nmol of ICG at 0 s. The kinetic images were superimposed onto the whole-body PA anatomical reference (red) acquired at 800 nm wavelength. (**h**) Schematics of the SIP-PACT system for trunk imaging (Li et al. 2017). BC, beam combiner; CL, conical lens; MBS, magnetic base scanner; OC, optical condenser; USTA, (full-ring) US transducer array; and WT, water tank. (**i**) Heartbeat encoded arterial network mapping overlaid on the anatomical image. (**j**) A graph showing the relative phase delay between the temporal variations of the cross-sectional areas of the two blood vessels 1 and 2 marked in (**i**)

The presented imaging demonstrations (Figs. 7d and e) were all limited to a 2D recording of the dynamics. However, in 2017, Deán-Ben et al. of the Razansky group reported a new type of small animal whole-body imaging system that enabled a much clearer 3D visualization of the organs and vasculature inside a body trunk (Fig. 7f). As included in the technical term "spiral volumetric optoacoustic tomography (SVOT)" used in the paper (Deán-Ben et al. 2017c), the system also added a mechanical scanning motion with a helical trajectory to an array transducer (4 MHz, 256-elements) that itself was capable of yielding an isotropic spatial resolution of ~200 μm over an ~1 cm^3 imaging volume—that is, FOV (note that this spherical array transducer is a similar one to that employed in Figure 5i, although this paper was reported earlier). Since the laser system employed in the study enabled a PRR of 100 Hz, the imaging system was eventually able to cover a ~ 100 cm^3 imaging volume in merely one second by including additional mechanical scanning; moreover, the system could also perform a dynamic imaging of an organ with a temporal resolution of 10 ms (~50 ms for multispectral imaging) if it was set to continuously record image data in a stationary position.

This system led to a very striking result that has not ever been reported thus far. As illustrated in Fig. 7g, a real-time tumor perfusion of the ICG solution (i.e., a contrast agent) injected via the tail vein of a tumor-bearing mouse was clearly visualized with a frame rate of 20 Hz. Furthermore, an interesting phenomenon of a long delay of ~1.26 s between the appearance of the contrast agent in a major lateral vein versus the tumor area was also observed. The researchers ascribed the extended time delay to the obstruction caused by the tumor growth. Then, the perfused drug flowed into the liver of the animal and was finally revealed as a PA signal decay due to its clearance.

In the paper (Deán-Ben et al. 2017c), their demonstrations were not limited to the experiment. By imaging the flow dynamics of an ICG bolus injected in a similar manner, the real-time motions of a cardiac system and the bolus' appearance in each

ventricle could also be successfully observed (using an independent animal). Further, the renal artery infiltration of Alexa Fluor 750 (AF750) after five-minute post-injection and its filtration in the kidney cortex and subsequent excretion were successfully visualized. In the demonstrations, the lowered frame rate was because of the multi-wavelength imaging requirement for a spectral unmixing, in which five different laser wavelengths were used. Nevertheless, the imaging speed was sufficient for visualizing the contrast agent's kinetics in a living biological system. Undoubtedly, the showcased model was the best imaging performance ever achieved in biomedical PAT, in terms of the effective combination of the imaging speed, image quality, and spectral unmixing capability, and was an invaluable achievement that indicated a new paradigm change in small animal whole-body imaging.

Although their sizes are much smaller, zebrafish and *Drosophila* are also regarded as important models for such body-wide imaging research, and the Ntziachristos and the Razansky groups also reported numerous interesting results based on the two models (Razansky et al. 2009; Ma et al. 2009, 2012; Omar et al. 2017). However, we have not introduced these applications in this chapter because the body dimensions of zebrafish and *Drosophila* are much smaller than those of rodents and, thus, can be imaged by using other optical imaging techniques as well. In addition, we mostly focused on array transducer-based imaging systems to highlight PAT's real-time imaging capability for whole-body imaging.

Meanwhile, by employing the same US detection system utilized for the SIP-PACT-based brain imaging presented in Figure 5g in the previous section, Li et al. of the Wang group in 2017 also demonstrated its applicability to small animal whole-body imaging in the same paper (Li et al. 2017). However, for the experiment, they modified the related illumination optics, as illustrated in Fig. 7h to more efficiently irradiate the trunk zone of a small animal.

First, as with the case of the SVOT system presented in Fig. 7f, this system also could image the entire cross-section of a small-animal body and, thus, visualize the major organs in the thoracic (heart and lung) and abdominal cavities (liver, spleen, kidney, caecum, and intestine). However, the authors of the SIP-PACT system presented an interesting result that highlighted the high-speed and high-resolution imaging capability of the system, which was sufficiently advanced to image a body trunk with an isotropic in-plane resolution of 125 μm at a 50-Hz frame rate.

As depicted in Fig. 7i, they were able to selectively map the artery network in a whole-body cross-sectional image by analyzing the temporal correlation of the vessel diameter changes for all the imaged blood vessels according to the heartbeat frequency. The change in vessel diameter in the arterial network is a natural phenomenon caused by instant blood ejection from the heart; the pressure waves then propagate along the arterial tree, dilating the aortic wall of the arterial tree, as it is directly connected to the heart. Figure 7j depicts the changes in vessel area according to time for the two blood vessels highlighted by arrows 1 and 2 in Fig. 7i and in which a steady phase delay was clearly revealed. Indeed, this was a great achievement that photoacoustically captured the pulse wave propagating through the arterial network for the first time. Based on the result, they suggested that such a capability could provide a noninvasive and direct diagnostic information for chronic coronary artery disease and chronic renal disease.

Here, it must be noted that the 50-Hz imaging speed of the system, which was also subjected to the PRR of the employed laser, was relatively slower than that of the SVOT system and the speed benefit was only available in the 2D imaging mode. Nevertheless, vessel diameters could be better resolved in a cross-sectional image (Fig. 7i) because the in-plane spatial resolution (125 μm) was better than that of the SVOT system due to the use of 512-transducer elements with the 5-MHz center frequency.

In addition to the imaging demonstration, in the paper, they also presented another interesting result that observed different sO_2 response characteristics of individual organs according to the artificially manipulated oxygen challenge (i.e., hypoxia) via inhaled gas. Although related data are not presented here, they observed a relative sO_2 decrease in most organs—such as the brain, liver, and kidney—and a sO_2 increase in a few organs, like the cecum. Based on the observed results, they presented a plausible interpretation that there may exist an adjustment mechanism for the animal's whole-body metabolic activity to survive during hypoxia.

As is evident, the presented research examples showcase that PAT can offer numerous unique opportunities in small animal-based future biological and clinical studies. Among a large number of outstanding technical aspects, this is attributed to the nonionizing radiation-based, high-resolution, real-time, and safe longitudinal imaging capability of PAT. Indeed, this could provide researchers great benefits in terms of versatility and research freedom when designing a relevant experimental model and conducting studies. Although X-ray CT and MRI also have been utilized for such research, X-ray CT requires the use of contrast agents and is always accompanied by numerous concerns caused by its ionizing radiation. Further, MRI suffers from motion artifacts, as a much longer scanning time is necessary to achieve a similar level of spatial resolution for vasculature as that with PAT.

All the presented systems (Fig. 7) had to be accompanied by an additional mechanical scanning mechanism due to the limited number of detection channels in an employed array transducer. However, in the near future, it will be eventually possible to image faster biological processes over the whole-body region without the effect of motion artifacts. Then, more delicate experiments associated with disease models and pharmacodynamics studies can be performed. In this section, the presented examples were mostly focused on the whole-body and label-free imaging capability of PAT; thus, no disease model was involved. However, examples presented in the next section reveal what additional research scenarios can be provided by PAT.

Cancer Research

When an imaging technique is utilized for cancer imaging, there are two important needs. From the perspective of biology, it can promote understanding of underlying mechanisms related to tumor genesis, development, metastasis, and associated microenvironments (Weissleder and Pittet 2008; Fukumura et al. 2010; Amornphimoltham et al. 2011; Brown et al. 2019). On the other hand, if the technique is also applicable clinically—that is, to humans—it is of particular importance in identifying the tumor location (i.e., visualization) in relation to cancer

screening and staging and also to use the technique for guiding other diagnostic or therapeutic procedures (Weissleder et al. 2016; Yun and Kwok 2017). Thus, irrespective of whichever application is eventually considered, it is evident that, among the performance factors listed in "Principles" section, contrast is the most important element to effectively visualize cancerous tissues as well as the spatial distribution of the contrast agent administrated to visualize them.

In terms of this aspect, PAT has immense potential as it can create a variety of different image contrasts based on excellent spectroscopic imaging ability. As already mentioned in "Principles" section, thus far, numerous studies have demonstrated that, compared to conventional US imaging, PAT can provide much clearer image contrasts for cancerous tissues even using the endogenous contrast mechanism. In addition, in order to create additional exogenous image contrasts for tumor, a variety of dedicated contrast agents for PAT have been suggested, along with successful demonstrations of their biocompatibility and functionalities, such as targeting and therapeutic functions (Mehrmohammadi et al. 2013; Nie and Chen 2014; Weber et al. 2016; Gujrati et al. 2017).

Since 2005, in which the first PAT-based in vivo tumor imaging experiment was presented (Ku et al. 2005), the largest number of papers have been reported in relation to cancer application (for example, among all the papers published in 2019, over 50% expressed their relationship to this application). In particular, it is evident that related publications showed a sharper increase around 2014, probably due to the global spread of the PAT technique along with the inflow of more researchers and that they presented various approaches and goals, such as the ones based on various kinds of tumor models (xenograph, orthotopic, etc.), and also the ones that aimed at a drug test or the validation of a developed contrast agent to target specific biomarkers (Mehrmohammadi et al. 2013; Taruttis et al. 2015). Among many, particularly the studies associated with contrast agent development for actual clinical use accounted for a considerable portion of the reports (Mehrmohammadi et al. 2013; Nie and Chen 2014; Weber et al. 2016; Gujrati et al. 2017). Of course, although many of them successfully demonstrated their feasibility for actual clinical use, it is currently true that, as a completely new type of chemical developed for PAT, they require more rigorous and systematic studies because the toxicity and accompanying clearance issues of an injected contrast agent must be completely resolved before the translation. Thus, in this section, we present several possible research scenarios of PAT in relation to biological or preclinical cancer research, mostly focusing on those papers that well represented the distinctive imaging features of PAT over existing imaging modalities for the purpose.

First, PAT can provide quantitative information on numerous functional and physiological parameters associated with tumor development in an animal model based on an employed single PAT imaging system only. As already mentioned in "Brain Imaging" section, PAT is a unique imaging modality that can simultaneously image anatomical and physiological parameters such as the tissue volume, vessel cross-section (diameter), concentration of hemoglobin, sO_2, and blood flow. Thus, the first statement represents that related parameters also can be utilized for understanding the tumor microenvironment. In 2011, Yao et al. of the Wang group

presented a report that actually demonstrated such a capability of PAT and also showcased the importance of the other parameter termed the metabolic rate of oxygen (MRO_2) (Yao et al. 2011), which can be calculated based on the measurements of the aforementioned parameters and is also typically regarded as a more useful index compared to other oxygenation indexes of tissue—such as sO_2 and partial oxygen pressure (pO_2)—because it directly reflects the rate of oxygen consumption instead of the static oxygen concentration (Buxton and Frank 1997).

In the study, in order to observe a significant change in the aforementioned parameters, they designed a series of experiments that imaged nude mouse ears representing four different physiological and pathological conditions—that is, hyperthermia, cryotherapy, melanoma, and glioblastoma—by employing the first OR-PAM system reported in 2008 (Fig. 8a)(Maslov et al. 2008). As mentioned earlier, the system featured the greatly improved spatial resolution (5 μm for transverse and 15 μm for axial) compared to any other PAT system that was available at that time. They chose the mouse ear model because it can be treated as a well-defined biological system for the in vivo validation of such a quantitative imaging approach and its thickness can be covered by the penetration depth (~700 μm) of the OR-PAM system.

Among the results acquired from the aforementioned four conditions, Figure 8b–d illustrates the cases of a control (upper row: before inoculating the tumor) and U87 human glioblastoma (GT)-bearing mouse ear (lower row: day 7 after the xenotransplantation of the tumor), respectively, and Figure 8e represents the calculated physiological parameters for the two cases. After 7 days of tumor inoculation, it was evident that numerous new blood vessels appeared in the intratumoral region due to angiogenesis (see the lower image of Fig. 8c). Moreover, there was a significant increase in the volumetric flow rate, while the oxygen extraction fraction (OEF) decreased (see Fig. 8e); here, the OEF is defined as $(sO_{2in} - sO_{2out})/sO_{2in}$ and represents the proportion of O_2 molecules that cross the capillary wall (the subscripts *in* and *out* denote feeding and draining vessels, respectively).

However, there was a more notable finding that—rather counterintuitively—the early-stage glioblastoma expressed a hyperoxic state instead of a hypoxic state, although there was a significant increase in MRO_2 (i.e., hypermetabolism) compared to the control data (see Fig. 8e). Here, the hyperoxic state of the tumor region could be conjectured indirectly by the analyzed sO_2 value of the draining vein, but also could be determined by directly analyzing the sO_2 value of intratumoral vasculature in the lower image of Figure 8c; Figure 8f represents the result acquired from the direct analysis. It must be noted that a similar tendency was also observed in the result of the melanoma tumor imaging experiment performed in the study (but not presented here). Based on this result, the researchers suggested that the MRO_2 parameter could be a more reliable measure for early cancer detection if related imaging techniques are applied to clinics.

Currently, the presented imaging experiments are only limited to tumors that are developed in a shallow tissue—that is, mouse ear—where OR-PAM (that is, the ballistic imaging version of PAT) can be applied and where the region of interest is

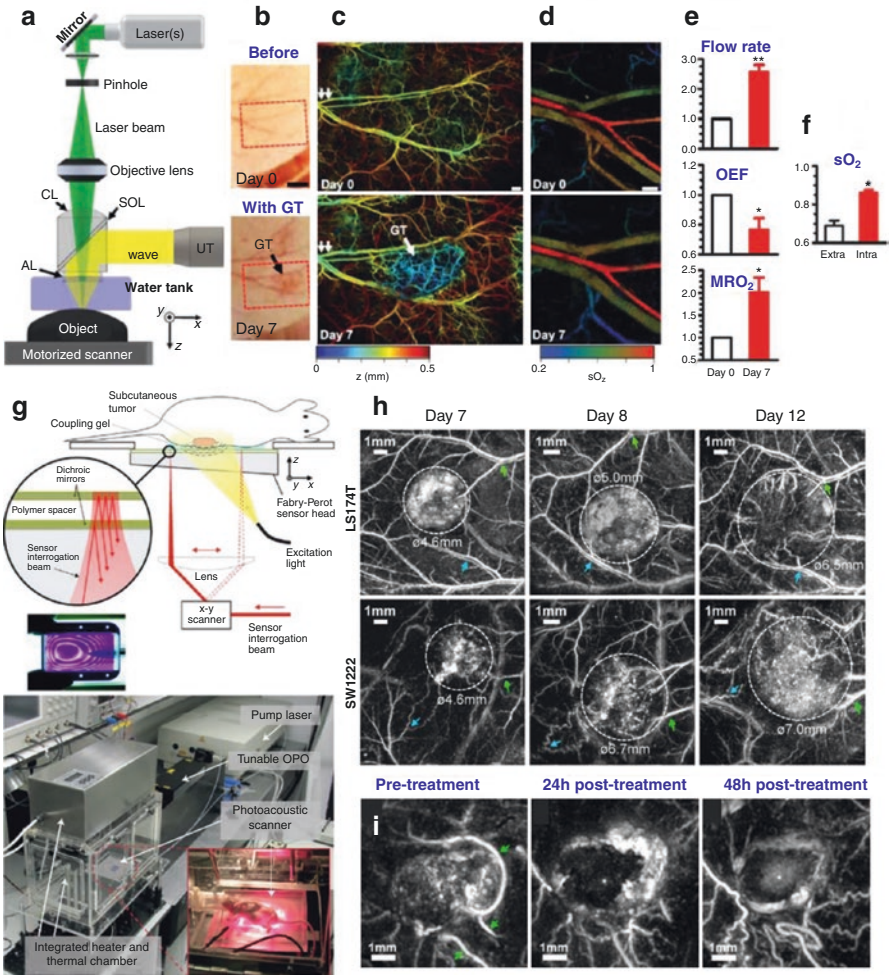

Fig. 8 Examples of PAT cancer imaging applications. (**a**) Schematic of an OR-PAM system (Yao et al. 2011). CL: correction lens; AL: acoustic lens; SQL: silicone oil layer; UT: US transducer. (**b**) Photos of a representative mouse ear before (day 0) and 7 days after the xenotransplantation of U87 glioblastoma tumor cells. Scale bar: 2 mm. (**c**) OR-PAM images (584 nm) of microvasculature in the tumor region, which correspond to the dashed boxes in (**b**) and z is coded by colors. Scale bar: 250 μm. GT: glioblastoma tumor. (**d**) Metabolic PAM images of sO_2 in the artery–vein pair (i.e., double arrows in (**c**)) that supports the tumor region. The two images were acquired at days 0 and 7, respectively. Scale bar: 100 μm. (**e**) OR-PAM quantification of volumetric blood flow rate, OEF and MRO_2 7 days after the tumor xenotransplantation, normalized by the values of day 0. (**f**) Comparison of the averaged sO_2 values in the intra- and extra-tumoral vasculatures. (**g**) Schematic and photo of the Fabry-Pérot polymer film US sensor-based PAT system (Laufer et al. 2012a). The thickness of the polymer spacer in a natural state is 40 μm. (**h**) PA x–y MAP images showing the development of two types of human colorectal tumor (LS174T, SW1222) and the surrounding vasculature between day 7 and day 12 post-inoculation. The dashed lines indicate the tumor margins. (**i**) PA images (640 nm) showing the effect of a vascular disrupting agent (OXi4503) on the blood vessel network of a tumor (LS174T). These are x–y MAP images through the center of the tumor before treatment, 24 h after treatment, and 48 h after treatment

well-defined because the quantitative measurement of sO_2 and flow speed is currently challenging with the optical diffusion regime. Nevertheless, there is sufficient possibility for the related imaging approach to be further extended to deeper tissue regions, as multiple studies have presented several feasible methods for solving such issues (Cox et al. 2012; Deán-Ben et al. 2015; Perekatova et al. 2016; Tzoumas et al. 2016; Hochuli et al. 2019; van den Berg et al. 2015, 2016; Brunker and Beard 2016; Bücking et al. 2018). If successful, PAT could be a useful and powerful tool for the pathophysiological study of cancers.

Second, PAT is an excellent tool for studying the longitudinal observation of an angiogenesis as well as the therapeutic response to anticancer treatment at unprecedented depth scales. Angiogenesis is known as a hallmark of cancers (Hanahan and Weinberg 2011; Pavlova and Thompson 2016; Weis and Cheresh 2011), and PAT has demonstrated its excellence for such a vasculature visualization. Although previous multiple studies demonstrated PAT's angiogenesis imaging capability, all these were limited to shallowly seated tumors, mostly based on OR-PAM or AR-PAM. However, in 2012, Laufer et al. of the Beard group demonstrated a much larger-scale visualization of angiogenesis with an acoustic diffraction-limited spatial resolution over a depth extended to ~10 mm (Laufer et al. 2012a). By using a Fabry-Pérot (FP) polymer film US sensor-based PAT system (Fig. 8g), they imaged two different types of human colorectal adenocarcinoma xenografts, LS174T and SW1222, over 12 days after the inoculation of the tumor cells into the flanks of nude mice. Briefly, the system also employed a typical wavelength-tunable optical parametric oscillator (OPO) system whose output beam with a pulse duration of 7 ns and a PRF of 50 Hz was guided to a target object via an optical fiber. However, unlike other PAT systems that used conventional piezoelectric sensors, it featured the use of the FP polymer sensor that detected generated PA waves based on the interference of an interrogation laser beam (1550 nm) reflected from the two different reflection surfaces formed by dichroic mirror coating, whose distance (or the thickness of the polymer spacer, see black circle in Figure 8g) was changed according to the varied intensity of incoming PA waves. Of course, due to the dichroic nature, the two reflection surfaces were transparent to the PA excitation laser beam over a wavelength range of 590–1200 nm.

Thus, in the sensing mechanism, the beam diameter of the interrogation laser beam determines the aperture size of the detector and also can virtually form a point detector, which can receive PA waves approaching over a much wider angle than those of conventional piezoelectric sensors. In addition, compared to the conventional piezoelectric sensor-based PAT systems, the concept of the presented system also has an advantage that it can exhibit an excellent axial-resolving ability due to its exceptionally broad bandwidth characteristics and it also allows one to achieve a very simple, but more efficient and high energy light delivery mechanism into a target object through the entire area of the transparent sensor (i.e., full-field illumination over the entire imaging zone). Consequently, the measured transverse and axial resolutions of the system were as high as 81 μm and 51 μm, respectively, which could also be conserved up to an imaging depth of 10 mm.

As revealed by the tumor imaging experimental results presented in Figure 8h, a neovascularization was commonly observed in the two tumor models as they grew, and estimated tumor sizes (volumes) also increased by approximately 50% per day; however, they exhibited somewhat different features. Compared to the SW1222 tumor (bottom row), the LS174T tumor (upper row) showed more strongly varying contrast over the entire tumor region—that is, heterogeneous vascular distribution—particularly toward the tumor center (days 7 and 8). Interestingly, from days 8 to 12, a noticeable decrease in the optical absorption was observed in the central zone, which could be attributed to a reduced blood content or possibly tumor necrosis, thereby creating an avascular region. The result was generally consistent with the findings of previous studies that were performed on the basis of vascular corrosion casting methods (Folarin et al. 2010). In contrast, in the case of the SW1222 tumor (bottom row), the development of a more homogeneous vasculature and an increase in the tortuosity of the normal vasculature surrounding the tumor was also observed (see the blue arrows in the bottom row), which was also consistent with previous studies on this type of tumor (Folarin et al. 2010).

The authors also performed another interesting experiment that illustrated the potential of PAT for evaluating the response of tumor vasculature to a therapeutic vascular disrupting agent. By using OXi4503 (combretastatin A1 diphosphate)—which is known to selectively block and destroy tumor vasculature and, thus, result in extensive central necrosis—they visualized the response of LS174T tumor after 24 h and 48 h of the administration of the drug. Note that the imaging time was determined based on the documented time course of the effects of the drug.

Surprisingly, the effect of the drug administration appeared very clearly. As illustrated in Figure 8i, the contrast of the tumor core in the 24 h image was much reduced compared to the pre-treatment image due to the disintegration of the vasculature caused by the drug; on the other hand, the tumor rim exhibited a strong image contrast, which suggested an increase in hemoglobin concentration caused by the reperfusion of blood vessels. However, after 48 h, the tumor core began to show a slight and diffusely distributed increase in the signal intensity. The authors interpreted that this might indicate an accumulation of hemoglobin due to the reperfusion of vessels in the rim that had partially disintegrated during treatment.

Thus far, in PAT researches, there have been numerous other reports of the application of PAT for such a tumor imaging study. However, as clearly evidenced in the two cases, it is undoubted that the safe, high-resolution, deep tissue imaging capabilities of PAT will provide an unprecedented research platform that enables one to longitudinally observe the progress of tumor development.

Third, PAT can also be used with a variety of contrast agents developed for molecular imaging. The two papers presented were both based on endogenous contrast mechanisms to visualize tumor vasculature. However, PAT also can be employed as a new type of molecular imaging modality (Mehrmohammadi et al. 2013; Nie and Chen 2014; Weber et al. 2016; Gujrati et al. 2017). Currently, related research is very actively growing because, compared to existing imaging modalities, PAT can provide wider options in selecting related probes based on its unique optical absorption-based contrast mechanism. Of course, it is more desirable to

visualize a tumor based on the endogenous contrast mechanism. However, this is not always possible because a large number of tumors still do not sufficiently express such chromophores that can absorb light. Thus, in order to visualize such tumors more effectively, thus far, a variety of contrast agents, such as small molecule dye- or nanostructure-based targeting probes, have been developed (Mehrmohammadi et al. 2013; Nie and Chen 2014; Weber et al. 2016; Gujrati et al. 2017). Of course, a number of these contrast agents, particularly earlier versions, were employed only to boost PA signals. However, in recent years, more sophisticatedly engineered contrast agents have been developed to target specific biomarkers—such as $\alpha_v\beta_3$ integrin (De la Zerda et al. 2008), epidermal growth factor receptor (EGFR) (Hudson et al. 2014), human epidermal growth factor receptor (HER) 2 (Li et al. 2008b), and CD44 (Swierczewska et al. 2012)—which are known to be overexpressed in numerous types of cancers.

Indeed, a great amount of effort has been made in relation to the development of contrast agents for PAT; this led to a vast number of documented papers that cannot be sufficiently covered here. Thus, in the latter part of this section, we introduce only several core papers related to reporter gene (RG) imaging—which is regarded as one of the forefronts of molecular imaging—to exemplify what kind of RG imaging approaches are possible in PAT (for more general information on PAT contrast agents, refer to refs. (Mehrmohammadi et al. 2013; Nie and Chen 2014; Weber et al. 2016; Gujrati et al. 2017).

The main advantage of in vivo RG imaging is that it enables a direct visualization of the location and level of gene expression, promoter activity, protein–protein interaction as well as more complex biological behaviors, like cell growth dynamics, by selectively encoding the genes of interest (Weber et al. 2016). In PAT, approximately two types of RGs based on enzymes and fluorescent proteins have been utilized thus far (Nie and Chen 2014; Weber et al. 2016; Brunker et al. 2017; Laufer et al. 2013).

In 2007, Li et al. of the Wang group reported the first PAT RG imaging result based on lacZ (Li et al. 2007), which is one of the most widely utilized RGs (Ghim et al. 2010). It is known that the lacZ gene encodes the enzyme β-galactosidase, which is an *Escherichia coli* enzyme responsible for lactose metabolism. In the study, by locally administrating X-gal—which consists of galactose linked to a substituted indole—to a target point of interest (i.e., near the inoculated 9 L gliosarcoma tumor expressing lacZ gene [Fig. 9a]), the authors could photoacoustically visualize the presence of the lacZ expression (Fig. 9b). It was photoacoustically possible because according to the explained role, if lacZ is expressed, the X-gal's glycosidic linkage is cleaved by β-galactosidase, a process that produced a stable dark-blue product—that is, chromophore—with a strong absorption in a red region. Note that although β-galactosidase and X-gal alone are colorless, the final product—which can be produced only when they coexist—is dark blue (Fig. 9a); thus, it can be visualized by PAT. In Fig. 9c, we present one of the core results of another report from the authors (Li et al. 2008a) in which gliosarcoma cells expressing the lacZ gene under a rat scalp and also its neighboring vasculature were clearly visualized by a dual-wavelength AR-PAM.

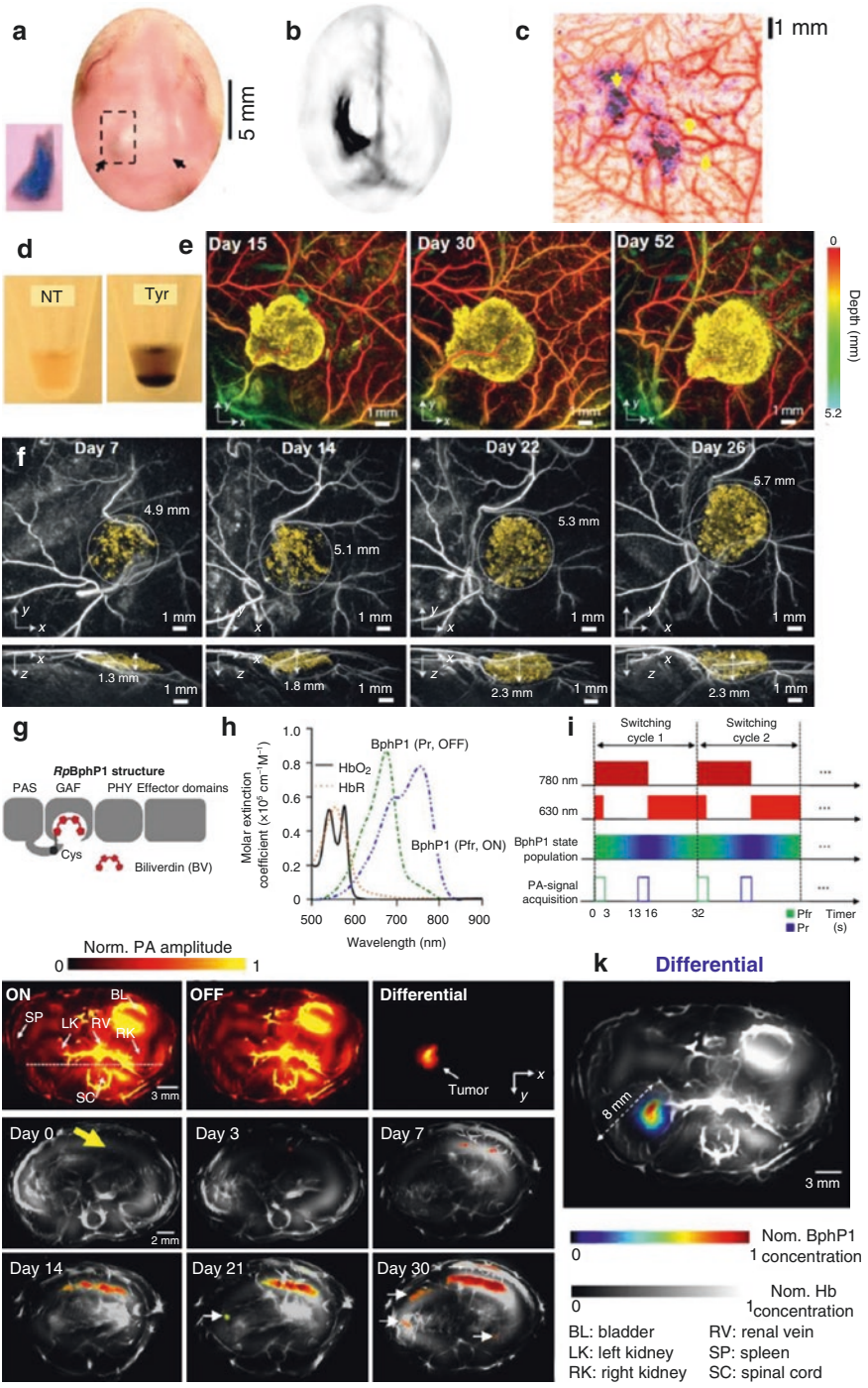
a
5 mm
b
c
1 mm
d
NT
Tyr
e
Day 15
Day 30
Day 52
Depth (mm)
0
5.2
f
Day 7
Day 14
Day 22
Day 26
4.9 mm
5.1 mm
5.3 mm
5.7 mm
1.3 mm
1.8 mm
2.3 mm
2.3 mm
g
RpBphP1 structure
PAS GAF PHY Effector domains
Cys
Biliverdin (BV)
h
BphP1 (Pr, OFF)
HbO2
HbR
BphP1 (Pfr, ON)
Molar extinction coefficient (×10⁵ cm⁻¹M⁻¹)
Wavelength (nm)
i
Switching cycle 1
Switching cycle 2
780 nm
630 nm
BphP1 state population
PA-signal acquisition
Pfr
Pr
Timer (s)
j
Norm. PA amplitude
ON
OFF
Differential
BL
SP
LK
RV
RK
SC
Tumor
3 mm
k
Differential
8 mm
3 mm
Nom. BphP1 concentration
Nom. Hb concentration
BL: bladder
LK: left kidney
RK: right kidney
RV: renal vein
SP: spleen
SC: spinal cord
l
Day 0
Day 3
Day 7
Day 14
Day 21
Day 30
2 mm

Fig. 9 Examples of representative PAT-based reporter gene imaging studies. (**a**, **b**) Photo showing an imaged rat head (**a**) and corresponding PAT image (**b**) acquired at 650 nm after the injection of X-gal (Li et al. 2007). In (**a**), the inset depicts the underside of the rat's scalp excised after sacrificing the animal. (**c**) In vivo images of lacZ-marked tumor by dual-wavelength AR-PAM (Li et al. 2008a). This is a merged pseudo-colored image of two PAM images acquired at 584 nm and 635 nm, which depict blood vessels (red) and tumor (blue), respectively. Arrows indicate the feeding vessels of the tumor. (**d**) Photos showing the pigmentation of 293 T cell pellets expressing Tyr (Jathoul et al. 2015). Left: non-transduced (NT); right: transduced with Tyr. Artificial expression of Tyr caused the pigmentation of the otherwise-transparent tumor cells. (**e**) Serial longitudinal in vivo PA MAP images (600 nm) of Tyr-expressing K562 cells after subcutaneous injection of 5 million K562 cells into the flank of a nude mouse (vasculature is color-coded for depth; K562 cells are false-colored yellow). (**f**) In vivo PA images (640 nm) of Tyr-expressing 293 T cells acquired at different times after the inoculation of 5 million 293 T cells. Dashed circles provide an indication of the increase in diameter. (**g**) Domain structure of BphP1 (Yao et al. 2015a). (h) Molar extinction spectra of HbO_2, HbR, Pfr (ON-state) BphP1, and Pr (OFF-state) BphP1. (**i**) Time sequences of the photo-switching cycle of BphP1. The 780-nm light was used for PA imaging and switching off of the protein. The PA signals were acquired only with 780-nm illumination. (**j**) In vivo whole-body PACT images of the kidney region of a nude mouse, acquired 1 week after injection of ~10^6 BphP1-expressing U87 cells into the left kidney. The differential image clearly shows the tumor in the left kidney. (**k**) An overlay of the U87 tumor (in color) in the left kidney and the blood dominated OFF-state image (in grayscale). Hb, hemoglobin. (**l**) Whole-body PACT images of the liver region of a nude mouse acquired repeatedly over 30 days after the injection of BphP1-expressing U87 cells into the right liver lobe. Differential signals (in color) are overlaid on top of the structural signals from the blood (in grayscale). The white arrows in the images for days 21 and 30 indicate secondary tumors due to metastasis

Here, an important thing that must be noted is that a single β-galactosidase molecule can cleave multiple X-gal molecules and produce a large number of blue products. Although this could have a positive implication that the method could enable the detection of a low-level expression of lacZ because the related process could be understood as a kind of signal amplification, the downside is that a 1:1 stoichiometric mapping between the amount of detected blue products and the level of RG expression is fundamentally impossible. Moreover, another big disadvantage of this method is that it requires the local injection of an exogenous chromogenic substance (X-gal) into the region of interest and this process may not lead to a systemic delivery.

Another well-known enzymatic approach in PAT is the tyrosinase (Tyr)-based reporter system (Jathoul et al. 2015). Since Tyr plays the role of catalyzing the formation of the dark brown pigment eumelanin from cellular tyrosine, the mechanism can be utilized for an artificial PAT contrast creation by genetically expressing it. By creating a novel retroviral vector that co-expressed Tyr and a surface marker gene (dCD34) in the two types of human cancer cell models (K562 and 293T), Jathoul et al. of the Beard group successfully demonstrated in vivo longitudinal imaging of their growths in the flanks of nude mice over the longest period (52 days) ever achieved. They co-expressed the dCD34 gene to facilitate the easy selection of the tumor cells during the long-term cultures of the cell lines and the Tyr gene to create a PAT image contrast for the inoculated tumors, as mentioned earlier. Figure 9d

illustrates the photos of 293 T cell pellets without (left) and with (right) expressing Tyr. For the experiment, they utilized the FP US sensor-based PAT system, as depicted in Figure 8g. Figure 9e and f depicts the longitudinal imaging results of the growth of K562 and 293 T tumor cells.

Previously, several studies also have employed Tyr for PAT (Paproski et al. 2011; Krumholz et al. 2011; Stritzker et al. 2013; Qin et al. 2013; Paproski et al. 2014). However, the greatest advancement of the presented report was that they achieved a greatly extended longevity of the Tyr-expressing tumor in living mice, which extended up to >7 weeks (Fig. 9e). Moreover, although the inoculated tumor xenograft was genetically engineered, it was evident that the entire volume of the 293 T tumor cells increased by 38% over a period of 26 days (Fig. 9f). Basically, such achievements were possible because these studies developed a novel retroviral vector that enabled a stable transduction in which the cell genome was permanently altered so that the changes were passed to progeny cells, thereby resulting in the continuous production of PA image contrast caused by the steady increase in tumor cell populations. As long-lived high contrast is essential for numerous practical biological applications, like visualizing cell growth as presented, the study suggests that retroviral-mediated expression of Tyr can provide high expression levels and also be well tolerated with little effect on cell viability.

In addition to the biological implications, the report has another important technical implication—high-resolution three-dimensional imaging of the genetically labeled cells was achieved at depths approaching 1 cm with unprecedented image quality, which is not possible with other optical imaging modalities even now.

As presented, the Try-based RG system exhibits a high detection sensitivity based on the intrinsic signal amplification mechanism. Moreover, unlike the lacZ-based enzymatic approach, the tyrosinase RG system does not require an exogenously administered substrate and, thus, related approaches could address potential toxicity concerns. However, the introduced two enzymatic reporter systems are basically less desirable because they are regarded as indirect methods—which depend on substrate availability—and, thus, limit quantification. In addition, melanin's featureless broad absorption spectrum makes it difficult to be effectively discriminated from intrinsic background signals generated by hemoglobin (Weber et al. 2016; Brunker et al. 2017; Laufer et al. 2013).

Due to the limitations of the enzymatic reporters, a new form of approaches based on nonenzymatic reporters—such as fluorescent proteins, nonfluorescent chromoproteins, and photoswitchable nonfluorescent proteins—has been actively explored in recent years and is attracting increased attention (Weber et al. 2016; Brunker et al. 2017; Laufer et al. 2013). As a direct method expressing RGs, such a protein-based approach enables a 1:1 mapping of the expression level of the protein of interest and also enables one to take advantage of using various proteins already available in the class.

In this context, there was a report that exploited eGFP (enhanced green fluorescent protein) and mCherry—well-known fluorescent proteins—for a PAT-based RG imaging study (Razansky et al. 2009). However, the limited penetration capability of light at the absorption peaks (488, 587 nm) of the two proteins made them applicable

only to the two small size organisms, *Drosophila melanogaster* pupae and adult zebrafish. Subsequently, in order to overcome the issue related to the undesirable spectral properties of these fluorescent proteins, more red-shifted fluorescent proteins, like iRFPs, began to be employed for PAT since 2012 (Filonov et al. 2012). Obviously, the iRFPs are better suited for related applications because they are derived from bacterial phytochrome photoreceptors (BphPs), which are generally known to exhibit relatively low fluorescence quantum yield and a high intrinsic extinction coefficient compared to GFP-like proteins as well as to have ideal spectral properties that absorb far-red light due to the incorporation of biliverdin IXα (BV).

In the related class, iRFP 713 (also simply called iRFP) with a peak absorption of 690 nm was the first one to be utilized for the related approach, followed by two variants iRFP 670 and iRFP 720 that have peak absorptions of 645 nm and 703 nm, respectively (Krumholz et al. 2014). However, although the two papers were those that employed BphPs for PAT for the first time, the developed probes did not relate to such an optical switching mechanism of BphP, as demonstrated by the following paper.

In 2015, Yao et al. of the Wang group reported an important achievement that harnessed the reversible optical switching mechanism of BphP1 to enhance the detection sensitivity of PACT at large depths as well as to achieve a super-resolution OR-PAM imaging (Yao et al. 2015a). BphP1 is a nonfluorescent BphP from the bacterium *Rhodopseudomonas palustris* (BphP1 is a short name for *Rp*BphP1). Interestingly, as with all canonical natural BphPs, it also exhibits very interesting photochromic behavior: it undergoes reversible Pfr → Pr photoconversion (i.e., *trans* to *cis* conformation) upon 730–790 nm light irradiation and Pr → Pfr photoconversion (i.e., *cis* to *trans* conformation) upon 630–690 nm light irradiation. Here, the two states Pr and Pfr are named according to the meaning "pigment red absorbing" and "pigment far-red absorbing," respectively; the two conformational states are the result of the photoisomerization of BV. Notably, due to the photoconversion, the two states exhibit different absorption spectra, where the Pr state has a dominant absorption at 670–700 nm (the Pr state) and the Pfr state at 740–780 nm.

It is known that BphPs consist of two key elements: a photosensory core module (PCM) and an output effector domain (Fig. 9g). The PCM is further divided into the three protein domains PAS, GAF, and PHY; these are connected with an α-helix linker, and inside a chromophore-binding pocket of the GAF domain, photoisomerization of the BV—which is covalently attached to the cysteine (Cys) residue of the PAS domain—leads to the two conformational states called Pfr and Pr. In the unbound state, switching does not affect the absorption properties of BV even though photoisomerization occurs; however, when covalently bound to the protein barrel, the two conformational states exhibit the distinct absorption spectra, as illustrated in Fig. 9h, in which the Pfr state is called "the ON state" and the Pr state is referred to as "the OFF state." The Pfr state is also regarded as "the ground state," because although BphP1 is photoswitched to the PrF state, it naturally relaxes back to the Pfr state with a half-life of ~210 s.

In the report, the authors utilized the interesting on/off switching mechanism of BphP1for the in vivo differential imaging of BphP1-expressing U87 glioblastoma

cells injected into the left kidney of a nude mouse 1 week ahead. According to the time sequences presented in Fig. 9i, the animal was irradiated with 630 nm and 780 nm and then the PA images were acquired. Here, it is important to note that the PA images were acquired only with 780-nm excitation, although the times sequence shows that during the PA signal acquisition period, the 630-nm light was also fired—that is, in each switching cycle, the 630-nm illumination (16 s) was not for PA signal generation but only for inducing the Pr → Pfr photoconversion, whereas the 780-nm illumination (16 s) was for PA signal generation as well as the Pfr → Pr photoconversion. Consequently, they could acquire the two sets of 780 nm-excited PA images of BphP1-expressing glioblastoma in the two different states (ON and OFF) of BphP1.

Since the two PA image data sets were at the same 780-nm wavelength, it was possible to accurately extract only the tumor signal by simply subtracting the two data sets pixel-wise (Fig. 9j). Figure 9k illustrates the extracted tumor image overlaid on the OFF-state PA image that depicts blood vasculature. Indeed, the showcased differential imaging concept is a very important demonstration that illustrates another technical scope of PAT in relation to contrast creation. Even though a local optical fluence information is completely unknown due to the inhomogeneity of intervening complex biological tissues and also the PA signal change at the two different states is obscured by the overwhelming background vascular signals, it was possible to accurately separate only the reporters' signals that came from large depths approaching ~10 mm. Based on the same method, they were also able to successfully visualize the growth and metastasis of the glioblastoma tumor—which was originally inoculated into the right liver lobe of a mouse—for over 30 days (Fig. 9l), and also the mouse brain with a glioblastoma located at ~3 mm beneath the scalp surface (not presented here). Moreover, by applying a similar principle, they achieved a super-resolution PA imaging with a lateral/axial resolution of ~141 nm/400 nm (not presented here).

After the first demonstration was presented, the same group as well as other groups also presented more advanced photoswitchable probes—such as DrBphP (Li et al. 2018a) and sGPC2 (Chee et al. 2018)—which exhibited more improved performance and/or other optical characteristics. As the concept provides a new research paradigm in PAT-based RG imaging, it goes without saying that this is likely to lead to numerous important new findings and follow-up technical advances.

In this section, several notable examples of PAT related to cancer research have been introduced. As evident, related examples have a close relation to the previous two sections. In short, based on the multi-scale, multi-contrast, real-time RG imaging capability of PAT, various forms of cancer research can be realized not only in the illustrated areas but also over the entire brain and whole-body areas of small animals. Moreover, although not sufficiently covered in this section, the relatively wider options in creating endogenous contrasts as well as the great flexibility in engineering dedicated contrast agents for PAT is also likely to have a profound impact in clinics by presenting viable solutions against issues of toxicity and insufficient targeting ability of conventional contrast agents developed for other imaging modalities.

Other Notable Biological Applications

In relation to the small animal whole-body imaging capability of PAT, there is another important application that needs to be noted. The examples presented in the previous section mostly showcased how PAT could be utilized for disease models-based preclinical studies, especially focusing on cancer application. However, PAT is also expected to open a new research paradigm in developmental biology based on the safe and real-time, deep imaging capabilities, which however cannot be provided simultaneously in conventional imaging modalities (Ripoll et al. 2015; Laufer et al. 2012b).

As depicted in Fig. 10, Laufer et al. of the Beard group demonstrated longitudinal visualization of organ and vascular genesis during embryo development in a pregnant mouse (Laufer et al. 2012b). Very surprisingly, numerous details of several major organs—such as heart, liver, umbilical cord, and many other major vessels—were clearly visualized even in the noninvasive in vivo imaging, which was performed via the abdominal wall of the mother mouse. Further, in another experiment performed ex vivo within one hour after the sacrifice of the mother mouse, since no

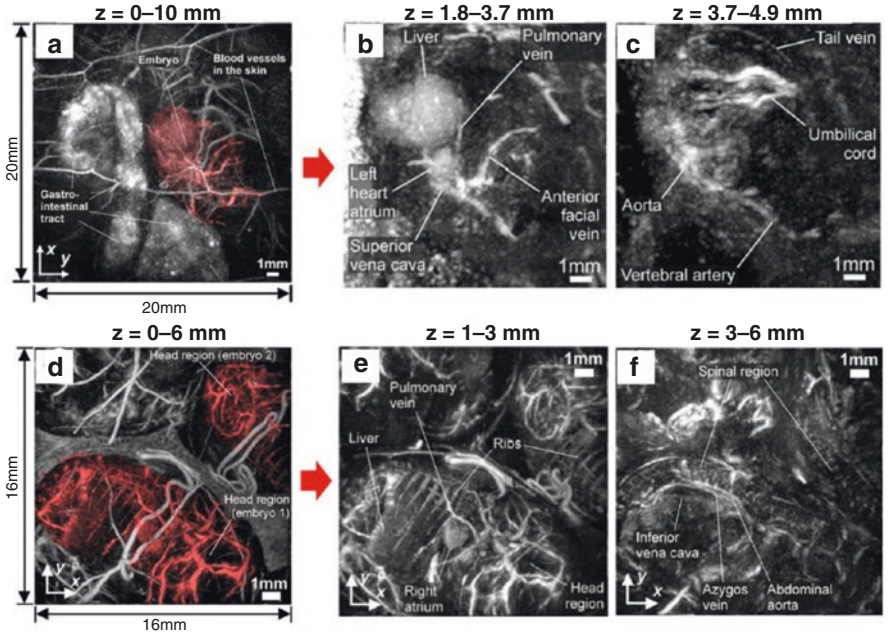

Fig. 10 In situ PAT images (640 nm) of the abdomen of pregnant female mice (Laufer et al. 2012b). (**a**) In vivo MAP of a 3D image data set of the abdomen of a pregnant mouse (E15.5) containing a single embryo. (**b**) MAP for z = 1.8 to 3.7 mm, (**c**) MAP for z = 3.7 to 4.9 mm. (**d**) MAP of the complete 3D image data set (z = 0 to 6 mm) obtained from the abdomen of a pregnant mouse containing two embryos (shaded red). (e) MAP for z = 1 to 3 mm. (f) MAP for z = 3 to 6 mm

motion artifact was involved, the PAT system enabled the visualization of a large number of additional details related to smaller vessels, like Azygos vein, and not only related to major organs, such as the spinal cord, ribs, and right atrium.

Although the presented demonstration was based on the FP US sensor-based PAT system, which has not yet sufficiently advanced to provide real-time imaging, the authors presented a feasible projection that related imaging approach could also be applied to such applications as the longitudinal imaging studies of transgenic mouse embryos, in which specific genetic knockouts induce heart and vascular malformations. Since all such studies are currently performed ex vivo based on MRI or optical projection tomography—which require extensive preparation of the excised embryos and also may involve the draining of blood and the use of contrast agents, such as gadolinium or fluorescent dyes—it is highly expected that the new technical addition provided by PAT could have profound impact on various developmental biological studies (Laufer et al. 2012b).

Clinical Applications

The key benefit of the clinical application of PAT is that its related systems are compatible with conventional US imaging functions. Although a number of previous biological applications also demonstrated the capability of combined PA and US imaging, since the inherent integration benefit—apart from the functional and molecular imaging capability—was more pronounced in clinical applications, it must be importantly evaluated as the core technical aspect that could make PAT more easily acceptable in clinics. Needless to say, US imaging already occupies a solid position in clinics as many of its related procedures are regarded as gold standards. Thus, PAT's compatibility with US complements the weaknesses of US and doubles the value of the technology.

Thus far, the clinical applications of PAT have been pursued over various application areas. However, considering the number of publications and likelihood of success, we selected several major application areas and made the following subjective categorization: 1) breast cancer diagnosis, 2) dermatological application, and 3) endoscopy and minimally invasive imaging application. In addition to those, we allotted a fourth topic called PA angiography and lymphangiography because several studies related to this topic have reported very promising results.

Breast Cancer Diagnosis

The application of PAT for breast cancer imaging has been a major topic of interest since the inception of the technique in the 1990s (Esenaliev et al. 1997; Oraevsky et al. 1999; Kruger et al. 1999a, b); it has played a leading role in PAT development, as numerous important breakthroughs associated with imaging performance, such as imaging depth, were achieved in relation to this application. However, it must be noted that although over 30% of all PAT papers pursuing clinical applications disclosed research objectives addressing this application, thus far, real images of

human breasts have been mainly reported by two PAT pioneers and several other research groups that emerged later; In other words, most of the research from other groups were limited to animal-based studies associated with disease models or contrast agent developments. This feature can probably be explained by the fact that related study requires a long technical accumulation and a number of expensive system elements, such as high-power laser, array transducer, and multichannel DAQ. Thus, in this section, we introduce related technological developments, focusing on the results reported by several major research groups.

The first case that applied PAT to breast cancer diagnosis was presented by Oraevsky and Kruger in the 1990s (Esenaliev et al. 1997; Oraevsky et al. 1999; Kruger et al. 1999a, b), and thereafter, the two researchers made many important initial contributions to the development of clinical breast imaging systems up to 2013. Meanwhile, in 2004, Manohar and Steenbergen et al. also appeared as new players and began reporting their work on system development (Manohar et al. 2004; Manohar et al. 2005). In short, until 2013, these were the three main researchers reporting their works on system developments for practical clinical translation.

The first paper on real human breast image production appears to be the one reported by Oraevsky et al. in 1999 (Oraevsky et al. 1999). In this work, they presented the first human breast image ex vivo and also reported the important observation that PA image contrasts between tumors and normal tissues were as great as ~300% and also much greater than those of conventional ultrasonography, MRI, and X-ray mammography images, which were acquired concurrently. Although it was performed ex vivo, they conjectured that the strong contrast was attributed to the dense microvascularity of the tumors because the imaging was performed within the first 10–20 min after harvesting tumor-bearing breast samples from a radical mastectomy. In the report, they named the system the laser optoacoustic imaging system (LOIS), and it was equipped with a 12 element-based linear array transducer (0.05–3 MHz, polyvinylidene difluoride (PVDF)) and 1064-nm laser system.

In the next year, the group presented another report on a second-generation breast imaging system named LOIS-2 (Andreev et al. 2000). The system was also constructed based on a PVDF-based array transducer. However, the number of detection channels in the array transducer was greatly increased to 32, and the array had an arc-shape rather than the previous linear shape. It was an important modification, and its particular geometric features have been adopted in many other PAT systems from other groups.

Almost one decade later in 2009, the group reported the latest version of the arc-array transducer-based LOIS along with the results of a pilot clinical study obtained from 27 patients (Ermilov et al. 2009). It appears to be the first clinical study that involved such a large number of subjects.

Figure 11a shows a schematic of the latest system in which the number of the detection channels of the arc-array transducer was further increased to 64 (Fig. 11b) from the previous 32, and the laser illumination was provided from one side by busing an optical fiber bundle. The updated configuration made it possible to acquire a single slice breast image in vivo in a fashion similar to craniocaudal or mediolateral projection, with a spatial resolution that was better than 0.5 mm. To excite the breast

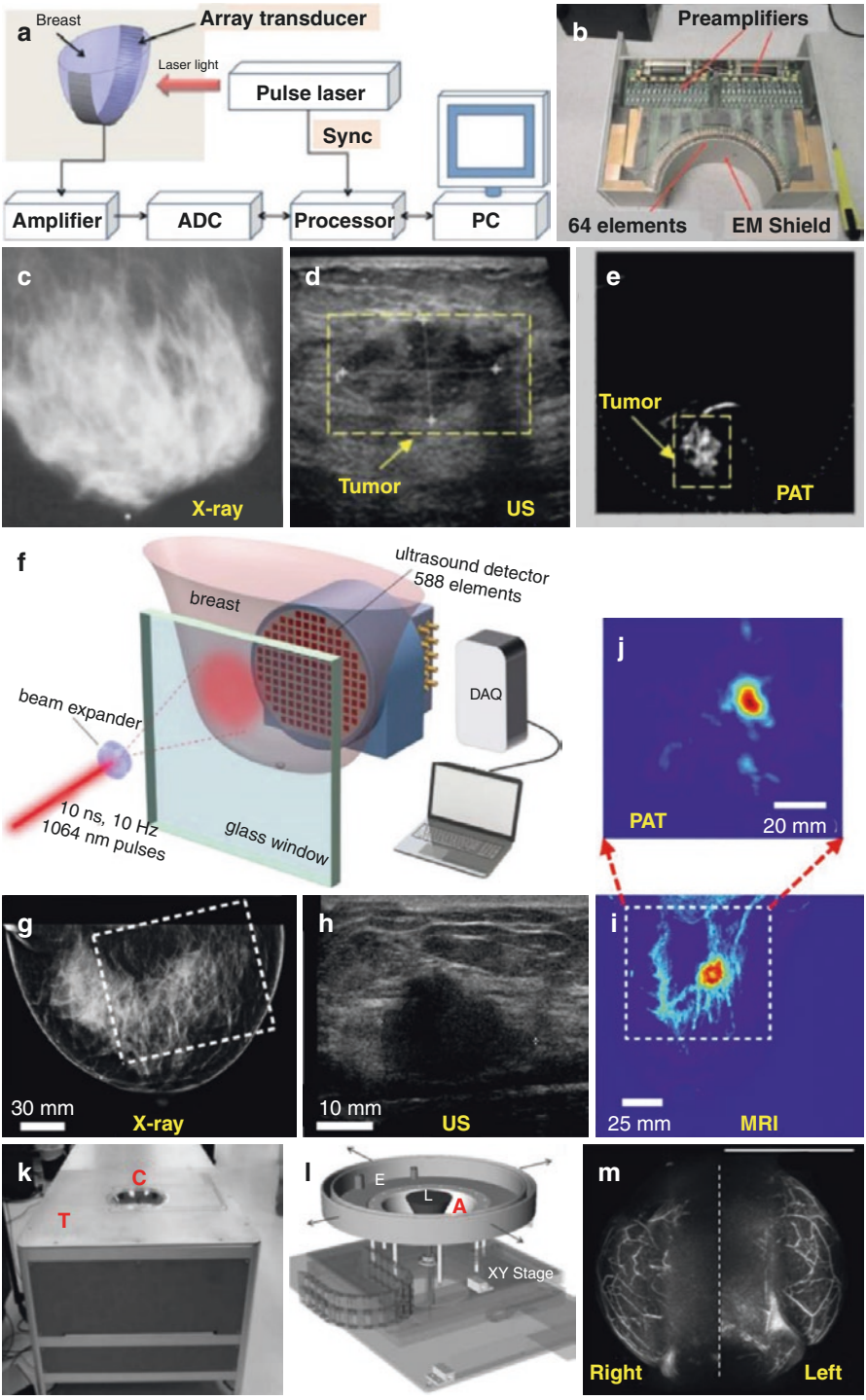
a
Breast
Array transducer
Laser light
Pulse laser
Sync
Amplifier
ADC
Processor
PC
b
Preamplifiers
64 elements
EM Shield
c
X-ray
d
Tumor
US
e
Tumor
PAT
f
ultrasound detector
588 elements
breast
beam expander
DAQ
10 ns, 10 Hz
1064 nm pulses
glass window
j
PAT
20 mm
g
30 mm
X-ray
h
10 mm
US
i
25 mm
MRI
k
C
T
l
E
L
A
XY Stage
m
Right
Left

Fig. 11 PAT breast imaging systems and imaging results from related pilot clinical studies performed based on the systems. (**a**, **b**) Schematic (**a**) of a 64-element arc-shaped array transducer-based breast imaging system (LOIS-64) and a photo (**b**) of the employed array transducer (Ermilov et al. 2009). (**c**–**e**) A set of imaging results acquired from a malignant tumor based on conventional X-ray mammography (**c**), US (**d**), and LOIS-64 (**e**). High contrast of the object in the PA image (**e**) implies the advanced angiogenesis indicative of a malignant tumor. (**f**) Schematic of the 2D 588-elements US array transducer-based PA breast imaging system (Heijblom et al. 2015). (g–j) A set of imaging results acquired from a patient with IDC (grade 3 of 19 mm) based on conventional X-ray mammography (**g**), US (h), MRI (**i**), and PA MAP image (**j**). The X-ray mammogram (**g**) did not show any abnormalities, whereas the US image (h) revealed a highly suspect image contrast for the 22-mm palpable mass. The white boxes in (**g**) and (**i**) indicate the FOV of the PA image presented in (**j**). (k) Photo of the hemispherical detector array (HDA)-based PAT breast imaging system depicting the exam Table (T) and the breast positioning cup (C); the HDA is located below this (Kruger et al. 2013). (l) Schematic depicting the HDA (A) mounted on an XY-translational stage. (m) Medial-lateral MAP image of the right- and left-breasts of a healthy volunteer with known mammographic breast density (heterogeneously dense) and brassiere cup size (D cup), which was acquired by the system (**k**)

tissue, a 757-nm laser beam with a single pulse energy of approximately 380 mJ was employed, and it was uniformly expanded over a 70-mm diameter area on the breast surface, which yielded an optical fluence of 10 mJ/cm^2.

In addition to the system result, they also accomplished a very promising outcome from the clinical study: They successfully visualized 18 malignant tumors out of 20 (based on the number confirmed by biopsy) using LOIS, excepting those cases in which PA images could not be obtained due to technical issues. Importantly, among the 18 visualized tumors using LOIS, five were not seen on X-ray mammography images, whereas only one tumor was seen on the mammography image. Figure 11c–e shows an example in a breast cancer case that eventually turned out to be a poorly differentiated infiltrating ductal carcinoma grade 3/3 (according to the biopsy). As shown in Figure 11c, the tumor could barely be localized on the mammography image acquired from the radiologically dense breast, whereas it was clearly visualized in the PA image (Fig. 11e). The US image (Fig. 11d) also helped to identify a 23 × 15 mm size tumor located at the depth of ~21 mm; however, the tumor margins were not clear. Furthermore, the tumor contrast in the US image was lower than that in the PA image, a result that was attributed to the strong signal generation by the associated microvasculature.

In 2004, Manohar et al. of the Steenbergen group in the Netherlands reported a different type of breast imaging system that was designed to image an entire breast based on parallel plate geometry (Manohar et al. 2004). Since then, the group has made continuous reports on the progress of related system development until the mid-2010s. In 2007, they also reported their first human breast imaging result obtained by the system from 13 subjects (Manohar et al. 2007); however, here we introduce their later report published in 2015 (Heijblom et al. 2015) since it was more comprehensive.

Figure 11f depicts the latest version of the related system reported in 2015 as described earlier; its basic configuration and key elements have remained almost the same since the first published paper (Manohar et al. 2004), except the increase in the

number of detection channels of the engaged DAQ system. The main feature of the system is the use of a 2D US detector array consisting of 588 elements distributed over an 85-mm diameter area (pitch: 3.175 mm). As a result, they could achieve a relatively larger FOV (90×85 mm^2) compared to those of other groups. The size of each element was 2×2 mm^2, and a vast number of detection channels could be created by forming corresponding electrodes on the surface of a 110-μm thick PVDF film, which yielded a center frequency of ~1 MHz. For breast imaging, the target was gently pressed between the disc-shaped transducer and a glass window and then photoacoustically excited by a 1064-nm laser beam (~350 mJ) over a 35-mm^2 illumination area.

With this system, they performed a pilot clinical test that imaged 29 human subjects with symptomatic breast malignancies. Then, they compared the acquired PA images with conventional X-ray and US images and also with MRI and vascular staining histopathological images for subsets of cases. Surprisingly, they acquired a promising result that successfully identified lesions in suspect breasts at the expected locations in 28 out of 29 cases. Moreover, they also made the crucial observation that the PA contrast of the lesions was independent of the conventional mammographically estimated breast density, whereas there was a significant drop in lesion contrast in X-ray mammography for high-density breasts compared to low-density breasts.

In addition, a large number of other important findings and conclusions were reported in the paper. Among these are a set of results that correspond to the aforementioned observation and are presented in Figure 11g–j. The data were obtained from a subject with a past history of infiltrating ductal carcinoma (IDC), which was also confirmed by histopathological analysis in the study. However, as shown in Figure 11g, no abnormalities were observed in the X-ray image, whereas the US image (Fig. 11h) revealed the presence of an unsharply delineated, irregular, hypoechoic mass that was 22 mm, which was highly suspected of malignancy as per the US evaluation. Thus, they decided to proceed to an MRI and PA examination, from which they were able to identify that the PAT image (Fig. 11j) could accurately delineate the highly vascularized region, as with the MRI image (Fig. 11i). Although the individual blood vessels were not visualized in their PA images due to the relatively poor spatial resolution (~3.5 mm) of the system, they attributed the acquired high contrast production to the increased vascularity inside the tumors as it could be confirmed by the immunohistochemistry analysis based on CD31 staining.

As mentioned earlier, Kruger also pioneered PAT since the beginning by making many initial crucial contributions to instrumentational and theoretical works (Kruger 1994; Kruger and Liu 1994; Kruger et al. 1995). In particular, he reported the first prototype of PAT image reconstruction algorithms (Kruger et al. 1995). Furthermore, for breast imaging applications, he suggested the hemispherical detector array (HDA)-based signal detection concept for the first time (Kruger et al. 1999a, b). Among many of his important papers, we mention only three papers.

First, in his 2000 paper (Kruger et al. 2000), Kruger et al. reported the first in vivo human breast images acquired from five subjects. Notably, they acquired the images by employing a 434-MHz, high power (25 kW peak power) radio wave generator rather than a typical pulsed laser. Thus, the related concept was termed thermoacoustic tomography by the researchers. Although the images were poorer than those in his subsequent papers, this paper was the first to present in vivo breast images over the

entire PAT area. Approximately one decade later, Kruger et al. disclosed a new version of a breast imaging system that was constructed based on a pulsed laser, and they published two studies in 2010 (Kruger et al. 2010) and 2013 (Kruger et al. 2013), in which a different scanning mechanism and a different number of transducer elements were applied. Although the former paper was also technically important, we focus here on the second paper (Kruger et al. 2013) because it presented 3D breast vasculature images with superior quality compared to any other system reported so far at that time.

Figure 11k depicts the system reported in the paper. Basically, the overall system configuration and scanning mechanism were inherited from its former version (Kruger et al. 2010). However, in this study (Kruger et al. 2013), they greatly improved the spatial resolution and FOV by employing a 512-elements array transducer (2 MHz) and performing a spiral scan, which differed from the former 128-element (5 MHz)-based rotational scanning mechanism (Kruger et al. 2010). The main advantage of the spiral scanning method lay in its flexibility in setting the lateral FOV, which can be set arbitrarily, exceeding the demonstrated size in the paper (i.e., 24 cm in diameter), while conserving the uniform spatial resolution of ~0.42 mm over the imaged volume. The schematic presented in Figure 11l was the key module that enabled the spiral scanning.

Figure 11m depicts one of the representative images acquired from four subjects. Surprisingly, vasculature details even at a depth of ~4 cm were clearly visualized using a laser pulse energy of ~280 mJ (756 nm) irradiated to the breast over a 60-mm diameter area and then collecting PA data over the described detection points. Previously, the researchers also claimed a similar imaging depth. However, the visualized vasculature was not as detailed and global as the presented image. Indeed, the paper represented a great achievement, demonstrating that the developed system could image breasts up to the DD cup size, which accommodates 90% of all women in the United States.

Meanwhile, in 2014, a Japanese group teamed with Canon Inc. reported the results of a clinical study that was conducted using their first prototype named PAM-01 (Kitai et al. 2014). The overall configuration of their first version was similar to that of the Netherlands group (Heijblom et al. 2015) in terms of the imaging concept, where an imaged breast was placed between two parallel plates. However, they applied a different illumination scheme that adopted dual-side illumination, in which another illumination was provided around the detector made of a 15 × 23 matrix array (1 MHz). Consequently, their imaging resolution was much better (~2 mm) than that of the Netherlands group and could also successfully visualize breast cancer lesions in 20 out of 27 subjects. More comprehensive results were reported in their other paper published in 2015 (Fakhrejahani et al. 2015). After the study, the group also reported another improved version of the system (named PAM-02). It featured an advanced imaging performance capable of providing PA and US images simultaneously with an improved spatial resolution, and it also produced a sO_2 image (Asao et al. 2016).

However, in the most recent paper published in 2017, with Toi as a lead author (Toi et al. 2017), the group reported an achievement that could be considered one of the most significant advancements in the practical clinical translations of the PAT breast imaging applications. In the report, they also released their new imaging setup (named PAI-03) and reported another pilot clinical study result acquired from

22 subjects with malignancies based on the new system. However, in the new study, they could acquire much clearer 3D vasculature images than the previous one (Asao et al. 2016) because they changed their system concept to the HDA-based breast imaging concept that was originally proposed by Kruger et al. (Fig. 11k).

Figure 12a and b–c respectively show the new PAT system developed for the study and a representative imaging result (PA and MRI images) acquired from a subject. As shown in the PA (Fig. 12b) and MRI (Fig. 12c) images acquired from the same area of a normal breast, the PAT system could depict detailed 3D vasculature and blood vessel branching structures along with morphological characteristics much better than conventional MRI based on standard contrast-enhanced imaging. The superior imaging performance was also evident in tumor regions, as shown in a

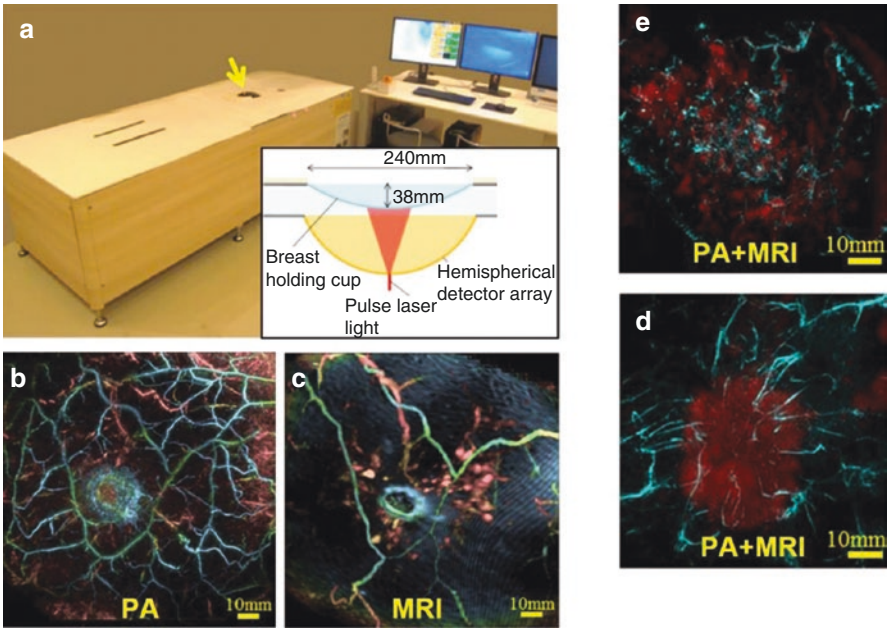

Fig. 12 PAT breast imaging systems and imaging results from related pilot clinical studies performed based on the systems. (**a**) Photo of the HDA-based PAT breast scanner (PAI-03) developed by Toi et al. (Toi et al. 2017). (**b**) PA image acquired from a normal breast. (**c**) Standard contrast-enhanced MRI image acquired from the same area of (**b**). (d) PA and MRI fusion image acquired from a 40-year-old woman with IBC (tumor is 47 mm in diameter). (**e**) Another PA and MRI fusion image acquired from a 46-year-old woman with DCIS; this reveals a trend toward increased identification of spotty intra-tumoral signals. (**f**) Photo of the dual-modality PA and US imaging system embodied by modifying a clinical US system (Garcia-Uribe et al. 2015). (**g**) Photo of the imaging probe, in which two fiber bundles were added on the two sides of a clinical linear array US probe. (**h**) An illustration showing the PA and US image-guided fine needle aspiration biopsy of an SLN. (**i**) Co-registered PA and US image of an SLN. (**j**) Schematic of the 512-element full-ring array transducer-based PAT breast imaging system (Lin et al. 2018). (**k**) Representative results were acquired from two breast cancer patients with radiographically dense breasts. Images from the left to right columns: X-ray mammography images; depth-encoded PA images; PA MAP image presented in sagittal planes marked by white dashed lines in the depth-encoded PA images; PA images showing the contrast-boosted tumors after applying the vessel density calculation algorithm (tumors are identified by green circles, and background images in grayscale are the MAP of vessels that lie deeper than the nipple)

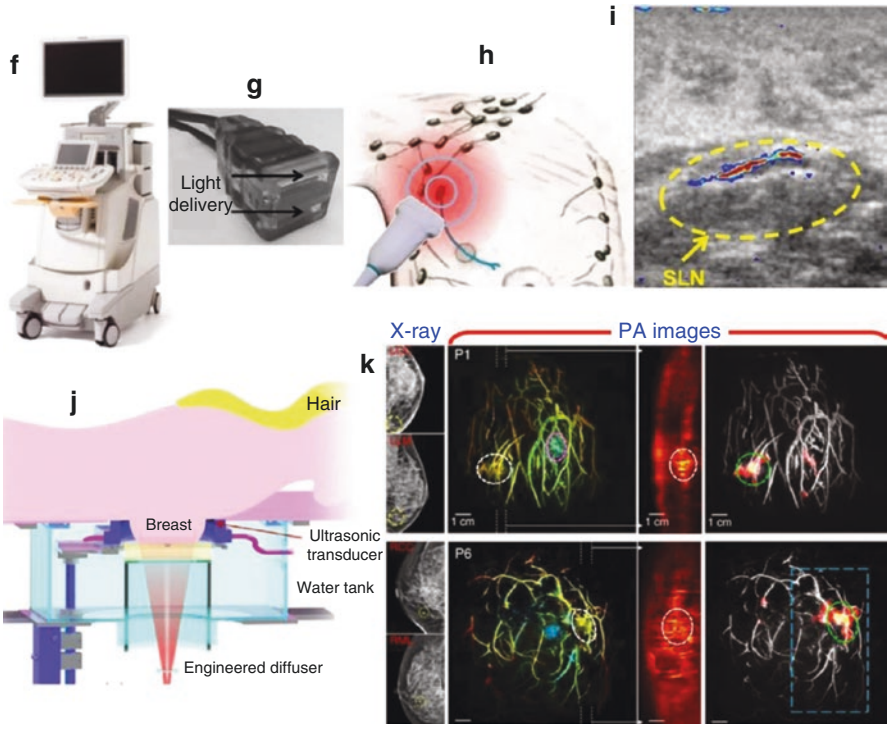

Fig. 12 (continued)

representative image (Fig. 12d) acquired from another subject with invasive breast carcinoma (IBC). Such high-quality vasculature images could be acquired because they adopted the HDA-based signal detection concept in which 512 US transducers (2 MHz) were engaged. Based on the system presented in Figure 12a, PA spatial resolutions were 0.57 mm along the horizontal plane and 0.37 mm along the gravitational direction.

In addition to substantial improvement in the imaging performance, they also reported many interesting findings obtained from the 22 subjects, including five cases of ductal carcinoma in situ (DCIS) and 17 cases of IBC and general conclusions derived from them. Among them, the notable ones were as follows: (1) More blood vessels were observed in the tumor-bearing breast than the contralateral side in most cases; (2) peritumoral vasculature was detected in 86% of all cases; (3) in IBC cases, most tumor-related blood vessels were centripetally directed toward the tumor (Figure 12d corresponds to a related example), and 93% of centripetal blood vessels appeared to be disrupted or rapidly narrowed at the tumor boundary; (4) a significant difference was observed between DCIS and IBC in terms of the vessels' centripetal vascularity; IBC cases tended to have a centripetal blood vessel structure (Fig. 12d), whereas there was a trend toward increased identification of intratumoral spotty signals among the five DCIS cases (Fig. 12e). In addition, although there was only one case, they observed one interesting phenomenon: Fine intratumoral blood

vessels were visualized after chemotherapy, whereas no significant change in tumor size was detected in US imaging.

The reported results represent an important achievement highlighting the diagnostic value of PAT. According to the authors, with the employed laser pulse energy of ~200 mJ, the maximally imageable depth of the system was ~30 mm, although this is somewhat underestimated.

Another notable achievement in the breast imaging application of PAT related to the sentinel lymph node (SLN) mapping in breast cancer, which was investigated by the Wang group. Prior to the study in 2008, the group also demonstrated PAT-based SLN mapping in a rat model for the first time by using methylene blue as a contrast agent (Song et al. 2008).

In the lymphatic system, SLN is defined as the first node that drains from a primary tumor. From a practical perspective, its location can be determined based on the finding that an injected agent such as radioactive isotopes or other blue dye is taken up into the node in a manner similar to how tumor cells travel from the primary tumor. Thus, the first lymph node or cluster of lymph nodes where the dye is taken up represent the SLN. In clinical settings, SLN is crucial in terms of cancer staging because it guides the patient prognosis and treatment strategy based on biopsy results: that is, if tumor cells are found in an SLN, it means that the tumor has already metastasized from the primary tumor.

To demonstrate PAT's advantage in finding an SLN and guiding the related biopsy, Garcia-Uribe et al. of the Wang group developed a dual-modality PA and US imaging system by modifying a clinical US imaging system (Fig. 12f) and implementing an imaging probe (Fig. 12g), and they reported their first pilot clinical study result in 2015 (Garcia-Uribe et al. 2015). In the study, methylene blue dye with a peak absorption wavelength of 665 nm was employed as the contrast agent to visualize the SLNs stained by it (Fig. 12h), and a laser wavelength (667 nm) near the peak wavelength was chosen.

Excepting two cases in which the system malfunctioned, 16 women who had pathologically proven breast cancer and thus were scheduled to have an axillary lymph node dissection participated in the study and underwent SLN biopsy under the guidance of the developed system. Figure 12i shows a typical co-registered PA and US image in which the colored area corresponds to the SLN visualized by PAT imaging. Under the guidance of the system, they performed percutaneous needle biopsies after deploying a single titanium marker clip via a needle for 13 cases. Among them, the presence of the marker clip in the surgically removed SLN specimen could be confirmed in six cases.

Beginning with the SLN imaging project, the Wang group more aggressively pursued breast imaging application, and in 2018 the group reported a new type of imaging system that significantly improved spatiotemporal resolution by employing a full-ring 512-element ultrasonic transducer array (2.25 MHz) (Fig. 12j) (Lin et al. 2018). Although many of the aforementioned studies also demonstrated the imaging of a whole breast (Kruger et al. 2013; Toi et al. 2017), the imaging speeds of their systems were relatively slow due to the limited capacity of the employed DAQ or scanning mechanism. However, this new system enabled full 3D imaging of a breast within the approximate scanning time of a single breath hold (~15 s) by employing vast numbers of DAQ channels that were mapped to all the elements one by one. In

the reported version, the scanning time was a kind of minimum time required to acquire a complete volumetric data set by adding additional mechanical translational motion to the array transducer along the elevational direction under the limited PRR (10 Hz) of the employed laser system. However, 2D cross-sectional imaging speed itself was as fast as 10 Hz.

As with the Kruger (Kruger et al. 2013) and Asao (Toi et al. 2017) groups' systems, their new imaging system was also able to provide a vasculature image of a full breast in 3D, and it was also able to depict vasculature details in a tumor region as fine as 255-μm along the transducer array plane; however, the image resolution along the elevational direction was relatively worse (~5.6 mm) due to the large extent (5 mm) of the transducer elements. Based on the performance, they were able to acquire high-quality 3D vasculature images from eight subjects (one healthy, seven cancerous). Among these, representative results acquired from two breast cancer patients with radiographically dense breasts are presented in Figure 12k.

Although the X-ray images (left-most ones) did not show any distinguishable image contrast, the PA images clearly visualized tumor regions. In addition, by applying the vessel density (local vessel number/local area) calculation algorithm they developed, they were able to further boost the image contrasts of the tumors (right-most ones). Moreover, they disclosed a new concept that differentiated tumor regions based on the compliance difference of tumor and normal tissues with respect to a mechanical deformation (such as a breathing motion as mentioned in the paper) by using the acquired PA images. In terms of the imaging depth, their system's performance was comparable with those of previous studies (Kruger et al. 2010, 2013) and reached ~4 cm.

In this section, several representative system configurations developed for breast imaging have been introduced. As shown, some of the earlier reported imaging systems suffered from either limited FOV or scanning speed, limited spatial resolution, and insufficient imaging depth. However, the two systems that were more recently reported (Lin et al. 2018; Toi et al. 2017) have sufficiently advanced to delineate numerous vascular details at much improved imaging speeds and depths. Consequently, they could successfully illustrate the core benefit of PAT for dense breast tissues for which conventional X-ray mammography does not work effectively.

Considering the speed with which related technology has progressed, we expect that PAT could attain its meaningful position in the near future since it can provide detailed vasculature associated with tumor development without the involvement of contrast agents and ionizing radiation. As angiogenesis is a well-known hallmark of cancer, PAT could be more useful than MRI in future breast cancer diagnosis and management, when considering such technical aspects, such as excellency in vasculature visualization, real-time imaging capability, better accessibility to the system with virtually no limitation to the frequency of use, and versatile compatibility with various contrast agents. Although clinically approved dedicated functional contrast agent is not available yet, we anticipate that it will be realized in the near future and thus greatly increase the utility of PAT in clinics.

To more successfully realize this goal, however, further improvement in imaging depth remains necessary. Moreover, in the case of the presented systems, equipping them with conventional US imaging function, which is technically possible, would be a desirable development. We imagine a future PAT system capable of whole

breast imaging based on a single shot of laser pulse and capable of providing co-registered US images in real time.

Dermatological Applications

Currently, the application of PAT for dermatological uses is not large as compared to the breast imaging application, as the former only emerged in earnest in the late 2000s. However, several papers reported in recent years have demonstrated its promise in terms of clinical success. Although Oraevsky et al. also mentioned the dermatological application of PAT in an earlier 1990s study (Oraevsky et al. 1994b), full-fledged research outcomes could only be reported after the AR-PAM concept was first introduced by Maslov et al. of the Wang group in 2005 (Fig. 13a) (Maslov et al. 2005). Before 2005, image quality of the PACT systems that were typically available at that time were not good enough to visualize detailed morphologies in the skin. However, due to the substantial resolution improvement provided by the AR-PAM technique, vascular details distributed in a cutaneous tissue could be very clearly visualized at an axial resolution of ~15 μm and a lateral resolution of ~45 μm (Maslov et al. 2005), which represents an approximately 10-fold improvement compared to previous PACT images.

After reporting on the AR-PAM concept, researchers in the Wang group first attempted to showcase its applicability to dermatology by imaging various skin diseases or conditions. For example, at approximately the same time in 2006, Zhang et al. (Zhang et al. 2006a) and Oh et al. (Oh et al. 2006) in the Wang group reported the first PA image feature of an inoculated B16 melanoma tumor, which is a representative murine cancer cell line frequently utilized for human skin cancer studies.

Fig. 13 Representative systems developed for the dermatological applications of PAT and produced images. (**a**) Photo of an AR-PAM system (Maslov et al. 2005). (**b**) The first AR-PAM-based sO_2 image was acquired from a subcutaneous section of rat skin in vivo (Zhang et al. 2006a). (**c**) In vivo AR-PAM image of a subcutaneously inoculated B16-melanoma in an immunocompromised nude mouse, acquired using 584 nm and 764 nm (Zhang et al. 2006a). (**d**) Photo of a nevus located on the forearm of a subject (Favazza et al. 2011). (**e**) Corresponding AR-PAM image (570 nm) delineating the nevus and surrounding blood vessels. (**f**) Schematic of the OR-PAM system developed for cuticle imaging (Hsu et al. 2016). (**g**) Photo showing the imaged area. (**h**) Wide-field PA image of cuticle capillaries depicted with normalized PA amplitude. (**i**) Selected time-lapse images of single-RBC sO_2. (**j**) Time-averaged images (~10 s) of all time-lapse frames of sO_2 imaging. (**k**) Photo of the portable UB-RSOM system (Aguirre et al. 2017). (**l**) Schematic depicting the operation of UB-RSOM. The transducer was raster-scanned parallel to the skin surface, acquiring the PA A-line signals generated by laser illumination (532 nm) from two fixed fiber bundles. Note that the focal point of the transducer was kept above the skin surface. (**m**, **n**) UB-RSOM images of psoriatic (**m**) and healthy (**n**) skin. The histology images were acquired based on hematoxylin and eosin staining to compare with the corresponding UB-RSOM cross-sections

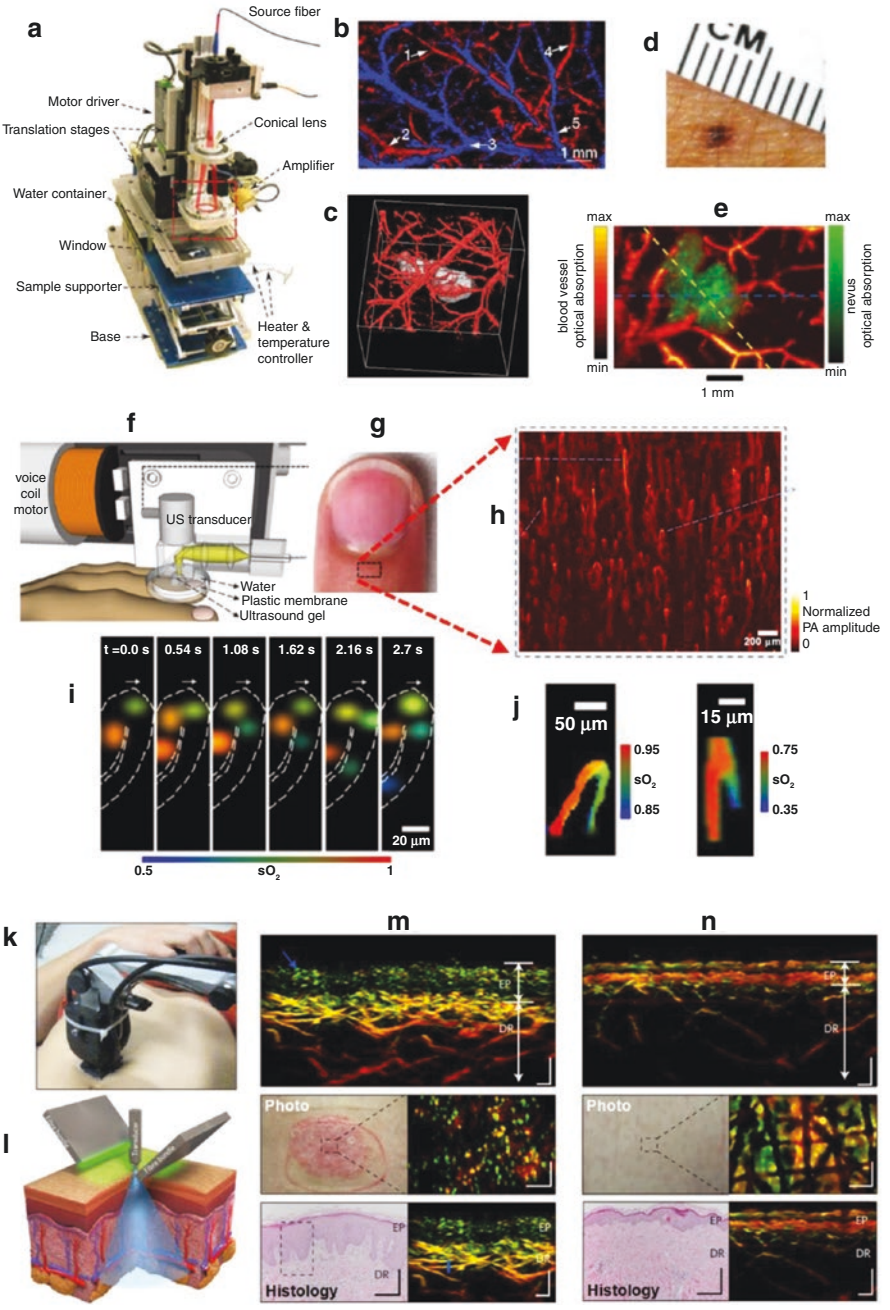
a
Source fiber
Motor driver
Translation stages
Conical lens
Amplifier
Water container
Window
Sample supporter
Base
Heater & temperature controller
b
1
2
3
4
5
1 mm
c
d
cm
e
max
min
blood vessel optical absorption
nevus optical absorption
1 mm
f
voice coil motor
US transducer
Water
Plastic membrane
Ultrasound gel
g
h
200 μm
1
Normalized PA amplitude
0
i
t =0.0 s
0.54 s
1.08 s
1.62 s
2.16 s
2.7 s
20 μm
0.5
sO2
1
j
50 μm
0.95
sO2
0.85
15 μm
0.75
sO2
0.35
k
l
m
n
EP
DR
Photo
Histology

In particular, the former paper (Zhang et al. 2006a) presented a sO_2 map of blood vessels distributed in rat skin (Fig. 13b), which is referred to as the first experimental demonstration of the functional (i.e., sO_2) imaging capability of PAM. Moreover, they also presented the first PAM image of human palmar vessels distributed at a ~ 3 mm depth. Although the melanoma tumor image presented in the paper (Fig. 13c) was not from an actual human subject, but from an animal (nude mouse), the range of demonstrations presented in the paper presented an important event announcing the beginning of the dermatological application of PAM. In the same year, Zhang et al. presented another report that demonstrated the technique's diagnostic potential in evaluating the depth of a thermal burn. For this, they artificially induced a thermal burn on porcine skin and imaged it ex vivo (Zhang et al. 2006b).

Approximately 5 years later in 2011, Favazza et al. of the Wang group presented a report that demonstrated more direct potential for the AR-PAM technique for in vivo dermatological applications by imaging a nevus developed in real human skin (Fig. 13d) (Favazza et al. 2011). Clinically, nevus is known as a benign tumor of melanocytes, which should be accurately differentiated from melanoma in order to avoid unnecessary biopsies. However, many pigmented lesions still display some of the clinical characteristics of melanoma, and their discrimination still relies heavily on clinical suspicion based on evaluation parameters such as asymmetry, border irregularity, color, size (lateral dimensions), and change (evolution, lesion growth). Thus, if a lesion raises sufficient concern, it is biopsied and histologically analyzed, and a definitive diagnosis is rendered.

To demonstrate related applicability, they imaged a volunteer with nevus, and effectively visualized the affected areas and surrounding microvasculature using a 570-nm laser excitation wavelength as shown in Figure 13e. In addition, by analyzing the depth-resolved PA images, they also demonstrated that the PAM system could accurately identify the thickness, depth, and volume of the lesion, all of which could be confirmed using a histological analysis performed on the excised tissue.

In addition to the nevus imaging experiment, they also performed a normal cutaneous imaging experiment, and they found an interesting result; namely, a large difference in the vascular patterns between the forearm and palm. Based on the demonstrated high-resolution vasculature imaging capability of PAM, they suggested that the PAM technique could serve as a new tool for characterizing and assessing cutaneous malignancies or other skin disorders, such as melanoma and hemangioma in situ, and also for diagnosing and assessing systemic diseases that affect the microvasculature, such as diabetes, renal disease, hypertension, and many other cardiovascular diseases.

Meanwhile, in 2008, the OR-PAM technique, which is another version of PAM that was invented to provide an optical-resolution PA image, was first introduced to the PAT field by Maslov et al. of the Wang group (Maslov et al. 2008). Although only relatively few researchers have investigated the dermatological application of the OR-PAM technique, it has immense potential as it possesses a unique functional imaging capability in terms of microcirculation. According to the literature, most OR-PAM-based research to date have focused on other research subjects, such as

brain or cancer imaging studies that are based on animal models rather than human subjects.

Of the several papers that demonstrated the dermatological application of OR-PAM, Hsu et al. of the Wang group in 2016 showcased more direct potential for dermatological application (Hsu et al. 2016). Using a fast voice-coil scanning-based OR-PAM system (Fig. 13f), which was an improved version from the original system presented in ref. (Wang et al. 2013) in terms of the dual-wavelength imaging capability, they investigated the vascular structures and other functional parameters (sO_2) of human cuticles for the first time in vivo (Fig. 13g). They chose the cuticle region because of its ability to present microcirculation well, and they imaged nine healthy subjects.

The cellular-level and high-resolution imaging capability of the system (3 μm lateral and 15 μm axial) made it possible for the detailed structures of the imaged capillary loops to be clearly visualized in the MAP image (Fig. 13h). Moreover, the high-speed imaging capability providing 100 B-scan frames enabled the tracing of a single RBC flow in a capillary loop along with the record of its sO_2 change in real time (Fig. 13i). Surprisingly, by averaging multiple sO_2 images acquired in such a manner for ~10 s (Fig. 13j), they discovered that more oxygen was released in the curved cuticle tip than in other regions of the capillary loop. Furthermore, they observed that the RBC flow speed decreased in the tip region. Based on further analysis, they concluded that in addition to the decreased RBC flow speed, other factors, such as the drop of the partial oxygen pressure in the tip region, drove RBCs to release more oxygen in the tip region.

As the cuticle region serves as a window representing the status of microcirculation, monitoring such functional parameters at the fundamental level of the physiology of oxygen transport can potentially help physicians define clinical standards for early-stage diagnosis and evaluation of perivascular diseases, such as Raynaud's phenomenon and systemic scleroderma, before capillaries undergo observable changes in morphology.

Meanwhile, in 2017, Aguirre et al. of the Ntziachristos group also reported a research outcome that was important enough to rekindle interest in this application area (Aguirre et al. 2017). By using a raster scan optoacoustic mesoscopy implemented in ultra-broadband (10–180 MHz) detection mode (UB-RSOM) (Fig. 13k and l), they visualized detailed vasculature of normal and psoriatic skins with a spatial resolution as high as 15 μm. However, it should be noted that such a high spatial resolution could be sustained up to a 2-mm depth, and it was not achieved by applying the OR-PAM concept, but by employing a custom-made focused ultrasonic transducer ($f = 3$ mm, NA: 0.5, $LiNbO_3$) with the ultra-broad detection bandwidth (170 MHz) and a laser system with an ultra-short pulse duration of 0.9 ns. Furthermore, to effectively utilize the detected broad frequency components, they applied a frequency band equalization technique that they developed, and they finally produced images by applying a dedicated image reconstruction algorithm that was based on a beam forming concept.

Figure 13m and n depicts the representative imaging results of psoriatic and healthy tissues, respectively. As shown in the three UB-RSOM images presented in

the left column, elongation and dilation of capillary loops (visualized in green), thickening of the epidermal layer due to prominent skin acanthosis, and increased vessel diameter and vascularization in the dermal layer were clearly observed compared to healthy skin (right column). Furthermore, the layered structure observed in the healthy skin disappears in psoriasis, and coronal UB-RSOM images close to the surface of the psoriatic skin were markedly different from the corresponding images of healthy skin. Observation of the histology images revealed that the overall features provided by the label-free UB-RSOM demonstrated good agreement with them.

Indeed, the presented results are remarkable achievements that demonstrate the potential of PAT for the crucial issue of dermatological application. However, apart from its dermatological implications, it must be noted here that although they produced high-quality images over a large volume of tissue (~4 × 2 × 1 mm^3) with a high spatial resolution (lateral/axial: 18.4/4.5 μm) that remained mostly consistent over the entire volume, the scanning time was merely ~70 s, which was a rather short scanning time compared to that required by large scanning points like 266 × 135 scanning points. This result could be explained by the synergetic effect of the employed ultra-broad band acoustic detection, frequency band equalization, and dedicated image reconstruction techniques, and it would have probably been impossible if the conventional OR-PAM scanning concept was applied.

Considering this aspect, we expect that the presented imaging concept could provide a more effective solution to making a seamless connection between OR- and AR-PAM techniques; that is, visualizing those structures lying around the boundary between ballistic and diffusion regimes without drastic change of the spatial resolution. Although several researchers have attempted to address the issue, unsatisfactory resolution zones remain because they constructed related systems by simply merging OR- and AR-PAM concepts.

Currently, only a relatively small number of studies have explored this domain of application. However, continuous attention to this area may be needed because interest in beauty and healthcare has steadily increased recently. In addition, it should be noted that after the paper, the Ntziachristos group also recently presented a report that applied artificial intelligence (AI) to skin vasculature analysis (Moustakidis et al. 2019).

Endoscopy or Minimally Invasive Imaging

Another important clinical application of PAT is minimally invasive imaging, and continuous research has been made in this area in recent years. As already demonstrated by many studies based on precedented endoscopic methods, such as endoscopic OCT (Tearney et al. 1997; Yun et al. 2006; Gora et al. 2013) and confocal endoscopy (Kiesslich et al. 2004, 2006, 2007), the optical approach is known to be superior to conventional endoscopic ultrasound (EUS) (Shami and Kahaleh 2010; Akahoshi and Bapaye 2012) in terms of disease specificity, and as an optical imaging modality, PAT-based minimally invasive imaging applications have also gained

validity based on their unique imaging capability that provides rich functional and molecular information at clinically relevant depths. The importance of related applications is evident from the recent increase in the number of related publications: Currently, it forms the second largest clinical application area after breast cancer application.

Reviewing the literature pertaining to this application area revealed several initial papers that were published in the 1990s and that addressed gastrointestinal (GI) tract (Oraevsky et al. 1997) or intravascular imaging applications (Chen et al. 1993; Beard et al. 1998). Thereafter, two more studies reported in 2001 and 2005 pursued the same applications (Viator et al. 2001; Henrichs et al. 2005). However, although these reports also recognized the importance of related research, earnest research activities arose in the latter part of the 2000s, as Sethuraman et al. of the Emelianov group reported the first PA image acquired from a rabbit aorta ex vivo in 2007 (Sethuraman et al. 2007). In the paper, not only did they present the aorta image, they also proposed a conceptual idea on the related imaging device to be embodied in an integrated PA and US imaging design. Indeed, it was an important event that reignited attention because it illustrated how the PA and US images differed and what synergetic effect could be derived through integrated dual-modality imaging, more details of which are presented in the next section titled "Intravascular photoacoustic imaging."

Unlike conventional EUS and endoscopic OCT probes, a miniaturized PA imaging probe requires the integration of optical and acoustical elements in a single imaging probe, which creates a challenge and thus slows down the technology's progress. Nevertheless, the minimally invasive imaging approach would ultimately represent one of the most important clinical application directions of PAT because the typical imaging depth of PAT is less than ~5 cm; however, there are many important clinical issues that can be sufficiently covered by this depth. Moreover, in clinics, there are already well-established US-based endoscopic tools, such as EUS, transesophageal echocardiography (TEE), intravascular ultrasound (IVUS), transrectal ultrasound (TRUS), and transvaginal ultrasonography, which can be potentially integrated with their PA counterparts.

Related to this fact, minimally invasive imaging application of PAT has been pursued for the three main endoscopic divisions: GI, intravascular, and urogenital imaging applications. Thus, in this section, we introduce major achievements related to these areas.

Gastrointestinal Tract Imaging

After categorizing documented reports according to their application areas, it was obvious that compared to the intravascular imaging application to be presented next, relatively fewer studies related to Gastrointestinal (GI) application have been reported. Nevertheless, GI application is a crucial endoscopic area because it forms the largest endoscopic clinical application, and there are also many important diseases, such as various GI cancers, where PAT can be effectively used. Although PAT has already demonstrated its potential for critical clinical issues, such as breast cancer detection and dermatological issues that develop near the body surface, most

other major diseases arise in internal organs, where PA imaging from outside the body may not be applicable.

Recognizing the importance of GI application, Yang et al. from the Wang group undertook related technology developed and reported their first achievement of a miniaturized imaging probe in 2009 (Yang et al. 2009). In the paper, they demonstrated a physical embodiment with a 4.2-mm diameter and ~ 4-cm long imaging probe by applying a micromotor-based built-in scanning mechanism, and they also showcased its endoscopic imaging capability by imaging excised tissues ex vivo. The key feature of the imaging probe was the use of a scanning mirror that was customized to reflect both the laser beam and acoustic waves during constant rotation (~4 Hz). Notably, by applying the scanning mirror concept, it was possible to transmit laser pulses and electric signals at the proximal unit via static cables. Compared to previous endoscopes (Oraevsky et al. 1997; Chen et al. 1993; Beard et al. 1998; Viator et al. 2001; Henrichs et al. 2005; Sethuraman et al. 2007), the main advancement of the probe lay in its embodiment as a fully encapsulated form, in which all necessary optical and acoustic detection mechanisms and scanning mechanisms were integrated, thus enabling the first endoscopic imaging.

After the 2009 report, the authors also successfully implemented the advanced version with a 3.8-mm diameter and demonstrated the first case of in vivo endoscopic imaging applicability, using rabbits and rats (Yang et al. 2012a). Figure 14a depicts the imaging probe and imaging concept presented in the paper. Compared to the previous study (Yang et al. 2009), they demonstrated a co-registered, simultaneous, dual-wavelength PA and US endoscopic imaging concept for the first time, and they also greatly improved the lateral resolution by employing a focused US transducer.

In addition to the technical advancement, the paper presented several notable endoscopic demonstrations that, for the first time among optical endoscopic techniques, detected PA signals even from major organs, such as the lung and trachea located around the esophagus, and also successfully mapped sO_2 for the two major blood vessels; that is, the aorta and caudal vena cava, which directly branched out from the heart of a rabbit (Fig. 14b). Moreover, by using Evans blue as a contrast

Fig. 14 PA endoscopes developed for GI tract imaging applications and produced images. (**a**) An illustration depicting the principle of simultaneous dual-wavelength PA and US endoscopic imaging (Yang et al. 2012a). (**b**, **c**) Representative images were acquired from a rabbit esophagus (b) and rat colorectum (**c**) **in vivo**. (**d**) Schematic and photo of the dual-modality PA and LUS endoscopic probe (Tsyboulski et al. 2014). (**e**) Conventional US (middle), PA, and LUS image of a tissue-mimicking phantom with embedded glass spheres. The PA and LUS images were acquired according to the presented concept. (**f**) Photos of the optical-resolution PA endomicroscopic probe and its optical illumination and acoustic detection unit (Yang et al. 2015). (**g**) Schematic of the optical illumination and acoustic detection unit, which corresponds to the lower photo in (**f**). The inserted photo represents the optical illumination unit comprising an optical fiber and GRIN lens. (**h**) Label-free **in vivo** optical-resolution PA endomicroscopy image acquired from a rat colorectum. (**i**) Schematic and photo showing the distal end of the 2.5-mm outer diameter catheter (torque coil)-based PA and US dual-mode endoscopic probe capable of full angular FOV imaging (Li et al. 2018b). (**j**) Corresponding 3D PA and US images acquired from a rat colorectum in vivo

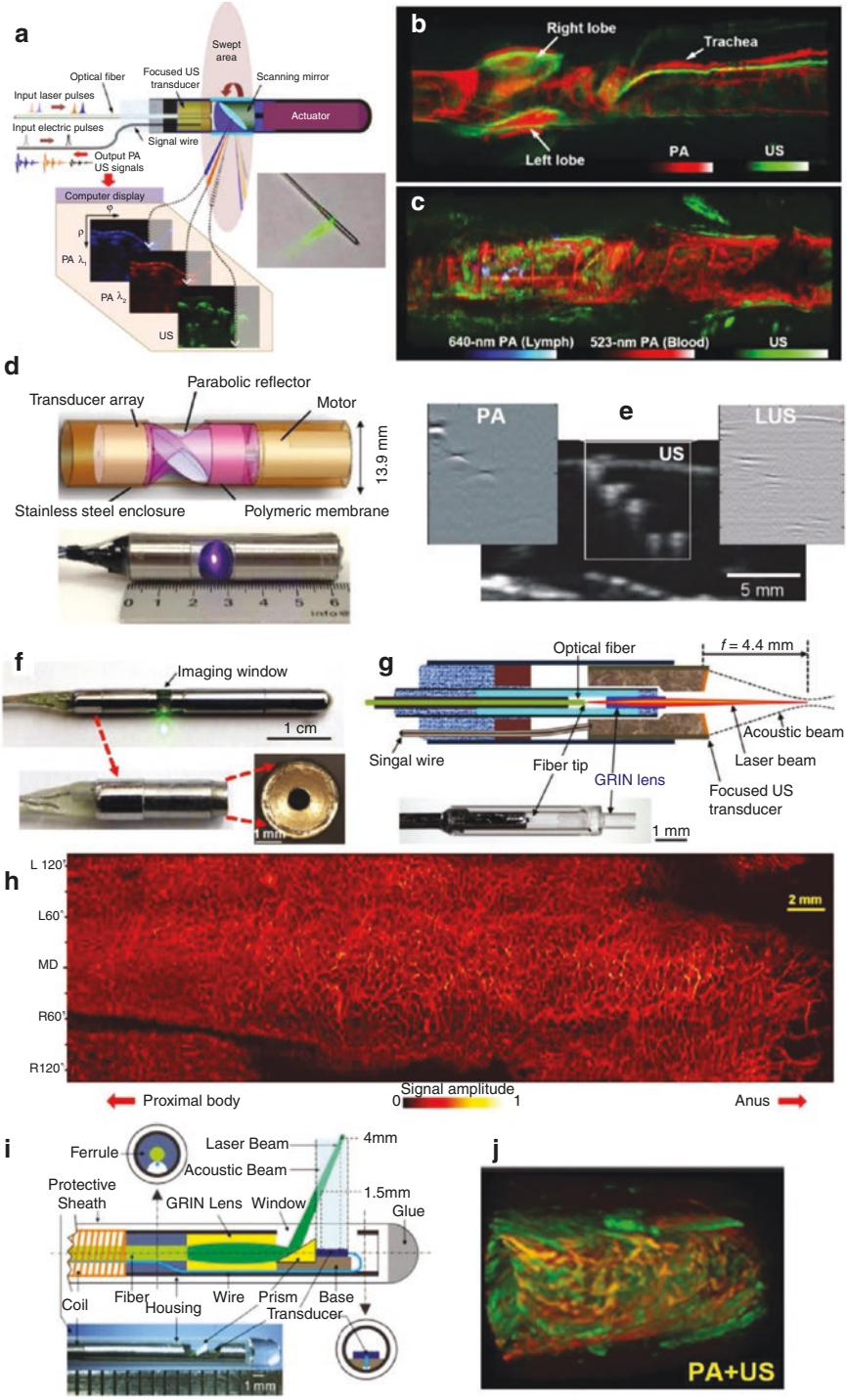
a
Swept area
Optical fiber
Focused US transducer
Scanning mirror
Input laser pulses
Actuator
Input electric pulses
Signal wire
Output PA US signals
Computer display
PA λ1
PA λ2
US
b
Right lobe
Trachea
Left lobe
PA
US
c
640-nm PA (Lymph)
523-nm PA (Blood)
US
d
Parabolic reflector
Transducer array
Motor
13.9 mm
Stainless steel enclosure
Polymeric membrane
e
PA
US
LUS
5 mm
f
Imaging window
1 cm
1 mm
g
Optical fiber
f = 4.4 mm
Acoustic beam
Singal wire
Fiber tip
GRIN lens
Laser beam
Focused US transducer
1 mm
h
L 120°
L60°
MD
R60°
R120°
2 mm
Proximal body
Signal amplitude
0
1
Anus
i
Ferrule
Laser Beam
4mm
Acoustic Beam
Protective Sheath
GRIN Lens
Window
1.5mm
Glue
Coil
Fiber
Housing
Wire
Prism
Base
Transducer
1 mm
j
PA+US

agent, they successfully visualized the lymph nodes and vessels distributed around the descending colon of a rat (Fig. 14c). Although the image demonstrations were performed in animals (i.e., rabbits and rats), it must be noted that they were all achieved using transesophageal or trans-enteric imaging, which suggests that PAE technology could be further developed to be utilized in a manner similar to current clinical TEE or EUS probes.

After the in vivo demonstration, the group reported two advanced versions of a PAE probe, a 2.5-mm diameter probe (Yang et al. 2012b) and a catheter-based PA endoscope (Yang et al. 2014), to be used for a clinical study that evaluated its utility for Barrett's esophagus diagnosis. Compared to the previous version (Yang et al. 2012a), the two probes featured a unique technical aspect: They were embodied in a narrower diameter or a fully flexible form to be used for real human GI tract imaging via the instrument channel of a clinical video endoscope. However, they turned out to be insufficient for use in the clinical study due to multiple technical issues, such as the long rigid distal section (Yang et al. 2012b) or the fragileness of the signal wire near the distal connection point (Yang et al. 2014).

While the Wang group developed the endoscopic probes, two notable endoscopes were also reported by other groups in 2010 (Yuan et al. 2010) and 2014 (Tsyboulski et al. 2014). Unlike those reported by the Wang group, in which a single-element US transducer was employed to develop the probes and which mostly aimed for a miniprobe, the two probes featured the use of an array transducer that served to develop them into a large probe.

The first was the 64-element array transducer (5 MHz)-based PAE probe reported by Yuan et al. in the Xing group in 2010 (Yuan et al. 2010), and it was developed for human colorectal cancer diagnosis. With this probe, they imaged an excised human colorectal tissue, including a tumor mass and claimed that their probe was capable of discriminating the tumor region with adequate contrast. However, although the overall device concept may have been feasible for practical clinical use, the large probe size (~3 cm in diameter and ~ 9.5 cm in length) needed to be further reduced. Furthermore, the fragile glass-based probe casing needed to be replaced with other materials.

The second probe was the 8-element array transducer-based PA and laser US endoscope developed by Tsyboulski et al. of the Oraevsky group in 2014 (Fig. 14d) (Tsyboulski et al. 2014). The probe was developed for esophageal and colon cancer diagnosis and harnessed the dual contrast benefit provided by PA and US imaging. However, interestingly, they applied a laser pulse-induced acoustic pulsing principle, namely "laser ultrasound (LUS)," instead of applying the conventional piezoelectric transducer-based acoustic pulsing method to perform US imaging. As per the concept, an LUS pulse is generated by a tubular polymeric membrane affixed around a rotating parabolic reflector in accordance with the same PA principle caused by some of the absorbed laser energy when a laser beam passes through the membrane. Of course, the membrane was acoustically transparent. Then, additional mechanical rotation was also provided to the parabolic mirror to achieve radial scan imaging. Compared to the previous probe (Yuan et al. 2010), there was a technical advancement in terms of the size (1.4 cm in diameter and 6 cm in length) (Tsyboulski et al. 2014). However, their image demonstration was limited to a proof-of-concept study based on nonbiological samples (Fig. 14e).

As shown, the two endoscopic probes were representative examples that were embodied as GI endoscopes employing an array transducer. However, their image demonstrations were all limited to ex vivo imaging, and no follow-up studies in relation to the probes were reported until now.

Meanwhile, in 2015, Yang et al. of the Wang group presented another report that demonstrated optical-resolution PA endomicroscopy in vivo for the first time (Yang et al. 2015). Figure 14f depicts the implemented imaging probe encapsulated in a stainless steel housing with a 3.8-mm outer diameter. As shown, its overall appearance and mechanical structure inherited those of the previous AR-PAE probe (Yang et al. 2012a). However, they achieved an OR-PAM level lateral resolution (~10 μm) by installing a 0.5-mm outer diameter gradient-index (GRIN) lens (0.20 pitch) inside the central hole of a ring-shape single-element focused US transducer (f = 4.4 mm, 42 MHz, $LiNbO_3$) and by guiding the necessary laser beam via a single-mode optical fiber (SMF) (Figs. 14f and g). The embodiment was key in attaining the best overlap between the optical focus and the acoustic focus to achieve maximum sensitivity, and the in vivo image presented in Figure 14h that was acquired from a rat colorectum shows that the alignment was successful.

The in vivo demonstration demonstrated that even a PAE probe with such a small diameter could provide a detailed vasculature map of a GI tract with a spatial resolution comparable to that of OR-PAM. However, for such a mini-PAE probe to be successfully translated into clinical usage, embodying related imaging probes in a fully flexible form over the entire probe section remains a key issue because it is typical that related imaging procedures are performed via the instrument channel of a standard clinical video endoscope. The paper reported by Li et al. of the Song group in 2018 eventually addressed the issue (Li et al. 2018b).

Unlike the previous built-in micromotor-based rotational scanning mechanism (Yang et al. 2009, 2012a, b, 2015), they applied the torque coil-based proximal actuation mechanism that is frequently utilized in conventional EUS mini-probes (Shami and Kahaleh 2010; Akahoshi and Bapaye 2012) or endoscopic OCT probes (Tearney et al. 1997; Yun et al. 2006; Gora et al. 2013). As already mentioned, the mechanism features include the use of a torque coil, which is commercially available and manufactured for the purpose of transmitting mechanical torque very smoothly from one end to the other, even in a bent condition. Furthermore, in such a torque coil, a hollow tubular hole is present, which enables a necessary signal wire and optical fiber for PA imaging to be placed inside. Consequently, leaving aside its great flexibility, applying this mechanism enabled related imaging probes to be embodied without limited angular FOV issues, which usually occur in the micromotor-based scanning mechanism (Yang et al. 2009, 2012a, b, 2015).

Based on these principles, the researchers implemented a 2.5-mm outer diameter catheter probe (Fig. 14i) that could potentially fit the 2.8-mm instrumental channel of a clinical video endoscope, and they demonstrated its in vivo applicability by imaging a rat colorectum (Fig. 14j). In the reported system, a slip ring-based optical–electrical rotary joint was also embodied at the connection point between the flexible catheter and the proximal driving unit. Furthermore, it can be seen that a GRIN lens unit was installed inside the scanning tip as in the case of ref. (Yang et al. 2015). However, it should be noted that the achieved lateral resolution was not as

great as that of ref. (Yang et al. 2015) because the employed optical fiber was not an SMF, but a multimode optical fiber (core dia.: 105 μm). Consequently, the attained PA transverse resolution was ~250 μm at the maximum SNR distance where the optical beam and the acoustic beam overlapped each other.

In short, the presented mechanism can be understood as an integration of an EUS and an OCT mini-probe, and it should also be noted that it has been the most frequently applied general mechanism in many intravascular PA imaging devices developed for cardiovascular applications, not only the GI applications. Related examples are introduced in the next intravascular imaging application section.

Previously, Yang et al. also adopted such a torque coil-based proximal actuation mechanism once in their catheter-based PAE probe (Yang et al. 2014). However, as the signal wire of an employed US transducer was not placed inside the torque coil but on a side of the plastic sheath, which was meant only to provide a static connection between the catheter and the proximal driving unit, the signal wire was easily damaged during its introduction into the instrument channel of a video endoscope. Eventually, such a design turned out to be undesirable. In this aspect, the configuration demonstrated in ref. (Li et al. 2018b) appeared to be more suitable for translation into practical clinical use. However, the unaddressed technical issue of related optical–electrical rotary joints being embodied based on a single-mode optical fiber remained. Although the related embodiment is not a simple issue due to the key requirement of delivering uniform optical energy during its rotation, it must be superior to the presented example in terms of the achievable spatial resolution.

All the PAE probes presented until now employed the conventional piezoelectric material-based US detection mechanism. Although this mechanism is more dominant, PA signals can also be detected by applying pure optics-based US detection mechanisms (Wissmeyer et al. 2018). Several mechanisms, such as FP polymer film (Beard et al. 1998; Zhang and Beard 2011; Ansari et al. 2018), micro-ring resonator (Hsieh et al. 2012), and a CCD camera-based US detection mechanism (Nuster et al. 2014), have been proposed so far. Among them, however, the first mechanism has been the most successful in terms of endoscopic applicability. Thus, in this section, we introduce a recent 2018 report by Ansari et al. (Ansari et al. 2018) from the Beard group as an example.

Figure 15a depicts their imaging probe that applied the FP polymer film-based US sensing mechanism and was developed for various laparoscopic approaches or interventional procedures, such as surgery, laser therapy, and needle biopsy. Since 1998, the group has pursued related technology development (Beard et al. 1998). However, in the presented paper (Ansari et al. 2018), they achieved high-resolution 3D PA imaging for the first time by implementing the optical sensor in a 2D array form. As shown in the schematic, the imaging probe was embodied as a forward viewing endoscope in which 50,000 optical fibers that acted as array elements were included and encapsulated in a 76-mm long rigid housing. Although the array consisted of such a vast number of detection elements, surprisingly, the achieved probe diameter was as small as 3.2 mm, a size that can numerically fit the standard instrument channel with a 3.7-mm diameter. Indeed, realizing such a high-density US array within such a small diameter was possible because they utilized the optical detection mechanism. This would have never been possible if the conventional

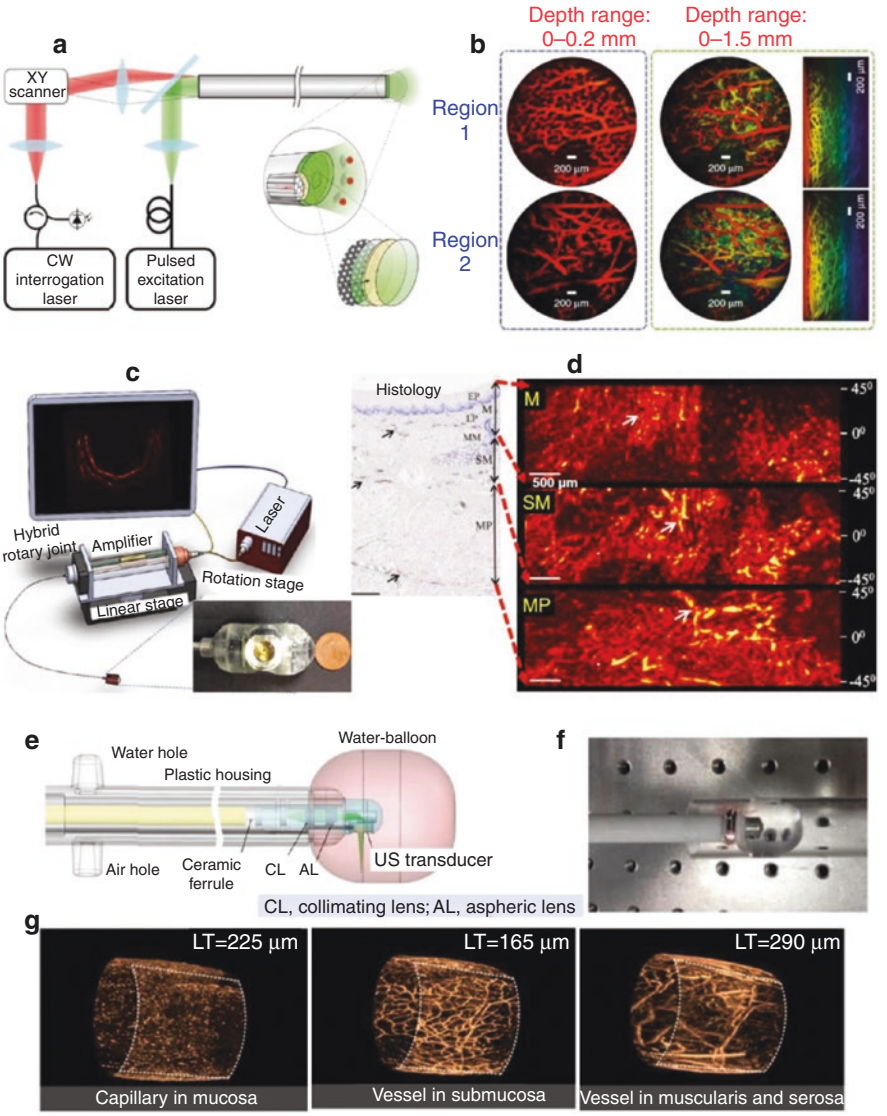

Fig. 15 PA endoscopes developed for GI tract imaging applications and produced images. (**a**, **b**) Schematic of an FP polymer US sensor-based forward viewing PA endoscopic probe (**a**) and corresponding 590-nm PA MAP images (**b**) acquired from an ex vivo duck embryo at two different regions (upper/lower rows) and depth ranges (left/right columns) (Ansari et al. 2018). The lateral and axial resolutions were ~ 45–70 μm and ~ 31 μm, respectively, for depths between 1 and 7 mm. (**c**) A schematic depicting the concept of the capsule-based PA endoscopic probe. The inset presents a picture of the implemented capsule (He et al. 2019). (**d**) A histology image (left) showing blood vessels at different esophageal layers revealed by anti-CD31 immunostaining, and radial-MAP images of the mucosa (M), submucosa (SM), and muscularis propria (MP) layers of the esophageal wall, respectively. (**e**) Schematic of the shape-adapting panoramic PA endomicroscopic probe (Xiong et al. 2019). (**f**) Photograph of the probe. (**g**) 3D PA images acquired from a rabbit colorectum in vivo. Each image depicts a vascular network in mucosa (left), submucosa (middle), and muscularis and serosa (right), respectively

piezoelectric method was applied. They validated its performance by imaging a duck embryo ex vivo (Fig. 15b).

The main shortcoming of this mechanism, however, is that it requires the installation of an additional complex optical system around the proximal part of the probe to interrogate the thickness changes of the FP polymer film attached at the other distal end, according to the pressure variation exerted onto the surface. In short, an interrogation beam should scan individual fibers one by one in order to address different points on the FP sensor film, a process that currently cannot be achieved quickly. In addition, it has the fundamental limitation of being incapable of conventional US pulse-echo imaging because it does not provide a reverse energy transduction mechanism. Nevertheless, attention should be paid to this technology because such an optical sensor exhibits the highest detection sensitivity and wide bandwidth characteristics ($f_{\text{-3dB}} = 34$ MHz).

Another notable technical issue that needs to be discussed relates to the target distance adjustment mechanism. This is particularly important when one designs an OR-PAE probe whose best resolution is only achieved at a specific distance called working distance.

As a representative example related to this issue, He et al. of the Ntziachristos group in 2019 reported an interesting endoscopic probe concept that could be applicable to a single-element transducer-based mechanical scanning mechanism (He et al. 2019). Although the aforementioned narrow diameter catheter has the advantage that it can be used via the standard instrument channel of a video endoscope, it is still true that if it is applied to imaging a human esophagus with a relatively larger diameter by directly contacting the esophageal wall, it can provide PA signals only from a limited angular portion where it contacts the wall. In clinical contexts, such a reduced effective angular FOV issue is undesirable because it greatly diminishes the detection possibility of cancerous tissues that may exist in other unscanned areas. Thus, to overcome the issue, the authors developed a tethered capsule-like optoacoustic endoscopic probe, namely capsule OE (i.e., COE), which can provide a full 360° angular FOV.

As shown in Figure 15c, it featured a capsule-shaped structure (18.6 mm in diameter and 20 mm in length) attached at the tip of a catheter. Its internal structure and components that were placed inside the catheter section were almost similar to those of the catheter-based probe (Fig. 14i), in which a 400-μm core diameter optical fiber was installed inside the conduit of the 3.2-mm diameter torque coil to deliver laser pulses. However, adding the capsule with a large diameter enabled them to employ a large diameter US transducer (30 MHz, PVDF), which performed a rotational scanning inside the capsule while receiving a mechanical torque from the torque coil. Consequently, the transducer, torque coil, optical fiber, and illumination optics placed around the transducer rotated together.

By attaching such a large diameter capsule, multiple benefits can be derived. These include the following: It gently expands an esophageal wall so that the wall surface is naturally positioned at an optimal working distance, where the lateral resolution is highest; no additional acoustic matching medium, excepting the body fluid, is necessary; and a room for installing a preamplifier, which is crucial for achieving a better SNR, can be secured very close to the transducer. Simply speaking, it provides an equivalent effect to using a medical balloon. Although the presented image

demonstration was limited to an ex vivo swine esophagus imaging (Fig. 15d), the presented concept could become practically useful due to the explained advantages.

In addition to this paper, another report addressed a technical issue related to acoustic coupling between a PAE probe and an imaged tissue. Although the presented capsule idea could also resolve this issue, it may impose a somewhat strong constraint on target tissues. However, in the 2018 report by Xiong et al. of the Yang group (Xiong et al. 2019), the issue was approached differently by integrating a water balloon to their rigid-type PAEM probe developed for colorectal cancer detection (Figs. 15e and f). Since the water balloon was very soft, it provided a gentler physical contact to target tissues by naturally changing its shape than that of the capsule-based method. In addition, it also enabled a boundary recognition to extract the holonomic vascular networks layer by layer, as shown in the rabbit colorectum image (Fig. 15g). As water balloons are frequently utilized in conventional EUS technology, the presented method could also be a key element in future clinical PAE. In relation to this, it could also be useful to refer to the adjustable focusing concept reported by Guo et al. in the Chen group (Guo et al. 2019).

In this section, we summarized PAE technology developments, focusing on several key papers that implemented a PAE probe with similar probe embodiment (i.e., mini probes or large diameter stand-alone probes) or typical technical features (i.e., single-element transducer- or array transducer-based probes) that are already applied in conventional EUS technology (Shami and Kahaleh 2010; Akahoshi and Bapaye 2012). Although the presented papers made their advancements close to the benchmarked EUS technology, only animal-based esophagus imaging or lower GI tract imaging has been reported so far, and no disease model-related or clinical study results have been reported yet (excepting the partially signals captured from a rectal wall as included in the human prostate image to be presented in a next section).

Intravascular Photoacoustic Imaging

The motivation for Intravascular photoacoustic (IVPA) imaging is to apply the excellent spectroscopic imaging capability of PAT for better screening and characterization of atherosclerotic plaques that build up in the cardiovascular system. In particular, vulnerable plaques that develop in the coronary artery are known to cause acute coronary artery syndromes, such as angina pectoris, sudden cardiac death, and myocardial infarction, all of which are major causes of death in many Western countries.

Presently, X-ray-based coronary angiography is regarded as the gold standard for examining stenosis, in which a radiocontrast agent is injected using the catheter introduced via the femoral or radial artery, and then its flow is displayed based on X-ray projection imaging. IVUS is also being increasingly used to delineate wall thickness and to determine calcification levels. In addition, a somewhat newly emerging technique called intravascular OCT has proven its clinical utility by providing unprecedented detailed anatomical image features, such as for vasa-vasorum (Yun et al. 2006), based on high-speed and high-resolution imaging capability. However, none of the mentioned imaging techniques can provide spectroscopic image information as rich as those by PAT. Consequently, more research efforts have been made in this area of application. Therefore, related research outcomes have also demonstrated an increase in recent years.

Although the idea of applying PAT for intravascular imaging was also suggested in earlier reports (Chen et al. 1993; Beard et al. 1998; Henrichs et al. 2005), earnest research activities relating to it emerged in the latter part of the 2000s; that is, after the Emelianov group reported the first PA and US image acquired from a rabbit aorta in 2007 (Sethuraman et al. 2007). The group paid their attention to structure and composition, rather than the degree of stenosis, which is a more important factor associated with acute clinical events, and thus PAT could be a valuable complement for better disease characterization and risk stratification.

Figure 16a and b shows the experimental setup and the first IVPA and IVUS images acquired from a normal rabbit aorta. As illustrated, the system was set up to provide co-registered PA and US images by incrementally rotating an excised aortic tissue sample, while a commercial IVUS catheter remained static inside the sample, and the necessary laser beam was delivered from the outside. Although the study did not address implementing a real intravascular imaging probe, it was the first one presenting how the IVPA image appeared and what kind of complementary image information could be provided over conventional single-mode IVUS images.

In 2008, the same group reported another notable demonstration using the same system (Sethuraman et al. 2008). As mentioned earlier, the key rationale for using PAT for this specific application was the excellent spectroscopic imaging capability that has the potential to discriminate plaque regions. To demonstrate feasibility, they imaged a normal and diseased atherosclerotic aorta, harvested from a rabbit subjected to 0.15% cholesterol chow for 10 months, using multiple laser wavelengths (from 680 to 900 nm), and they then spectroscopically differentiated plaque regions by applying a finite difference analysis method.

As shown in Figure 16c, the atherosclerotic (left) and normal (right) aorta images exhibited quite different slope patterns. Since the two images were processed from two PA images acquired at 680 nm and 900 nm, where lipid and collagen type I are known to manifest a large variation in the absorption, but with a different sign of the

Fig. 16 Systems and probes developed for IVPA imaging applications and produced images. (**a**) A commercial IVUS imaging catheter-based experimental setup for combined IVPA and IVUS imaging (Sethuraman et al. 2007). (**b**) IVUS (left) and IVPA (right) B-scan images acquired from a normal rabbit artery ex vivo. (**c**) The spectroscopic (first derivative) IVPA images of the atherosclerotic (left) and control (right) aorta calculated at 900 nm using a finite difference approach (Sethuraman et al. 2008). The reference image for evaluating the first derivative was obtained at 680 nm. In (**b**) and (**c**), the scale bars represent 1 mm. (**d**) Schematic (upper) and photo (lower) of the integrated IVUS and IVPA imaging catheter utilized for the first in vivo demonstration (Karpiouk et al. 2012). (**e**) First in vivo IVUS and IVPA images acquired from a rabbit's thoracic artery, at two different locations, in which a deployed stent was visualized. (**f**) Schematic showing the distal tip of the 1.25-mm diameter catheter probe and its peripheral systems (Jansen et al. 2011). (**g**) Histology and ex vivo IVPA and IVUS images acquired from a human coronary artery with an advanced atherosclerotic plaque. The histology (Oil Red O stain) reveals the presence of a lipid-rich plaque (*) as well as a calcified area (Ca). Lu, lumen; Pf, peri-adventitial fat. The two IVPA images were acquired using 1210 nm and 1230 nm, in which the lipid absorption was high and low, respectively. (**h**) Photo of the 1.1-mm diameter intravascular optical-resolution PA catheter probe showing its flexibility (Bai et al. 2014). (**i**) Schematic (upper) and photo (lower) of the distal end. (**j**) Schematic presenting the peripheral systems of the catheter probe. The 3D scanner consists of an optical–electric rotary joint (ROJ), a step motor, and a motorized pullback stage. (**k**) Three-dimensional cut-away PA image of a stent deployed in a plastic tube

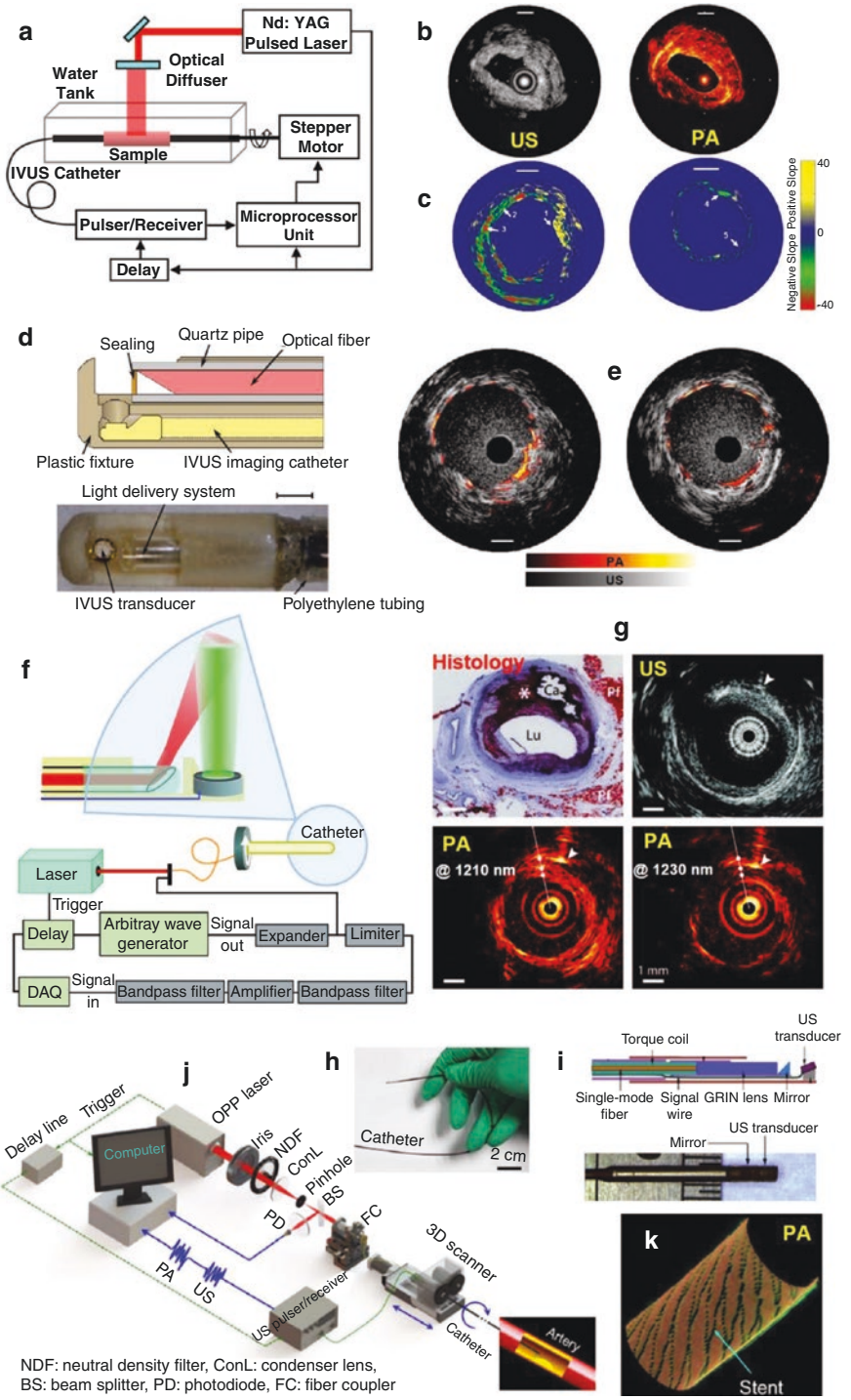

NDF: neutral density filter, ConL: condenser lens,
BS: beam splitter, PD: photodiode, FC: fiber coupler

slope, it can be seen that Region 1, in which a positive slope appeared, is suspected to be a lipid-rich region, while Region 3, which has a negative slope, is suspected to be a collagen type I-rich region.

In addition to the structural and spectroscopic imaging demonstrations, the group also reported the first IVPA-based molecular imaging result in 2009 (Wang et al. 2009). It is known that various biomarkers are present during the development of atherosclerotic lesions (Wang et al. 2010b). By using gold nanoparticles (Au NPs) as contrast agents, Bo Wang et al. from this group identified macrophages in atherosclerotic plaques (Wang et al. 2009). Macrophages are known to play a crucial role in the development and vulnerability of plaques. As such, Au NP has multiple advantages: small size on a nanometer level, good biocompatibility, and high volumetric absorption coefficient. Notably, when it is attached to other particles, it exhibits different optical absorption characteristics due to the surface plasmon resonance coupling effect.

As presented, the Emelianov group made most of the initial contributions demonstrating what kinds of actual benefits can be derived by the IVPA imaging technique if it were to be translated into clinical use. Although the demonstrations were promising, realizing a real imaging catheter remained a key issue. To address this, Karpiouk et al. from this group undertook related imaging device development, and they reported a prototype with a ~ 5-mm diameter in 2010 (Karpiouk et al. 2010). In their first outcome, the achieved probe diameter was somewhat large because they embodied it by simply adding a 600-μm core diameter, side-firing, and angle-polished optical fiber to the side of a commercial IVUS catheter (40 MHz, 3.6 F).

However, in 2012, the same team achieved an even narrower catheter with a 2.2-mm diameter (Fig. 16d) (Karpiouk et al. 2012), and they also successfully acquired the first in vivo IVPA (1064 nm) and IVUS images of a coronary stent deployed in a rabbit thoracic aorta (Fig. 16e). In the experiment, the imaging speed was very slow (~0.1 Hz) due to the PRR of the employed system. However, the study presented a valuable technical baseline—that such PA images could be acquired even in the presence of luminal blood using a laser pulse energy of 2.5 mJ.

Multiple research outcomes were also reported from other groups since 2010. In 2011, Jansen et al. in the van Soest group reported an even smaller diameter probe of 1.25 mm (Fig. 16f) along with the first ex vivo PA images of the investigated atherosclerotic human coronary artery samples that ranged between 715 nm and 1800 nm (Jansen et al. 2011). In their study, they demonstrated experimentally for the first time that an adequate level of image contrast for lipids could be created near 1210 nm, where a prominent harmonic of the C─H stretch vibrational mode signaled the presence of lipids (Fig. 16g).

A similar result was also reported by Allen et al. of the Beard group in 2012 (Allen et al. 2012). They investigated the spectral behavior of PA contrasts for atherosclerotic human aorta samples that ranged from 740 nm to 1400 nm, thereby reconfirming the contrast prominence of approximately 1210 nm. In addition, they performed a similar under-blood imaging test and discovered that a plaque region could still be visualized and differentiated, even through a 2.8-mm thick blood medium by using tens of mJ of laser pulse energy, which, however, was broadly

expanded over the sample (exact fluence was unspecified). The under-blood imaging test result increases the chance of actual clinic translation for the IVPA technique.

After related technical bases were established as described above, multiple groups began focusing on developing an applicable IVPA catheter for actual coronary artery imaging and reported related results. In 2014, Bai et al. in the Song group reported a 1.1-mm diameter probe (Fig. 16h) (Bai et al. 2014), whose size included its tubing thickness, implying that the IVPA technique could now achieve a typical thickness level comparable with those of existing clinical IVUS probes. Furthermore, the report presented two notable achievements: The device was embodied based on an OR-PAM concept, which thereby achieved a lateral resolution of 19.6 μm (Fig. 16i), and a slip-ring-based electrical and optical rotary junction at the proximal unit was demonstrated for the first time (Fig. 16j). It should be noted that the mechanism is commonly applied in most IVPA imaging systems reported thereafter. As the rotary joint was a key element that enabled a continuous rotational scanning unlike previous systems (Karpiouk et al. 2010, 2012; Jansen et al. 2011), they could acquire the first volumetric image from a stent as shown in Figure 16k.

In the next year, the same group also reported an even smaller probe at a diameter of 0.9 mm (Li et al. 2015); however, a quasi-focusing concept rather than an optical focusing concept was applied. Moreover, in the paper, they demonstrated a considerable advancement in the A-line acquisition rate, as high as 1 kHz; this was possible due to the effect of a rotary joint use and not merely the performance of the employed laser system. Although the two size achievements were technically considerable, the image demonstrations of the two papers were all limited to ex vivo experiments, presumably due to the still insufficient imaging speed.

To successfully translate the IVPA technique into clinical use, achieving a real-time imaging speed is also crucial because it is desirable to perform related imaging procedures within a few cardiac cycles. However, the imaging speeds of previous studies were all limited by either the low PRR or the availability of required wavelength from a commercial laser system. In general, the IVPA technique requires a laser wavelength of 1.2 or 1.7 μm, where the optical absorption of lipid generates strong PA signals. Unfortunately, however, existing commercial OPO systems do not provide a sufficient energy and pulse repetition rate at these two wavelengths. Recognizing this issue, the Cheng group has been reporting related achievements since 2014 (Wang et al. 2014b; Hui et al. 2015, 2017; Cao et al. 2016; Cao et al. 2018), presenting new types of catheter designs.

First, in 2014, Wang et al. of the Cheng group reported a custom-built barium nitrite [$Ba(NO_3)_2$] Raman laser system capable of providing a 1197-nm laser beam with a pulse energy as high as 2 mJ at a 2-kHz PRR, along with an integrated IVPA and IVUS catheter with a 2.9-mm outer diameter (Wang et al. 2014b). Although the probe diameter was relatively larger than those of previous reports, mainly due to the use of a large diameter ring transducer, embodiment levels for other parts were similar to them, and most notably, they demonstrated an A-line acquisition rate that was twice as fast as ref. (Li et al. 2015). Afterward in 2015, the group presented another report related to laser source development (Hui et al. 2015) that featured a potassium titanyl phosphate (KTP)-based OPO with an output pulse energy of up to

2 mJ at a PRR of 500 Hz and a wavelength of 1724 nm. The high energy achievement at this wavelength should be particularly noted because it was very close to the 1730-nm wavelength where the first overtone excitation of the methylene group CH_2 could be applied. For this reason, the 1730-nm wavelength has also been utilized in many later IVPA imaging studies.

In addition, in a 2016 paper reported and led by Cao et al., the Cheng group presented a new probe design that applied a collinear alignment concept between optical illumination and acoustic detection (Cao et al. 2016). In all previous studies that adopted a misaligned configuration between the optical illumination and acoustic detection (Karpiouk et al. 2010, 2012; Jansen et al. 2011; Bai et al. 2014; Li et al. 2015; Wang et al. 2014b; Hui et al. 2015), a significant signal drop occurred when an object location was beyond the overlapped position. However, in the new study (Cao et al. 2016), they solved this issue by configuring the illumination optics and acoustic sensor as depicted in Figure 17a. In fact, the probe concept was applied to the experiment reported in 2017 in which a 16-Hz B-scan imaging speed was demonstrated for the first time along with the use of an improved KTP-based OPO laser providing a 2-kHz PRR (Hui et al. 2017).

Would it be eventually possible to image an actual human coronary artery in vivo using such an IVPA technique? This may be the most important question when the related technology is pursued. In 2017, the van Soest group presented results showing the feasibility of this concept (Wu et al. 2017).

In the paper (Wu et al. 2017), Wu et al. acquired the first in vivo coronary artery images from a pig using their 1.3-mm diameter catheter probe composed of a 100-μm core diameter, angle-polished multimode optical fiber installed in a torque coil and a 40-MHz US transducer (Fig. 17b). Notably, the size included a sheath made of polyethylene (PE). As shown in Figure 17c, the imaging probe and all necessary peripheral systems were set up in a portable trolley to enable combined IVPA and IVUS imaging in real time in the experimental room. With the system, they could

Fig. 17 Systems and probes developed for IVPA imaging applications and produced images. (**a**) Schematic (upper) and photo (lower) of the 1.6-mm outer diameter IVPA and IVUS catheter with a collinear overlap between optical and acoustic waves (Cao et al. 2016). (**b**) Schematic (left) and photo (right) of the integrated IVPA and IVUS imaging catheter with a 1.3-mm outer diameter, whose measure included a polyethylene (PE) sheath. (**c**) A photo depicting the peripheral systems placed in a portable trolley for easy transportation (Wu et al. 2017). (**d**) An X-ray image showing the catheter and the two deployed stents (marked by two yellow boxes) with lipid target mounted on a balloon catheter. Note that the artificially created lipid target was located between the two stents. (**e**) Representative combined IVPA and IVUS B-scan image. The yellow-dashed area represents the artificially created lipid target. (**f**) Photograph of the 1.6-mm outer diameter IVPA and IVUS catheter with a quasi-collinear overlap between optical and acoustic waves (Cao et al. 2018). Note that the diameter measure included a polymer sheath. (**g**) A schematic illustrating the IVPA and IVUS imaging as well as the pullback C-scan. (**h**) A photograph exemplifying a related proximal actuation unit in which the optical rotary joint, electric slip ring, and mechanical pullback stage were included (this photograph was adopted from a different report (ref. Hui et al. 2017) presented by the same group). (**i**) Reconstructed 3D PA and US images acquired from a rabbit aorta over a pullback length of 20 mm. The image data were acquired at 4 fps and a pullback speed of 0.25 mm/s

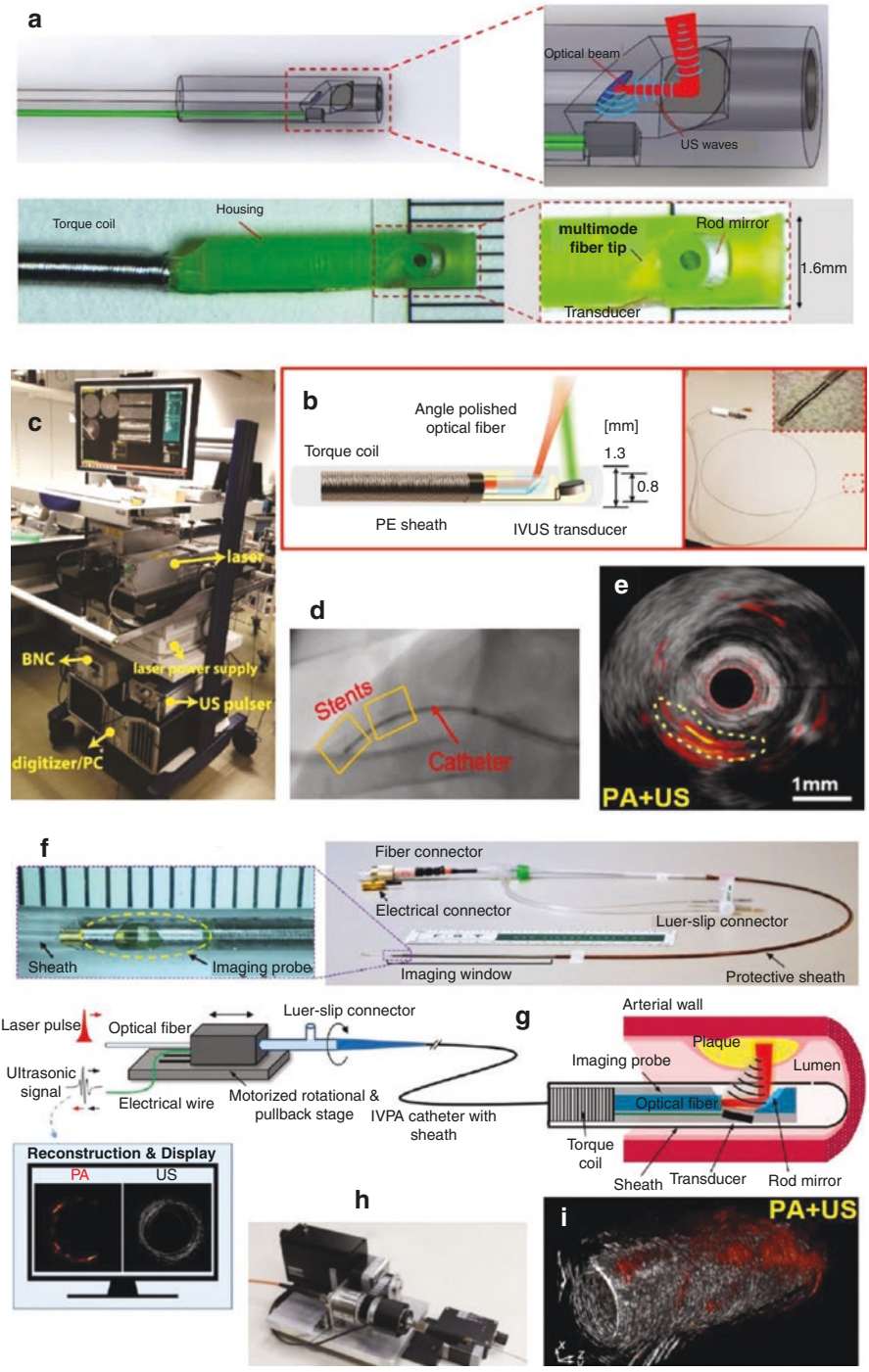
a
Optical beam
US waves
Torque coil
Housing
multimode fiber tip
Rod mirror
1.6mm
Transducer
b
Angle polished optical fiber
[mm]
Torque coil
1.3
0.8
PE sheath
IVUS transducer
c
laser
BNC
laser power supply
US pulser
digitizer/PC
d
Stents
Catheter
e
PA+US
1mm
f
Sheath
Imaging probe
Fiber connector
Electrical connector
Luer-slip connector
Imaging window
Protective sheath
Laser pulse
Optical fiber
Luer-slip connector
Ultrasonic signal
Electrical wire
Motorized rotational & pullback stage
IVPA catheter with sheath
Reconstruction & Display
PA
US
g
Arterial wall
Plaque
Imaging probe
Lumen
Optical fiber
Torque coil
Sheath
Transducer
Rod mirror
h
i
PA+US

successfully approach the right coronary artery (Fig. 17d) via the carotid artery with the aid of a guiding catheter (6 F), and they finally acquired high contrast PA images (Fig. 17e) from a lipid region that was artificially created to mimic a plaque lesion: The lipid was introduced into the imaged area prior to the imaging procedure. In the experiment, a 1720-nm laser wavelength with a pulse energy less than 80 μJ was utilized, and the frame rate of the B-scan, which was composed of 250 A-lines, was 20 Hz. During the imaging procedure, the artery was continuously flushed using heavy water-based saline.

A similar in vivo demonstration was also reported by Cao et al. of the Cheng group in 2018 (Cao et al. 2018), whose imaging result was, however, based on a rabbit model and performed using a 1.6-mm diameter catheter capable of achieving 16 Hz B-scan imaging speed (Fig. 17f). Figure 17g and h is the schematic of the implemented system and a photo of the rotary junction, respectively. In the in vivo imaging demonstration, they utilized a slightly different laser wavelength (1730 nm) with a pulse energy of 100 μJ at the output, and imaged a thoracic aorta region (Fig. 17i) after introducing the probe via the femoral artery. The imaged area might be understood as being less challenging compared to the coronary artery imaging demonstrated by the van Soest group (Wu et al. 2017). However, it should be noted that it was performed without flushing the blood.

Indeed, the presented in vivo IVPA imaging demonstrations along with the 3D pullback imaging were remarkable achievements that photoacoustically mimicked the current IVUS imaging procedure frequently performed clinically. From a technical perspective, it was possible because the torque coil and scanning tip of the two probes were all adequately sheathed in polymer tubing, unlike earlier probes (Karpiouk et al. 2010, 2012; Jansen et al. 2011; Bai et al. 2014; Li et al. 2015; Wang et al. 2014b; Cao et al. 2016; Hui et al. 2015, 2017). Needless to say, the sheathing is essential to protect the fragile coronary artery during the fast rotation of mechanical components; however, the sheathing also acts as an obstacle that deteriorates both optical and acoustic energy transmission. As such, the demonstrations (Cao et al. 2018; Wu et al. 2017) proved that an adequate SNR could be achieved even with the involvement of a sheath.

Although the demonstrations were promising, an unaddressed technical issue remained. Unlike ref. (Bai et al. 2014), the two demonstrations were not based on the use of a SMF and thus did not achieve optical focusing, which eventually resulted in a relatively poorer spatial resolution production than that of ref. (Bai et al. 2014). Although the spatial resolution may not be a critical part of IVPA application, applying such an optical focusing along with the use of a SMF or narrower diameter optical fiber would greatly improve the spatial resolution as well as SNR, even when using lower pulse energy.

As presented, real in vivo demonstrations of integrated IVPA and IVUS imaging were presented only in recent years, although the first concept was proposed in 2007, a decade earlier. This demonstrates the challenge posed by the development of this technology. Although some other technical issues related to the diameter, flexibility, and SNR still exist, we expect that the IVPA technique will be ultimately translated into clinical use because no fundamental limitation of the principle exists

(van Soest et al. 2017; Sowers and Emelianov 2018). In relation to the intravascular multi-modality imaging, it should also be considered to realize a tri-modality imaging of PA, US, and OCT. In 2011, related development targeting ovarian cancer diagnosis was addressed for the first time (Yang et al. 2011). However, the demonstration was limited to ex vivo imaging only because the required mechanical scanning mechanism was not effectively embodied. If the concept were to be realized in the form of an intravascular imaging catheter, there could be much great synergetic effect because each imaging modality possesses different strengths. So far, integration of only two imaging modalities (i.e., PA and US or OCT and US) has been demonstrated due to this challenge (Li et al. 2020).

Urogenital Imaging

Another crucial minimally invasive imaging application of PAT is the imaging of urogenital systems; thus far, prostate cancer (Kothapalli et al. 2019; Yaseen et al. 2010; Wang et al. 2010a; Bell et al. 2016; Horiguchi et al. 2016; Horiguchi et al. 2017) and numerous gynecologic cancers, such as endometrial (Miranda et al. 2018; Li et al. 2014), cervical (Qu et al. 2018), and ovarian (Yang et al. 2011; Kumavor et al. 2013) cancers, have been the major targets of application for capitalizing PAT as a new tool for the screening of these diseases as well as for guiding other procedures in relation to disease management. Among them, the prostate imaging application has been the most representative subject with the longest history of investigation because the organ can be relatively easily accessed via anal introduction. Currently, TRUS, which is also performed based on the same procedure, is regarded as one of the most representative tools for the diagnosis and management of prostate cancer. However, its clinical usage is mostly limited to biopsy guidance due to insufficient contrast. Oraevsky et al. recognized the importance of developing TRUS-like PAT probes and have been investigating this since the inception of PAT in addition to the application of PAT for breast imaging.

As a result of their efforts, in 2010, Yaseen et al. of the Oraevsky group presented a laser OA imaging system developed for prostates (LOIS-P), with an in vivo canine prostate imaging experiment that was designed to demonstrate efficacy for image-guided biopsy (Yaseen et al. 2010). In the system, a commercial 128-channel TRUS probe (Fig. 18a) was equipped with their OA imaging platform, including a signal amplification and DAQ function previously developed for the breast application (Ermilov et al. 2009). For the in vivo demonstration, they artificially created a bloody lesion, which simulated a cancerous tumor with high blood content, by surgically exposing the prostate of a dog and inserting an abrasive brush into the prostate via a 17G hypodermic needle (Fig. 18b). The exposed prostate was then placed on the colon and photoacoustically imaged using a 757-nm laser beam that approached the acoustic detection plane from an orthogonal direction. As shown in Figure 18c, in which two OA images acquired before (upper) and after (lower) the lesion induction are presented, only the OA image could successfully visualize the induced lesion, whereas the US image (Fig. 18d) did not show any change. Although the study demonstrated the feasibility of PAT-based prostate imaging, the developed

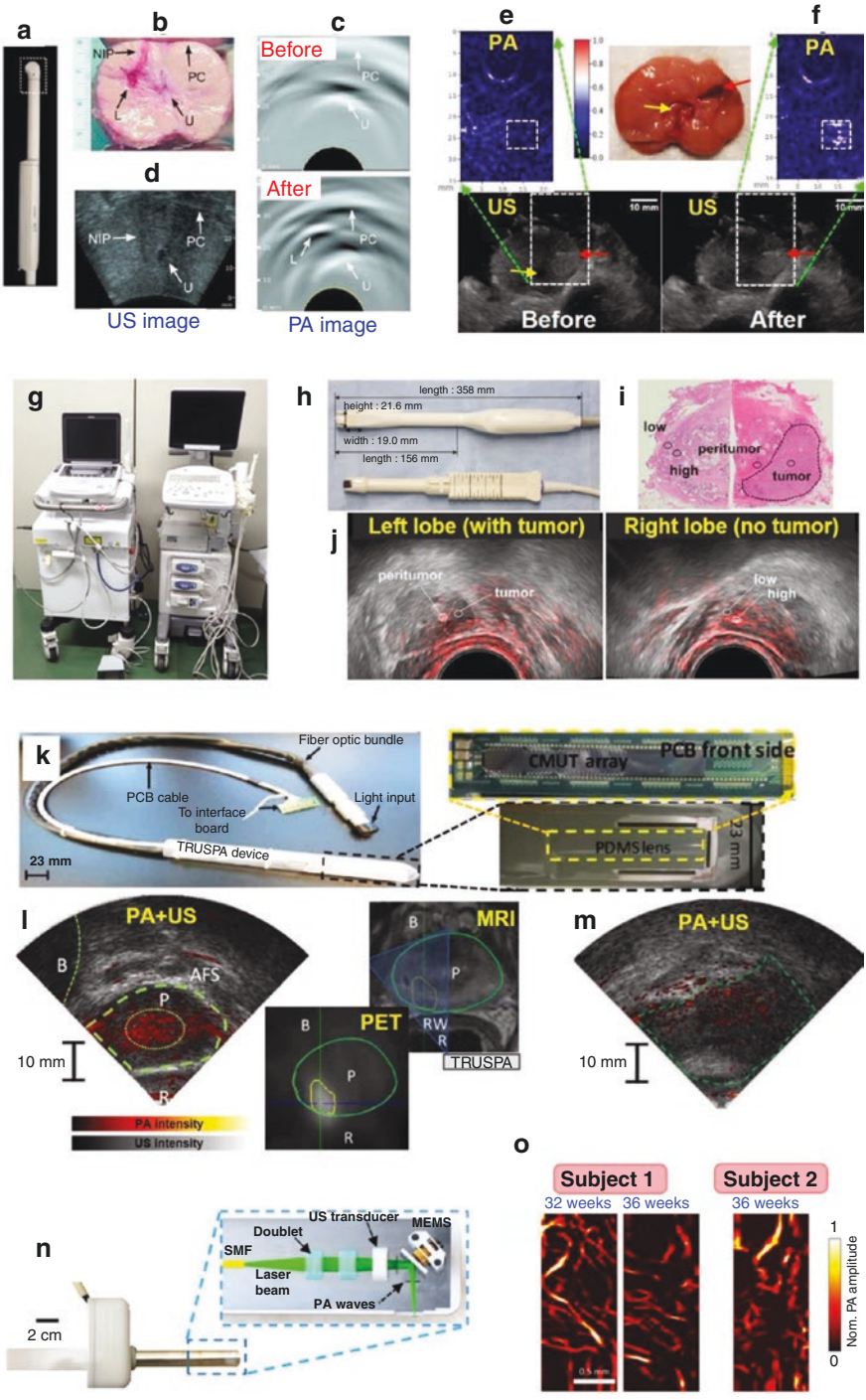
a
b
NIP
PC
L
U
c
Before
PC
U
d
NIP
PC
U
US image
After
PC
L
U
PA image
e
PA
US
10 mm
Before
f
PA
US
10 mm
After
g
h
length : 358 mm
height : 21.6 mm
width : 19.0 mm
length : 156 mm
i
low
peritumor
high
tumor
j
Left lobe (with tumor)
peritumor
tumor
Right lobe (no tumor)
low
high
k
Fiber optic bundle
PCB cable
To interface board
Light input
TRUSPA device
23 mm
CMUT array
PCB front side
PDMS lens
23 mm
l
PA+US
B
AFS
P
R
10 mm
PA Intensity
US Intensity
MRI
B
P
PET
B
RW
R
P
R
TRUSPA
m
PA+US
10 mm
n
2 cm
US transducer
MEMS
Doublet
SMF
Laser beam
PA waves
o
Subject 1
32 weeks
36 weeks
Subject 2
36 weeks
1
Nom. PA amplitude
0

Fig. 18 Representative outcomes reported in relation to the PAT-based urogenital tract imaging applications. (**a**) Commercial 128-channel endocavity US probe utilized for the dog prostate imaging experiment (Yaseen et al. 2010). (**b**) Photo of the sliced dog prostate, in which the needle insertion path (NIP), induced lesion (L) with blood, prostate capsule (PC), and urethra (U) are marked by an arrow. (**c**) PA images were acquired in vivo from the same dog prostate before (upper) and after (lower) the lesion was induced. The induced bloody lesion (L) is only visible in the lower image. (**d**) An US in vivo image acquired from the same dog prostate after surgery using a conventional US imaging system. (**e**, **f**) In vivo PA (upper) and US (lower) dual-modality mages of a canine prostate acquired before (**e**) and after (**f**) the generation of a lesion by injecting 0.1 ml of blood (Wang et al. 2010a). The photograph in the center represents the imaged prostate. In all images, red arrows indicate the plastic cannula inserted into the prostate for the blood injection, and yellow arrows indicate the urethra. Note that, although the PA and US images were co-registered, the presented PA images only correspond to the dashed rectangles in the US images. (**g**) Photo of the PAT system (left) developed for the human prostate imaging study and a conventional US imaging system (right); the two machines were presented together for an appearance comparison (Horiguchi et al. 2017). (**h**) Photograph of the developed TRUS-type PA probe (upper) and conventional TRUS probe (lower). (**i**) Histopathology image of the whole-mount specimen acquired from a subject. (**j**) Combined PA (red color map) and US (gray color map) image of the index tumors (left panel) and normal prostatic tissues (right panel) acquired from the subject. (**k**) Photograph of the 23-mm diameter TRUSPA imaging probe (Kothapalli et al. 2019). (**l**) Combined PA (red color map) and US (gray color map) in vivo image of the prostate in a patient with prostate cancer. In this image, the yellow contour indicates the suspicious region with a distinct PA contrast. The next two rectangular panels depict PET and MRI images acquired ahead of the TRUSPA imaging and utilized as references for the TRUSPA imaging. The blue-shaded triangular region in the MRI image roughly corresponds to the TRUSPA image. R: rectum, RW: rectal wall, B: bladder, AFS: anterior fibromuscular stroma, and P: prostate (green contour) (**m**) 2-min post-ICG TRUSPA image showing an enhanced PA contrast (red color map). (**n**) Photo and schematic of the transvaginal fast-scanning optical-resolution PAE probe (Qu et al. 2018). The probe features a custom-designed MEMS scanning mirror that permits a fast B-scan imaging speed of 250 Hz and has an encasing tube that is 20 cm in length and 20 mm in diameter. (**o**) Corresponding in vivo images (532 nm) acquired from the first pregnant woman at 32 and 36 weeks of gestation and the second pregnant woman at 36 weeks of gestation

system did not possess a combined US imaging function. It should be noted that the presented US image (Fig. 18d) was acquired using another commercial US system.

However, in the same year (2010), Wang et al. reported a more advanced imaging system that addressed this technical issue (Wang et al. 2010a). By modifying a commercial US system combined with a P4–1 phased array probe (128 chs), they successfully implemented a PA imaging function so that co-registered PA and US images could be provided by the single system. However, for this system, the necessary illumination optics remained unintegrated into the imaging probe, as with the previous system (Yaseen et al. 2010), and it also presented a limitation to producing these images by alternatively switching the related units on an off. However, there was a great improvement in the resolution, and also the contrast features in the PA and US images could be better differentiated due to the realized image co-registration capability. As with ref. (Yaseen et al. 2010), they also performed a similar invasive canine prostate imaging experiment (Fig. 18e) and demonstrated that the lesion artificially induced by the injection of small amounts of blood (as low as 0.025 ml) was detected only by PA imaging (Fig. 18f).

Although the latter study achieved dual-mode PA and US imaging successfully, the imaging probe was still unintegrated with a necessary illumination optic for PA imaging. However, in the paper reported by Bell et al. of the Zemp group in 2016, they addressed the issue by presenting a notable probe design (Bell et al. 2016). Unlike the previous two cases (Yaseen et al. 2010; Wang et al. 2010a), they implemented a custom-designed transrectal imaging probe by integrating a conventional 192-element linear array transducer and multiple optical fibers, which were distributed around the array transducer facing the scanning direction of the transducer to perform side-scanning. It should be noted here that the probe embodiment was not based on such a simple addition of illumination optics to an existing clinical US probe as in the next case. Although the image demonstration was limited to in vivo human skin imaging, they achieved a 10-Hz frame rate, even with the vast number of detection channels.

In 2016, as these three PAT groups conducted the delineated developments, Horiguchi et al. suddenly appeared in the field reporting two radical advancements that involved the first pilot clinical study results acquired from real human subjects with prostate cancer (Horiguchi et al. 2016; Horiguchi et al. 2017).

First, in the paper published in 2016 (Horiguchi et al. 2016), they reported the results of investigating whether PAT could help visualize periprostatic neurovascular bundles (NVBs) based on microvessels, which are known to be closely co-localized with NVBs and thus expected to reveal their presence in the form of PA signals. They raised the question because in urology there has been a crucial need to preserve NVBs around the prostate to preserve sexual potency after a radical prostatectomy (RP). First, to perform the study, they developed an integrated PA and US imaging system as well as two types of imaging probes, a conventional linear array-type US probe and a TRUS-type probe, which could be connected to the console. Then, they enrolled seven patients who were undergoing non-nerve-sparing retropubic RP, as they already had clinically proven organ-confined prostate cancer, and performed an in situ prostate imaging intraoperatively (using the TRUS-type imaging probe) as well as an ex vivo imaging with the resected specimens (using the linear array-type US probe).

Through the in vivo imaging experiments performed intraoperatively using 756 nm, they found that PAT was capable of locating NVBs using microvessels as the landmark of the NVBs and that it was also better at identifying NVBs than US alone. Importantly, the derived conclusion could also be identified and validated by experiments performed ex vivo, using the resected non-nerve-sparing RP specimens. As with the intraoperative imaging experiments, strong PAI signals were observed on the posterior and posterolateral surface of the prostate in most patients, and the location of the strong PAI signals was consistent with the location of coexisting microvessels and nerve fibers that could be identified by the immunohistochemistry analysis of the sample treated through double immunostaining with CD31 (for microvessels) and S-100 (for nerves). Furthermore, the location and extent of NVBs were more clearly visible in PAI images than in images by US alone.

The serial experiments were an important demonstration that suggested that PAT could be helpful in nerve-sparing radical prostatectomy. Thus, based on this

experience, they proceeded to a subsequent 2017 study (Horiguchi et al. 2017) that investigated whether the developed PAT system could describe the map of microvessels that arose from angiogenesis in prostate cancer and thus whether it could be utilized for detecting prostate cancer based on angiogenesis.

For the study, they recruited three patients who had undergone prostate biopsy and subsequent RP, and they acquired combined PA and US images just before the procedures by using the imaging system and probe (Fig. 18g and h), which was improved from the previous version (Horiguchi et al. 2016). Then, they retrospectively reviewed the acquired PA images and compared the most relevant PA images with the CD34-immunostained histopathological images of the RP specimens over four selected areas; that is, areas with high- and low-intensity PAI signals in normal prostatic tissue and areas peripheral to and inside of an index tumor, based on the correlation of PA signal intensity with three microvascular parameters; namely, microvascular density (MVD), total vascular area (TVA), and total vascular length (TVL), where MVD was defined by the number of vessels per unit area.

First, from the analysis of the normal prostate tissue, they found that in all three patients, the PA signal intensity, TVA, and TVL in areas with high-intensity PA signals were significantly higher than those in areas with low-intensity PA signals. This was indirect evidence suggesting that PA appearance could describe the distribution of microvasculature in prostatic tissue correctly. Next, from the comparative analysis on the two areas (i.e., peripheral to and inside of an index tumor), they found that the PA signal intensity, TVA, and TVL in the periphery of the index tumors were significantly higher than those inside the index tumors for all three subjects. However, MVDs in the index tumor and peripheral tumor were comparable, with the exception of one subject.

In addition to these findings, it was also observed that all index tumors showed a ring-like PAI appearance consisting of a peripheral area of high signal intensity completely or partially surrounding an area with low signal intensity, which was consistent with the results acquired from a previous breast cancer imaging study (Heijblom et al. 2015), and those tumors were recognized as hypoechoic regions on TRUS imaging. Figure 18i and j respectively shows representative histopathological and combined PA-US images acquired from a subject in which the aforementioned general tendency appeared.

Although the report was limited by the fact that the number of recruited subjects was small and the possibility of a spatial mismatch between the chosen histology and PA image, it demonstrated that PAT had potential in visualizing microvasculature in prostate cancer. Moreover, they demonstrated for the first time that PA signals could be detected at depths greater than 20 mm in actual human subjects.

In 2019, Kothapallie et al. reported another notable achievement in PAT prostate imaging application (Kothapalli et al. 2019). Unlike the other aforementioned groups' systems, in which commercial piezoelectric sensor-based commercial US detectors were employed, they developed an integrated TRUS and PA imaging probe (named TRUSPA) by compactly integrating a lab-made capacitive micromachined US transducer (CMUT) array (64 elements, 5 MHz) and illumination optics into a ~ 23-mm diameter imaging probe (Fig. 18k). They used it to perform an

animal experiment on mice with subcutaneous prostate cancer, and they also demonstrated its actual clinical applicability by imaging human subjects with prostate cancer (n = 20).

Among the numerous imaging results, Figure 18l and m is notable. First, Figure 18l depicts in vivo TRUSPA and PET-MRI imaging results from a patient with proven advanced prostate cancer as evidenced by preoperative PET-MRI that was followed by PET-MRI contrast-targeted biopsy (with MRI-TRUS fusion) of the prostate using a conventional TRUS device. As shown, the TRUSPA device displayed a distinct PA contrast from the right peripheral base of the prostate, which was not present when other prostatic regions of this patient was scanned, a result which was in agreement with PET-MRI results.

In the paper, they also demonstrated first-in-man contrast-enhanced TRUSPA imaging (n = 10) by intravenously administrating FDA-approved ICG solution (2.5 mg/ml) in the dose range of 5 to 75 mg (n = 10). As shown Figure 18m, an example acquired from a patient with biopsy-proven cancer in the left peripheral base of the prostate and captured at 2 min post-injection using an 800-nm laser beam, a PA contrast enhancement was clearly observed after the injection of ICG (25-mg dose). It should be noted that the dose was quite lower than the average dose (10 mg/kg) of MRI contrast agents in humans.

In addition to the encouraging results of the pilot clinical study, their achievement presented several important technical implications. First, unlike other groups' systems (Bell et al. 2016; Horiguchi et al. 2016; Horiguchi et al. 2017), the compact integration was not based on the simple addition of fiber optic illumination units to existing TRUS probes, but on a customized design and fabrication targeting the specific application. Consequently, they could detect PA signals from the dorsal vascular complex located even at ~40 mm depth from the rectal wall of a subject. Second, they achieved the highest imaging speed—10 frames per second (fps), even for the simultaneous B-mode presentation of PA, US, and combined PA-US images—among all array transducer-based, miniaturized PAT probes manufactured in-house. Lastly, they introduced the novel CMUT technology, which is known to be superior to conventional piezoelectric sensors in terms of bandwidth, SNR, and ease of fabrication in forming a 1D or 2D array, to PAT research.

In addition to the prostate imaging application, the report from Qu et al. of the Wang group in 2018 is also notable for its female genital system imaging (Qu et al. 2018). In 2015, Li et al. of the same group also reported a urogenital PA endoscope working in an AR mode for a similar purpose (Li et al. 2014). However, in the new study, they developed a transvaginal fast-scanning optical-resolution PAE probe to understand vascular relationships during cervical remodeling in pregnancy (Fig. 18n). The development of such an imaging probe would be crucial for understanding abnormal delivery issues, such as premature labor. In this regard, the proposed working hypothesis was also reasonable because there were studies reporting that cervical remodeling during pregnancy was associated with increased vascularity. Considering the application, they developed the probe so that it could exhibit a performance such as 250-Hz for the B-scan imaging speed over a 3-mm scanning range—which was

faster than the previous device (Li et al. 2014) by a factor of 10—and 3.1 μm and 46.5 μm for the lateral and axial resolutions, respectively.

With the probe, they imaged two pregnant women and analyzed five images acquired from three different areas (i.e., the sublingual mucosa, the uterine body, and the ectocervix) based on the two vascular parameters: (1) the microvessel density (the number of vessels per unit area) and (2) the total microvascular area (the percentage of area occupied by blood vessels). Notably, although the number of enrolled subjects was too small, they arrived at the tentative conclusion that microvessel density was a more promising parameter for identifying the progress of cervical remodeling compared to total microvascular area, whereas the total microvascular area was a more discriminatory parameter for classifying the type of tissue. Figure 18o represents representative PA vasculature images acquired from the ectocervix of the two subjects. It can be seen that the blood vessels of Subject 2 had a smaller aspect ratio than those of Subject 1 at the same gestational age (36 weeks).

As we already briefly mentioned in the previous IVPA imaging section, there was also another notable achievement demonstrating the tri-modality imaging of PA, US, and OCT reported by Yang et al. of the Zhou group in 2011 (Yang et al. 2011). Although the demonstration was limited to human ovarian tissue imaging ex vivo, further improvement of the technique would have a significant impact on urology in relation to laparoscopic or image-guided surgery applications.

In this section, we reviewed the three active domains of minimally invasive imaging applications for PAT. To summarize, the IVPA application has been the most active area of application because cardiovascular diseases are the leading cause of death in Western countries, and in recent years it is in vivo coronary artery imaging capability has been successfully demonstrated based on a swine model (Cao et al. 2018; Wu et al. 2017). In addition, the prostate imaging of PAT has advanced enough to apply to actual human subjects (Kothapalli et al. 2019; Horiguchi et al. 2016; Horiguchi et al. 2017). Although related imaging probes do not require a higher miniaturization and also have the advantage of relatively easy access to the target area compared to the other two applications—GI endoscopy and IVPA imaging—it was a great achievement that demonstrated image penetration of up to 4 cm in an actual human subject (Kothapalli et al. 2019), which suggests that a similar penetration could also be achieved in GI endoscopy. In short, if a PAE probe were to be realized in such a large form as with a conventional EUS probe (Shami and Kahaleh 2010; Akahoshi and Bapaye 2012), it may be able to provide images of peri-luminal organs.

Overall, the minimally invasive application of PAT continues to face many challenges related to the required imaging probe fabrication because unlike the existing EUS or optical endoscopic probes, a PAE probe requires the integration of both optical and acoustic elements in a small space. Nevertheless, considering the aforementioned fundamental penetration limit of PAT, we expect that this application could ultimately be one of the most important clinical application areas of PAT.

PA Angiography and Lymphangiography

Angiography refers to a technique utilized to visualize the vascular network (i.e., vasculature), a specific blood vessel of interest, or its internal structure in relation to a diagnostic or interventional purpose. Further, lymphangiography refers to a similar procedure but one that is performed to visualize lymph vessels or lymph nodes. For this, US imaging, X-ray imaging (either planar or CT), and MRI have been utilized thus far. Although MRI-based angiography can provide high-quality vasculature images, its clear visualization still requires the injection of a gadolinium-based contrast agent. Moreover, it requires a rather long scanning time, which makes the technique inapplicable for a real-time guidance of other medical procedures; thus, it is mostly utilized for pre- or after-treatment scanning purposes.

On the other hand, US imaging has the advantage of being capable of visualizing large blood vessels without the aid of a contrast agent and also does not have any safety concerns. However, in order to visualize a blood vessel clearly, there must be a sufficient level of blood flow because it relies on the Doppler principle and also requires the use of a contrast agent when it visualizes microvasculature. Due to the limitations of the two techniques, X-ray-based angiography has been a dominant tool and is regarded as a gold standard for numerous important clinical procedures; however, it also requires the injection of an iodine-based contrast agent and involves concern related to radiation hazards caused by X-ray bombardment when it is utilized for real-time imaging. Representative applications include the visualization of cerebral circulation, vascular network in a cancerous organ, and guiding a catheter for interventional cardiology.

As presented in the previous sections, PAT has already demonstrated its superiority of visualizing blood vessels (even microvasculature) without using any contrast agent and also the lymphatic system if it could be properly stained by a contrast agent injected into or around the target region of interest. Since blood vessels and lymphatic systems are the core parts of the circulatory system and also the major pathways of cancer metastasis (Steeg 2006; Alitalo 2011), addition of PAT to clinical angiography would have a significant impact on medicine.

Since the inception of PAT, various results that visualized a superficial vasculature have been steadily reported. Actually, such images were already good examples that indicated the angiographic imaging capability of PAT. However, in order to make PAT applicable to real clinical angiography, as with X-ray, its penetration depth must be extended to larger depths. In such aspects, research outcomes showing a more clinically relevant level (i.e., organ size) of visualization of vasculature began to be reported since the mid-2000s, as the energy level of available laser sources had greatly increased at the time. The breast vasculature images presented in “Breast Cancer Diagnosis” section correspond to related examples. However, in recent years, more encouraging results that visualized the detailed vasculature of various human body sites have been reported. Thus, in this section, although the related reports are relatively fewer than those related to other applications, we introduce several notable research outcomes that reveal the current status and future potential of PA angiography.

First, a report showcased the feasibility of PAT-based in vivo human carotid artery (CA) and jugular vein imaging for the first time (Fig. 19a), which was presented by Dima et al. of the Ntziachristos group in 2012 (Dima and Ntziachristos 2012). In clinic, as with coronary artery imaging, the CA imaging has also been an important subject in relation to atherosclerosis diagnosis, as it is a representative aspect in assessing the possibility of cerebral hemorrhage and ischemic stroke. In the report, they successfully visualized these vessels located 12–18 mm beneath the skin by using a curved array US transducer (5 MHz, 64 elements) with a radius of a curvature of 40 mm and applying a side optical illumination irradiated over a 4 cm × 0.5 cm area with ~26 mJ at 800 nm (Fig. 19b). The imaged features were CA and jugular vein because they could be confirmed by a conventional duplex US that provided combined anatomical and color Doppler US images (Fig. 19c).

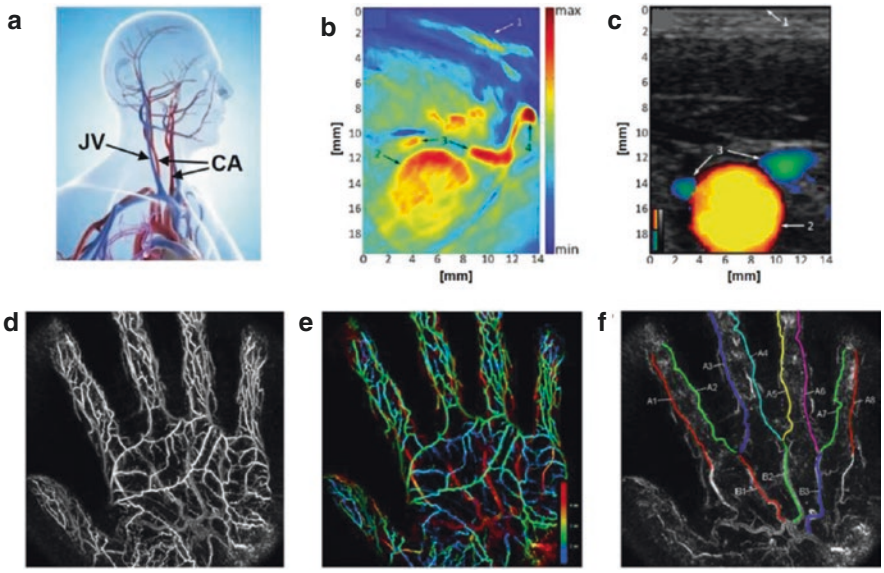

Fig. 19 Examples of reported outcomes showing the feasibility of clinical PA angiography. (**a**) Anatomic diagram presenting the location of the carotid artery (CA) and jugular vein (JV). (**b**) PA cross-sectional image presenting the cardio-vasculature of a female volunteer at the lower neck level; this image was acquired using the developed system (Dima and Ntziachristos 2012). (**c**) Corresponding directional duplex US image (i.e., an image acquired using a different machine) indicating positive flow in yellow/red and negative flow in green/blue. Annotations: 1. Skin surface; 2. Common carotid; 3. Internal jugular vein; 4. External jugular vein. (**d**) PA MAP image (795 nm) showing a human palmar vasculature (Matsumoto et al. 2018). The image was produced using a complete 3D data set acquired by PAI-03. (e) Depth-encoded PA image. (f) Superimposed image of the binarized colored lines extracted from the common and proper palmar digital arteries over an PA background image (gray) after removing the vein signals near the skin's surface. (**g**) Schematics illustrating the postures of a subject during PA imaging (Nagae et al. 2019). (**h**) PA images obtained from various body sites. ⑦ is an image of whole anterolateral thigh (ALT) image. The pink square in ⑦ indicates the corresponding area of the S-factor image presented alongside. In the S-factor image, the two large blood vessels appear to be an artery and vein in the ALT, and the yellow arrow indicates blood vessels that are considered perforators

Fig. 19 (continued)

Since the report, the CA imaging has continued to generate interest. For example, in 2014, Kruizinga et al. of the van Soest group presented a report that investigated CA samples ex vivo by using laser wavelengths that ranged from 1130 nm to 1250 nm (Kruizinga et al. 2014); they found that the atherosclerotic plaques accumulated in a CA wall also could be photoacoustically visualized by the same 1210-nm laser wavelength that was frequently applied in numerous IVPA imaging studies (Jansen et al. 2011; Li et al. 2015), as presented earlier. Moreover, in the report, they also presented a different strategy that photoacoustically imaged CA by applying internal illumination from the pharynx and detecting the generated PA signals externally from a neck surface using an US detector. In addition to the report, there were several follow-up studies that demonstrated (1) a more accurate visualization of anatomical features distributed around the thyroid as well as the CA using a PAT probe custom-designed to better fit the human neck (Dima and Ntziachristos 2016), (2) the first in vivo 2D real-time mapping of the blood flow (US) as well as the oxygen state (PA) of the CA (Mercep et al. 2018), and 3) the first 3D real-time visualization of the structures around the CA (Ivankovic et al. 2019).

In addition to the CA imaging, several research outcomes that demonstrated the potential of PAT for clinical angiography began to be reported in very recent years. Among these, the two papers reported by a Japanese team provided more strong evidence in this regard.

First, in 2018, Matsumoto and Asao et al. (Matsumoto et al. 2018) presented a rather impressive achievement that visualized the detailed vasculature distributed in human hands for the first time by using their third prototype of the HDA-based PAT system (named as "PAI-03"). As mentioned in "Breast Cancer Diagnosis" section, the employed system was originally developed for the breast imaging application (Fig. 12a); however, they improved the previous version for this new study. By using a 795-nm laser wavelength, they imaged palmar blood vessels (Fig. 19d and e) and analyzed their morphology, particularly focusing on the curvature parameters of the common and proper palmar digital arteries. However, for the analysis, it was necessary to remove the signals from superficial veins first to better distinguish the targeted arteries (Fig. 19f). In this manner, they analyzed the 3D palmar vasculature PA data acquired from 23 healthy subjects (12 females and 11 males) in an age range of between 22 and 59 years; interestingly, they found that the level of the tortuousness increased with age regardless of the sex.

After this report, in 2019, the research team also presented another notable research result that visualized vasculatures distributed in several body sites of a human subject (Nagae et al. 2019). The recruited subject was a male in his 50s, and the imaging experiment was performed using their fifth prototype (named "PAI-05"), which was further improved from the previous version in terms of the number of detection channels (now 1024-chs), scanning pattern (rectangular spiral), and the ease in positioning a target area. Thus, it was possible to position various body sites—such as hand, foot, arm, and thigh—on the scanner (as depicted in the illustrations presented in Figure 19g) and acquire nice vasculature images from the mentioned areas (as shown in Figure 19h), which were the first-of-its-kind in PAT. Moreover, by performing a dual-wavelength PA imaging (756 nm and 797 nm), they also demonstrated the sO_2 mapping capability of the developed system (see the magnified color image extended from the anterolateral thigh image).

Thus far, such a detailed vasculature analysis of human extremities has not been facilely attempted in clinic due to the limited availability of conventional imaging modalities and the cost issue. However, this has now become possible, as PAT can provide vasculature images with unprecedented image quality. Based on the presented demonstrations, the authors commented that the information provided on vascular morphology and related parameters, like arterial tortuousness, would be important information representing individuals' lifestyles, medical history, and disease symptoms. Moreover, apart from the evident medical implications, the new angiographic imaging technique could also extend into the fields of healthcare and beauty, for example, to treat issues such as varicose veins.

Then, could PAT eventually replace the conventional X-ray-based clinical angiography? Of course, it would be difficult to replace this due to its relatively lower penetration depth. However, it may be still possible for some areas or at least it may be realized in such a form as to complement or aid conventional procedures. As evident from the examples discussed in other sections, there was a case in which PAT detected signals from a maximum depth of ~5-cm, even in actual human tissue

imaging in vivo. In particular, the real-time and label-free safe nonionizing imaging capability of PAT would make the expectation rather feasible. Moreover, PAT has the unique imaging ability of distinguishing between a vein and an artery, which could make a critical contribution to interventional cardiology by aiding related procedures, like the arterial introduction of a catheter.

Thus far, we have discussed the potential of PAT for clinical angiography. However, in comparison, there are fewer studies involving PAT-based lymphangiography. This is because in order to visualize the lymphatic system, it is necessary to administrate an appropriate contrast agent, like methylene blue. Nevertheless, here we briefly review related progress because the lymphatic system is another important circulatory system in addition to the vascular system and is also another area in which PAT can function effectively.

As previously mentioned, the first PAT-based lymphatic system imaging was demonstrated by Song et al. of the Wang group in 2008 in relation to the SLN mapping in a rat (Fig. 20a) (Song et al. 2008). Thereafter, a number of papers were further documented in the category, particularly in relation to the development of a contrast agent that enabled more effective visualization by increasing its drainage efficiency into the lymphatic system or by increasing its optical detection sensitivity. For example, in 2010, Pan et al. investigated the size dependence of gold nanobeacons (GNBs) for SLN detection and found that smaller GNBs were noted trafficking through the lymphatic system and accumulating more efficiently in the lymph nodes in comparison to larger GNBs (Pan et al. 2010). In addition, in 2009, Kim and Zharov et al. demonstrated a dual-modality PA and photothermal mapping of lymphatic endothelial cells—which line the internal surface of lymphatic vessels—by using golden carbon nanotubes (GNTs) conjugated with an antibody specific to the lymphatic endothelial hyaluronan receptor-1 (Kim et al. 2009). As the GNTs were engineered to provide an enhanced PA contrast as high as ~10^2-fold, they were able to successfully visualize lymphatic vessels in mice even using an extremely low laser fluence of a few mJ/cm^2 (Fig. 20b and c).

Although the mentioned papers demonstrated the potential of PAT for the imaging of the lymphatic system, they were all limited to proof-of-concept studies based on animal models. However, in 2015, in addition to the aforementioned report by Alejandro et al. of the Wang group (Garcia-Uribe et al. 2015), Stoffels et al. of the Klode group also presented human SLN imaging results acquired from their first pilot clinical study performed in relation to melanoma metastasis (Stoffels et al. 2015). Notably, by using ICG as a contrast agent, they could reliably map SLNs in 20 patients in vivo, with a 100% concordance with conventional ^{99m}Tc-marked SLN lymphoscintigraphy. Moreover, they detected SLNs located even up to a depth of 5 cm—whose measure was based on a natural state and whose location was identified by SPECT/CT—by applying pressure during the PAT image acquisition to reduce the distance between the SLNs and the surface of the skin (Fig. 20d). Figure 20e represents a PA image displaying a spectrally unmixed ICG signal in an SLN overlaid on a structural image acquired at 800 nm. Overall, from the in vivo study, they were able to photoacoustically identify SLNs without any false negative and with 100% sensitivity and 48% specificity.

Although the report was also significant in terms of the first-in-human study related to melanoma, it was mostly focused on mapping a lymph node rather than

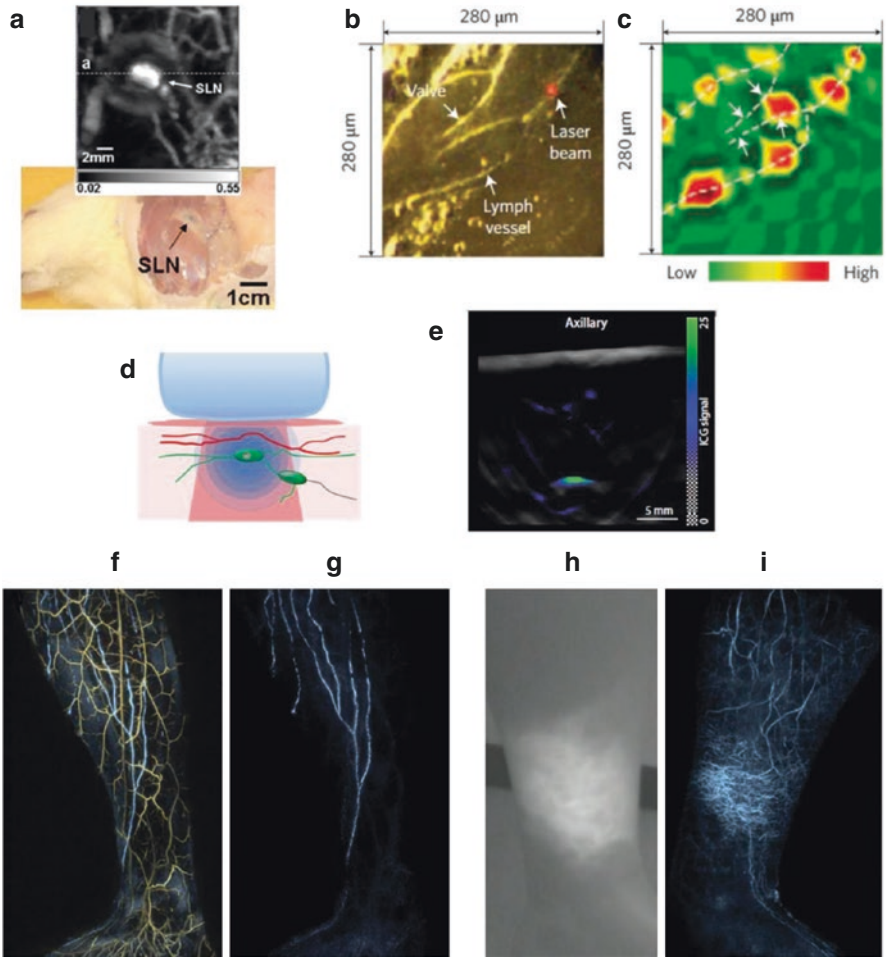

Fig. 20 Representative reports demonstrating preclinical lymphatic system imaging and the feasibility of clinical PA lymphangiography. (**a**) PA MAP image (upper) acquired 52-min post-injection, in which the stained SLN was visualized, and photo (lower) with skin removed after the PA imaging (Song et al. 2008). (**b**) Conventional microscope image showing the imaged area in a fragment of mouse mesentery (Kim et al. 2009). (**c**) Corresponding PA image (850 nm) acquired in vivo at 60 min after the administration of antibody-GNTs, which was engineered to target the lymphatic system. Dashed white lines indicate the lymphatic wall and valve. Arrows indicate valve leaflets. (**d**) A schematic illustrating the PA detection of a SLN indicated by ICG in conjunction with a handheld PA imaging probe (Stoffels et al. 2015). (**e**) Representative preoperative PA image of axillary SLN, with ICG signal (green) overlaid on a single-wavelength (800 nm) background image (gray). (**f**) The medial-side view of the PA angiography and lymphangiography of the right lower leg of a woman in her thirties without any past medical history; this image depicts both lymphatic vessels and venules (Kajita et al. 2019). (**g**) PA image showing lymphatic vessels only. (**h**) The medial-side view of the conventional fluorescence lymphography of the left lower leg of a 47-year-old woman with secondary lymphedema. (**i**) The PA lymphangiography of the same part, depicting only lymphatic vessels

visualizing lymphatic vasculature. However, in 2019, Kajita et al. presented an impressive result that achieved the first human lymph vessel imaging by using ICG as a contrast agent (Kajita et al. 2019). For the study, they employed the same PAT system called "PAI-05" utilized for the human angiography imaging presented in Figure 19g and imaged 20 healthy subjects and 30 lymphedema patients by administering ICG subcutaneously to the dorsal aspect of each foot or hand, as done in fluorescence lymphography.

Surprisingly, as depicted in Figure 20f, the PAT system could visualize lymphatic vessels and their neighboring venules with a spatial resolution as fine as 0.2 mm; Figure 20g depicts only lymphatic vessels. Indeed, this is a significant achievement that acquired a PAT-based human lymphatic vessel image for the first time. In order to showcase the superiority of PAT, they also presented a conventional fluorescence lymphographic image (Fig. 20h) along with a corresponding PAT image (Fig. 20i) obtained from a lymphedema patient. As illustrated, only the PAT system could clearly differentiate the dense interconnecting 3D structures of the lymphatic vessels distributed around the leg of the patient. In the paper, they only presented representative images obtained from healthy and lymphedema subjects. However, they stated that it would possible to analyze morphological patterns with the acquired lymphatic data and running course of each lymphatic vessel, along with their comparisons to accompanying venules, which would be reported elsewhere.

As presented, only the three papers involved human subjects and demonstrated more direct feasibility of PAT-based lymphangiography (Garcia-Uribe et al. 2015; Stoffels et al. 2015; Kajita et al. 2019). Although the related application is relatively more challenging because there is a fundamental issue regarding how to effectively deliver a contrast agent to the lymph system, PAT is expected to make a crucial contribution to clinical lymphangiography because it is an undeniable fact that once a targeted lymphatic structure is successfully stained, PAT can provide a much clearer contrast on it compared to conventional US imaging.

Other Notable Clinical Applications

Although the aforementioned clinical application areas are dominant in terms of the number of publications, there remain numerous other important applications that must be noted. Among these, PAT-based circulating tumor cell (CTC) detection as well as an intraoperative imaging application appear to be promising and of particular importance.

The first subject was mostly pioneered by the Zharov group in relation to the PAT-based flow cytometry technique development (Galanzha and Zharov 2012), and the result presented in Figure 20c could be understood as one of the related outcomes. In particular, in 2009, Galanzha et al. of the Zharov group also reported another notable article that presented a novel method to increase the possibility of CTC detection in the bloodstream (Galanzha et al. 2009). By applying a magnetic enrichment concept along with the use of dual chemical agents—that is, GNTs and magnetic nanoparticles—which were engineered to target human breast cancer cells, they could significantly increase the PA signal intensity generated by the magnetically captured tumor cells (e.g., ~88-fold increase in an in vivo mouse model).

Thereafter, similar approaches also began to be addressed by other groups. For example, in 2010, Jin et al. reported iron oxide and gold-coupled core-shell nanoparticles that could be utilized as a multifunctional contrast agent for multi-modality imaging—for example, MRI as well as the magnetomotive PAT (Jin et al. 2010). In addition, in the paper reported by He et al. of the Wang group in 2016 (He et al. 2016), they demonstrated an imaging-based single melanoma tumor cell detection in a bloodstream by applying the OR-PAM technique (Figs. 21a–c) as well as its on-the-spot laser killing.

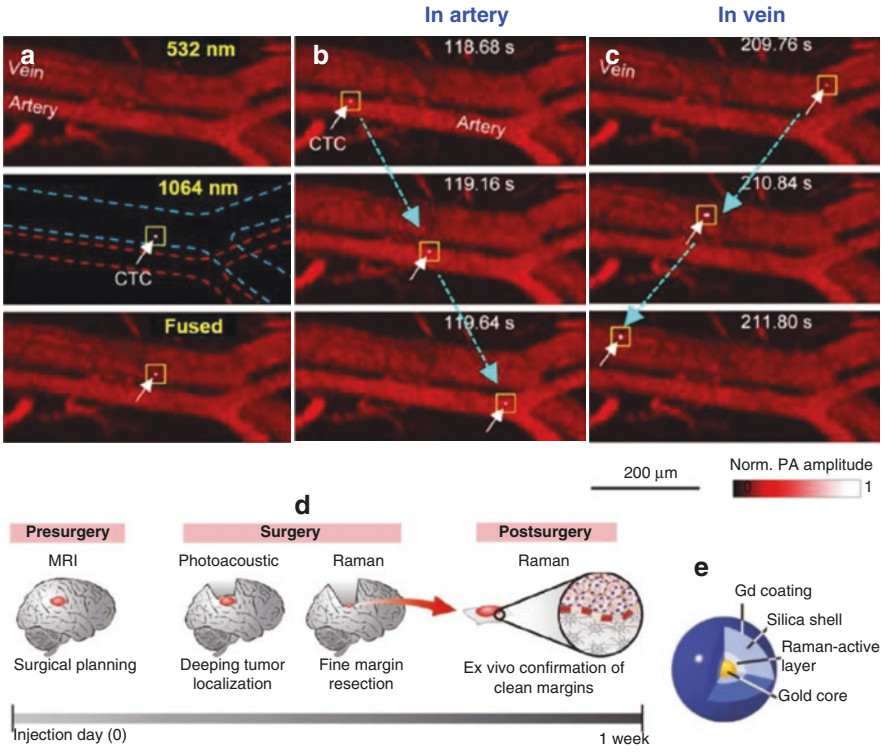

Fig. 21 PAT-based CTC detection and intraoperative imaging applications. (**a**) Snapshots showing single CTCs travelling in vasculature: 532-nm laser-induced (top), 1064-nm laser-induced (middle), and fused (bottom) flow cytography images (He et al. 2016). In the 1064-nm image, the white arrow and yellow square indicate the detected CTC; the red and blue dashed lines delineate the artery and vein boundaries, respectively. (**b**) Three fused snapshots spanning ~1 s revealing a single CTC traveling in the artery. (**c**) Three fused snapshots spanning ~2 s revealing a single CTC traveling in the vein. The times labeled in (**b**) and (**c**) are relative to CTC injection. (d) A diagram illustrating the strategy of the triple-modality MPR imaging-based brain tumor surgery (Kircher et al. 2012). (**e**) Approximate structure of the developed MPR nanoparticle. (**f**) A mouse model-based in vivo demonstration of the proposed strategy. Images from the left to the right columns are 2D axial MRI, PA, and Raman images, respectively. The post-injection images (lower row) of all the three modalities showed clear tumor visualization (dashed boxes outline the imaged area). (**g**) An in vivo surgical demonstration of a sequentially resected a brain tumor. Quarters of the tumor were sequentially removed (upper row) and intraoperative Raman imaging was performed after each resection step (lower row) until the entire tumor had been removed, as assessed by visual inspection. (**h**) The proposed imaging concept for the PAT-guided pituitary tumor surgery (left) and coronal view of the anatomy surrounding the sphenoid bone (right) (Lediju Bell et al. 2015a; Delman 2009)

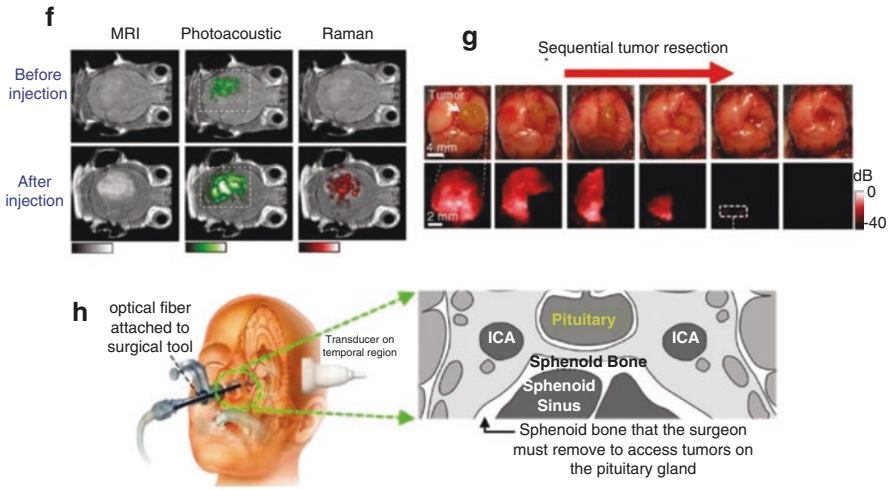

Fig. 21 (continued)

As presented, a key issue in CTC detection is to increase detection sensitivity or possibility. Surprisingly, Galanzha et al. of the Zharov group in 2019 (Galanzha et al. 2019) demonstrated their technique's in vivo clinical applicability by successfully detecting CTCs in the skins of 27 out of 28 patients with melanoma, with a detection sensitivity as low as 1 CTC/liter of blood. Moreover, they also successfully showcased the feasibility of laser illumination-based CTC eradication even in a human subject. As CTCs are regarded as potential indicators for tumor metastasis, in vivo detection of these CTCs is a critical issue in clinics for early diagnosis and treatment of cancer.

In relation to the intraoperative imaging application of PAT, the development of a dedicated miniaturized imaging probe, such as laparoscopic or handheld probes, is rather urgent and promising because there are numerous unmet needs in clinics—for example, although an MRI can provide a clear view of a tumor region, it is not directly applicable for an actual surgery. In this regard, in 2012, Kircher et al. of the Gambhir group proposed a feasible strategy that could more effectively remove a brain tumor based on the synergetic effect derived from the combined use of the three imaging modalities—MRI, PAT, and Raman (Kircher et al. 2012). As per the strategy, 1) MRI is performed for preoperative macroscopic delineation of the brain tumor; 2) PAT for intraoperative high-resolution and deep 3D imaging; and 3) Raman for intraoperative high sensitivity, high specificity, and high-resolution surface imaging of tumor margins (Fig. 21d). In order to make the strategy more effective in actual clinical settings, they also developed a dedicated contrast agent called the MRI-PA-Raman (MPR) nanoparticle (Fig. 21e), which could be utilized as a common contrast agent for the three mentioned imaging techniques (Fig. 21f). Figure 21g depicts an actual photo of the dissection of a brain tumor according to the strategy.

In addition to the brain imaging application, other reports also suggested PAT as a guiding tool for other surgical procedures, such as those related to prostate tumor

(Lediju Bell et al. 2015b) and pituitary tumor (Lediju Bell et al. 2015a). Figure 21h depicts a related example that addressed a PAT-guided pituitary tumor surgery based on an endonasal transsphenoidal approach.

Summary and Outlook

In this chapter, we reviewed the development history of PAT, mostly focusing on several key application areas that have been actively investigated over the previous two decades. However, as new applications and methodologies continue to be presented even currently, like the several examples that we briefly mentioned above, it is also highly expected that a completely new field of application or new embodiments that are beyond our current expectations could continuously emerge. This is probably due to the versatile contrast creation capability of PAT, which is based on the unique optical contrast mechanism termed "light absorption," and the distinct system embodiment feature that uses the conventional US imaging technique.

Of course, although in this review, we mainly highlighted the positive aspects of PAT, it is an undeniable fact that the imaging depth of PAT is relatively lower than that of existing mainstream imaging modalities, such as the MRI, CT, and US imaging techniques. However, it is also true that no other biomedical imaging technique, among all those that have emerged after current clinical mainstream imaging modalities, can provide such high-resolution images as PAT at depths reaching several centimeters in vivo (thus far, signal detection in a depth of ~5 centimeters has been recorded as the maximum in PAT); this is probably the core aspect that accounts for why PAT is currently the most rapidly growing technique in the biomedical imaging field compared to other imaging techniques, thereby indirectly suggesting the importance of PAT technology. Most of all, the unique anatomical, functional, and molecular imaging capability—which is not possible with the conventional mainstream imaging modalities but affordable in real time by PAT—will make a significant contribution to biomedicine in the future by enabling numerous breakthroughs and also paving the way for new medical imaging paradigms.

Further, the technical aspect that PAT can be easily integrated with the conventional US imaging technique—which is currently regarded as one of the three core tomographic imaging modalities in clinics—must also be importantly evaluated because based on the integration, PAT could provide a feasible solution or new innovation for numerous scattered issues in the current clinical application areas of US imaging, for which conventional methods or procedures face limitations. Simply speaking, the emergence of PAT has enabled color visibility in the US imaging technique, thereby enabling better identification and characterization of suspect tissues; this event could probably be likened to a previous historic event like when black-and-white TVs were replaced with color TVs in the previous century.

As discussed above, in biological application, the role and contribution of PAT for small animal whole-brain and whole-body imaging is expected to be particularly unique and, thus, be ultimately successful in the near future. In the clinical application, the breast cancer diagnostic application appears to be in a state that is closest to the final clinical translation compared to other application areas. In addition, new

light is currently being shed on the dermatological applications of PAT due to the recent innovations that have been presented. Moreover, the endoscopy and minimally invasive imaging applications of PAT are also expected to be successfully translated into clinics because there are numerous attractive clinical issues and also a corresponding number of efforts being made. Moreover, based on the unprecedented image quality for visualization of the vascular and lymphatic systems, which are the two core circulation systems, there is also a high expectation of the development of new forms of applications and contributions of PAT in clinical angiography and lymphangiography.

Although only several core application areas were mainly introduced in this chapter, there are numerous other notable and interesting application areas that could become more significant in the future. For example, in a case in which AI was applied to skin vascular analysis (Moustakidis et al. 2019), the incorporation of smart AI technology into PAT would make a critical contribution to clinical application by enabling early detection of disease symptoms and more accurate characterization of suspicious tissues in dermatological and numerous other applications areas, based on the rich spectroscopic and functional information on the vasculature and associated biomarkers provided by PAT.

Of course, however, additional efforts must be made for successful clinical translations. First, more precise and clear protocols and criteria on related imaging procedures and quality assurance must be established. Moreover, numerous technical standards necessary for related system embodiments—such as the one related to a light illumination parameter as well as for the quantification of related imaging performances, such as imaging depth and resolution—must be established. In addition, it will be necessary to further lower the cost of implementing related systems and also improve overall imaging performance. In particular, further improvements in imaging depth will be most critical, as current imaging depth is still insufficient to achieve broader clinical applications. Although this may not be essential for certain applications, such as the IVPA imaging and dermatological applications, significant improvements in the image depth will ensure the successful clinical translation of PAT. The results presented in this chapter represent the achievements in the development of PAT over the past ~25 years. We look forward to the full maturation of PAT in the next 25 years, when it becomes a commonly used imaging technique—for example, in hospitals.

Acknowledgments This work was supported by the U-K Brand Research Fund (1.200032.01) of UNIST (Ulsan National Institute of Science and Technology) and Basic Science Research Program through the National Research Foundation (NRF) of Korea funded by the Ministry of Education (2015R1D1A1A01059361).

References

Aguirre J, Schwarz M, Garzorz N et al (2017) Precision assessment of label-free psoriasis biomarkers. Nat Biomed Eng 1:0068

Akahoshi K, Bapaye A (2012) Practical handbook of endoscopic ultrasonography. Publisher. Springer Japan, Tokyo

Alitalo K (2011) The lymphatic vasculature in disease. Nat Med 17:1371–1380

Allen TJ, Hall A, Dhillon AP et al (2012) Spectroscopic photoacoustic imaging of lipid-rich plaques in the human aorta in the 740 to 1400 nm wavelength range. J Biomed Opt 17:061209. https://doi.org/10.1117/1.JBO.17.6.061209

Amornphimoltham P, Masedunskas A, Weigert R (2011) Intravital microscopy as a tool to study drug delivery in preclinical studies. Adv Drug Deliv Rev 63:119–128

Andreev V, Karabutov A, Solomatin S et al (2000) "Optoacoustic tomography of breast cancer with arc-array transducer", Proc SPIE 3916. Biomedical Optoacoustics:36–47

Ansari R, Zhang EZ, Desjardins AE et al (2018) All-optical forward-viewing photoacoustic probe for high-resolution 3D endoscopy. Light Sci Appl 7:75

Asao Y, Hashizume Y, Suita T et al (2016) Photoacoustic mammography capable of simultaneously acquiring photoacoustic and ultrasound images. J Biomed Opt 21:116009

Bai X, Gong X, Hau W et al (2014) Intravascular optical-resolution photoacoustic tomography with a 1.1 mm diameter catheter. PLoS One 9:e92463

Beard P (2011) Biomedical photoacoustic imaging. Interface Focus 1:602–631

Beard PC, Pérennès F, Draguioti E, Mills TN (1998) Optical fiber photoacoustic-photothermal probe. Opt Lett 23(15):1235–1237

Bell KL, Harrison T, Usmani N et al (2016) "Integrated transrectal probe for translational ultrasound-photoacoustic imaging", Proc SPIE 9708, Photons Plus Ultrasound: Imaging and Sensing 2016, 97080A

Boas DA, Brooks DH, Miller EL et al (2001) Imaging the body with diffuse optical tomography. IEEE Signal Process Mag 18(6):57–75

Brecht HP, Su R, Fronheiser M et al (2009) Whole-body three-dimensional optoacoustic tomography system for small animals. J Biomed Opt 14:064007. https://doi.org/10.1117/1.3259361

Brown E, Brunker J, Bohndiek SE (2019) Photoacoustic imaging as a tool to probe the tumour microenvironment. Dis Model Mech 12:dmm039636

Brunker J, Beard P (2016) Velocity measurements in whole blood using acoustic resolution photoacoustic Doppler. Biomed Opt Express 7(7):2789–2806

Brunker J, Yao J, Laufer J et al (2017) Photoacoustic imaging using genetically encoded reporters: a review. J Biomed Opt 22(7):070901

Bücking TM, van den Berg PJ, Balabani S et al (2018) Processing methods for photoacoustic Doppler flowmetry with a clinical ultrasound scanner. J Biomed Opt 23(2):1–8

Buehler A, Herzog E, Razansky D et al (2010) Video rate optoacoustic tomography of mouse kidney perfusion. Opt Lett 35(14):2475–2477

Buxton RB, Frank LR (1997) A model for the coupling between cerebral blood flow and oxygen metabolism during neural stimulation. J Cereb Blood Flow Metab 17(1):64–72

Cao Y, Hui J, Kole A et al (2016) High-sensitivity intravascular photoacoustic imaging of lipid-laden plaque with a collinear catheter design. Sci Rep 6:25236

Cao Y, Kole A, Hui J et al (2018) Fast assessment of lipid content in arteries in vivo by intravascular photoacoustic tomography. Sci Rep 8(1):2400

Cao R, Li J, Ning B et al (2017) Functional and oxygen-metabolic photoacoustic microscopy of the awake mouse brain. NeuroImage 150:77–87

Chaigne T, Arnal B, Vilov S et al (2017) Super-resolution photoacoustic imaging via flow-induced absorption fluctuations. Optica 4(11):1397–1404

Chaigne T, Gateau J, Allain M et al (2016) Super-resolution photoacoustic fluctuation imaging with multiple speckle illumination. Optica 3(1):54–57

Chatni MR, Yao J, Danielli A et al (2011) Functional photoacoustic microscopy of pH. J Biomed Opt 16:100503

Chee RKW, Li Y, Zhang W et al (2018) In vivo photoacoustic difference-spectra imaging of bacteria using photoswitchable chromoproteins. J Biomed Opt 23:1–11

Chen QX, Davies A, Dewhurst RJ et al (1993) Photo-acoustic probe for intra-arterial imaging and therapy. Electron Lett 29(18):1632–1633

Chen YS, Frey W, Kim S et al (2011) Silica-coated gold nanorods as photoacoustic signal nanoamplifiers. Nano Lett 11(2):348–354

Cheney M, Isaacson D, Newell JC (1999) Electrical impedance tomography. SIAM Rev 41(1):85–101

Conkey DB, Caravaca-Aguirre AM, Dove JD et al (2015) Super-resolution photoacoustic imaging through a scattering wall. Nat Commun 6:7902
Cox B, Laufer JG, Arridge SR et al (2012) Quantitative spectroscopic photoacoustic imaging: a review. J Biomed Opt 17:061202
Danielli A, Maslov KI, Garcia-Uribe A et al (2014) Label-free photoacoustic nanoscopy. J Biomed Opt 19(8):086006
De la Zerda A, Zavaleta C, Keren S et al (2008) Carbon nanotubes as photoacoustic molecular imaging agents in living mice. Nat Nanotechnol 3(9):557–562
Deán-Ben XL, Fehm TF, Ford SJ et al (2017c) Spiral volumetric optoacoustic tomography visualizes multi-scale dynamics in mice. Light Sci Appl 6:e16247
Deán-Ben XL, Gottschalk S, Mc Larney B et al (2017b) Advanced optoacoustic methods for multiscale imaging of in vivo dynamics. Chem Soc Rev 46:2158–2198
Deán-Ben XL, López-Schier H, Razansky D (2017a) Optoacoustic micro-tomography at 100 volumes per second. Sci Rep 7:6850
Deán-Ben XL, Razansky D (2018) Localization optoacoustic tomography. Light-Sci Appl 7:18004
Deán-Ben XL, Stiel AC, Jiang Y et al (2015) Light fluence normalization in turbid tissues via temporally unmixed multispectral optoacoustic tomography. Opt Lett 40(20):4691–4694
Delman BN (2009) Imaging of pediatric pituitary abnormalities. Endocrinol Metab Clin N Am 38(4):673–698
Denk W, Strickler J, Webb W (1990) Two-photon laser scanning fluorescence microscopy. Science 248(4951):73–76
Dima A, Ntziachristos V (2012) Non-invasive carotid imaging using optoacoustic tomography. Opt Express 20:25044–25057
Dima A, Ntziachristos V (2016) In-vivo handheld optoacoustic tomography of the human thyroid. Photo-Dermatology 4:65–69
Drexler W, Fujimoto JG (2015) Optical coherence tomography technology and applications, 2nd edn. Springer International Publishing, Cham. Imprint: Springer
Ermilov SA, Khamapirad T, Conjusteau A et al (2009) Laser optoacoustic imaging system for detection of breast cancer. J Biomed Opt 14(2):024007. https://doi.org/10.1117/1.3086616
Esenaliev RO, Karabutov AA, Tittel FK et al (1997) "Laser optoacoustic imaging for breast cancer diagnostics: limit of detection and comparison with x-ray and ultrasound imaging", Proc SPIE 2979, Optical Tomography and Spectroscopy of Tissue: Theory, Instrumentation, Model, and Human Studies II, 71–82
Fakhrejahani E, Torii M, Kitai T et al (2015) Clinical report on the first prototype of a photoacoustic tomography system with dual illumination for breast cancer imaging. PLoS One 10:e0139113
Fang H, Maslov K, Wang LV (2007) Photoacoustic Doppler effect from flowing small light-absorbing particles. Phys Rev Lett 99:184501
Favazza CP, Jassim O, Cornelius LA et al (2011) In vivo photoacoustic microscopy of human cutaneous microvasculature and a nevus. J Biomed Opt 16(1):016015. https://doi.org/10.1117/1.3528661
Filonov GS, Krumholz A, Xia J et al (2012) Deep-tissue photoacoustic tomography of a genetically encoded near-infrared fluorescent probe. Angew Chem Int Ed Engl 51(6):1448–1451
Folarin AA, Konerding MA, Timonen J et al (2010) Three-dimensional analysis of tumour vascular corrosion casts using stereoimaging and micro-computed tomography. Microvasc Res 80(1):89–98
Fukumura D, Duda DG, Munn LL et al (2010) Tumor microvasculature and microenvironment: novel insights through intravital imaging in pre-clinical models. Microcirculation 17:206–225
Galanzha EI, Menyaev YA, Yadem AC et al (2019) In vivo liquid biopsy using cytophone platform for photoacoustic detection of circulating tumor cells in patients with melanoma. Sci Transl Med 11(496):eaat5857
Galanzha EI, Shashkov EV, Kelly T et al (2009) In vivo magnetic enrichment and multiplex photoacoustic detection of circulating tumour cells. Nat Nanotechnol 4:855–860
Galanzha EI, Zharov VP (2012) Photoacoustic flow cytometry. Methods 57(3):280–296

Gamelin J, Aguirre A, Maurudis A et al (2008) Curved array photoacoustic tomographic system for small animal imaging. J Biomed Opt 13(2):024007
Gamelin J, Maurudis A, Aguirre A et al (2009) A real-time photoacoustic tomography system for small animals. Opt Express 17(13):10489–10498
Garcia-Uribe A, Erpelding TN, Krumholz A et al (2015) Dual-modality photoacoustic and ultrasound imaging system for noninvasive sentinel lymph node detection in patients with breast cancer. Sci Rep 5:15748
Ghim CM, Lee SK, Takayama S, Mitchell RJ (2010) The art of reporter proteins in science: past, present and future applications. BMB Rep 43(7):451–460
Gora MJ, Sauk JS, Carruth RW et al (2013) Tethered capsule endomicroscopy enables less invasive imaging of gastrointestinal tract microstructure. Nat Med 19:238–240
Gottschalk S, Degtyaruk O, Mc Larney B et al (2019) Rapid volumetric optoacoustic imaging of neural dynamics across the mouse brain. Nat Biomed Eng 3:392–401
Gujrati V, Mishra A, Ntziachristos V (2017) Molecular imaging probes for multi-spectral optoacoustic tomography. Chem Commun (Camb) 53(34):4653–4672
Guo Z, Ye Z, Shao W et al (2019) Miniature probe for optomechanical focus adjustable optical resolution photoacoustic endoscopy. arXiv e-prints, arXiv:1909522
Hanahan D, Weinberg RA (2011) Hallmarks of cancer: the next generation. Cell 144(5):646–674
He H, Stylogiannis A, Afshari P et al (2019) Capsule optoacoustic endoscopy for esophageal imaging. J Biophotonics 12(10):e201800439
He Y, Wang L, Shi J et al (2016) In vivo label-free photoacoustic flow cytography and on-the-spot laser killing of single circulating melanoma cells. Sci Rep 6:39616
Heijblom M, Piras D, Brinkhuis M et al (2015) Photoacoustic image patterns of breast carcinoma and comparisons with magnetic resonance imaging and vascular stained histopathology. Sci Rep 5:11778
Helmchen F, Denk W (2005) Deep tissue two-photon microscopy. Nat Methods 2(12):932–940
Henrichs PM, Meador JW, Fuqua JM et al (2005) "Atherosclerotic plaque characterization with optoacoustic imaging", Proc SPIE 5697, Photons Plus Ultrasound: Imaging and Sensing 2005: The Sixth Conference on Biomedical Thermoacoustics, Optoacoustics, and Acoustooptics, 217–223
Hochuli R, An L, Beard PC et al (2019) Estimating blood oxygenation from photoacoustic images: can a simple linear spectroscopic inversion ever work? J Biomed Opt 24(12):1–13
Horiguchi A, Shinchi M, Nakamura A et al (2017) Pilot study of prostate cancer angiogenesis imaging using a photoacoustic imaging system. Urology 108:212–219
Horiguchi A, Tsujita K, Irisawa K et al (2016) A pilot study of photoacoustic imaging system for improved real-time visualization of neurovascular bundle during radical prostatectomy. Prostate 76(3):307–315
Hsieh BY, Chen SL, Ling T et al (2012) All-optical scanhead for ultrasound and photoacoustic dual-modality imaging. Opt Express 20:1588–1596
Hsu HC, Wang L, Wang LV (2016) In vivo photoacoustic microscopy of human cuticle microvasculature with single-cell resolution. J Biomed Opt 21(5):56004. https://doi.org/10.1117/1.JBO.21.5.056004
Hu S, Maslov K, Tsytsarev V et al (2009a) Functional transcranial brain imaging by optical-resolution photoacoustic microscopy. J Biomed Opt 14:040503
Hu S, Maslov K, Wang LV (2011) Second-generation optical-resolution photoacoustic microscopy with improved sensitivity and speed. Opt Lett 36:1134–1136
Hu S, Wang LV (2010) Neurovascular photoacoustic tomography. Front Neuroenerg 2:10
Hu S, Yan P, Maslov K et al (2009b) Intravital imaging of amyloid plaques in a transgenic mouse model using optical-resolution photoacoustic microscopy. Opt Lett 34(24):3899–3901
Hudson SV, Huang JS, Yin W et al (2014) Targeted noninvasive imaging of EGFR-expressing orthotopic pancreatic cancer using multispectral optoacoustic tomography. Cancer Res 74(21):6271–6279
Hui J, Cao Y, Zhang Y et al (2017) Real-time intravascular photoacoustic-ultrasound imaging of lipid-laden plaque in human coronary artery at 16 frames per second. Sci Rep 7(1):1417

Hui J, Yu Q, Ma T et al (2015) High-speed intravascular photoacoustic imaging at 1.7 μm with a KTP-based OPO. Biomed Opt Express 6(11):4557–4566
Huynh E, Leung BY, Helfield BL et al (2015) In situ conversion of porphyrin microbubbles to nanoparticles for multimodality imaging. Nat Nanotechnol 10(4):325–332
Ivankovic I, Mercep E, Schmedt CG et al (2019) Real-time volumetric assessment of the human carotid artery: handheld multispectral optoacoustic tomography. Radiology 291:45–50
Jansen K, Van Der Steen AF, Van Beusekom HM et al (2011) Intravascular photoacoustic imaging of human coronary atherosclerosis. Opt Lett 36:597–599
Jathoul AP, Laufer J, Ogunlade O et al (2015) Deep in vivo photoacoustic imaging of mammalian tissues using a tyrosinase-based genetic reporter. Nat Photonics 9(4):239
Jin Y, Jia C, Huang SW et al (2010) Multifunctional nanoparticles as coupled contrast agents. Nat Commun 1:41
Jo J, Lee CH, Kopelman R et al (2017) In vivo quantitative imaging of tumor pH by nanosonophore assisted multispectral photoacoustic imaging. Nat Commun 8:471
Kajita H, Oh A, Urano M et al (2019) Photoacoustic lymphangiography. J Surg Oncol 121:48–50
Karpiouk AB, Wang B, Amirian J et al (2012) Feasibility of in vivo intravascular photoacoustic imaging using integrated ultrasound and photoacoustic imaging catheter. J Biomed Opt 17(9):96008. https://doi.org/10.1117/1.JBO.17.9.096008
Karpiouk AB, Wang B, Emelianov SY (2010) Development of a catheter for combined intravascular ultrasound and photoacoustic imaging. Rev Sci Instrum 81:014901
Kiesslich R, Burg J, Vieth M et al (2004) Confocal laser endoscopy for diagnosing intraepithelial neoplasias and colorectal cancer in vivo. Gastroenterology 127:706–713
Kiesslich R, Goetz M, Vieth M et al (2007) Technology insight: confocal laser endoscopy for in vivo diagnosis of colorectal cancer. Nat Clin Pract Oncol 4:480–490
Kiesslich R, Gossner L, Goetz M et al (2006) In vivo histology of Barrett's esophagus and associated neoplasia by confocal laser endomicroscopy. Clin Gastroenterol Hepatol 4:979–987
Kim JW, Galanzha EI, Shashkov EV et al (2009) Golden carbon nanotubes as multimodal photoacoustic and photothermal high-contrast molecular agents. Nat Nanotechnol 4:688–694
Kircher MF, De La Zerda A, Jokerst JV et al (2012) A brain tumor molecular imaging strategy using a new triple-modality MRI-photoacoustic-Raman nanoparticle. Nat Med 18:829–834
Kitai T, Torii M, Sugie T et al (2014) Photoacoustic mammography: initial clinical results. Breast Cancer 21:146–153
Knox HJ, Hedhli J, Kim TW et al (2017) A bioreducible N-oxide-based probe for photoacoustic imaging of hypoxia. Nat Commun 8:1794
Kothapalli SR, Sonn GA, Choe JW et al (2019) Simultaneous transrectal ultrasound and photoacoustic human prostate imaging. Sci Transl Med 11(507):eaav2169
Kottmann J, Rey JM, Luginbühl J et al (2012) Glucose sensing in human epidermis using mid-infrared photoacoustic detection. Biomed Opt Express 3(4):667–680
Kruger RA (1994) Photoacoustic ultrasound. Med Phys 21:127–131
Kruger RA, Kiser WLJR, Reinecke DR et al (2003a) Thermoacoustic computed tomography using a conventional linear transducer array. Med Phys 30(5):856–860
Kruger RA, Kiser WL, Reinecke DR et al (2003b) Thermoacoustic molecular imaging of small animals. Mol Imaging 2(2):113–123
Kruger RA, Kopecky KK, Aisen AM et al (1999b) Thermoacoustic CT with radio waves: a medical imaging paradigm. Radiology 211(1):275–278
Kruger RA, Kuzmiak CM, Lam RB et al (2013) Dedicated 3D photoacoustic breast imaging. Med Phys 40:113301
Kruger RA, Lam RB, Reinecke DR et al (2010) Photoacoustic angiography of the breast. Med Phys 37:6096–6100
Kruger RA, Liu P (1994) Photoacoustic ultrasound: pulse production and detection of 0.5% Liposyn. Med Phys 21:1179–1184
Kruger RA, Liu P, Fang Y et al (1995) Photoacoustic ultrasound (PAUS)—reconstruction tomography. Med Phys 22(10):1605

Kruger RA, Miller KD, Reynolds HE et al (2000) Breast cancer in vivo: contrast enhancement with thermoacoustic CT at 434 MHz-feasibility study. Radiology 216:279–283
Kruger RA, Reinecke DR, Kruger GA (1999a) Thermoacoustic computed tomography--technical considerations. Med Phys 26:1832–1837
Kruizinga P, Van Der Steen AF, De Jong N et al (2014) Photoacoustic imaging of carotid artery atherosclerosis. J Biomed Opt 19:110504
Krumholz A, Shcherbakova DM, Xia J et al (2014) Multicontrast photoacoustic in vivo imaging using near-infrared fluorescent proteins. Sci Rep 4:3939
Krumholz A, Vanvickle-Chavez SJ, Yao J et al (2011) Photoacoustic microscopy of tyrosinase reporter gene in vivo. J Biomed Opt 16(8):080503
Ku G, Wang X, Xie X et al (2005) Imaging of tumor angiogenesis in rat brains in vivo by photoacoustic tomography. Appl Opt 44(5):770–775
Kumavor PD, Alqasemi U, Tavakoli B et al (2013) Co-registered pulse-echo/photoacoustic transvaginal probe for real time imaging of ovarian tissue. J Biophotonics 6(6–7):475–484
Lan B, Liu W, Wang Y et al (2018) High-speed widefield photoacoustic microscopy of small-animal hemodynamics. Biomed Opt Express 9(10):4689
Landa FJO, Penacoba SR, de Espinosa FM et al (2019) Four-dimensional optoacoustic monitoring of tissue heating with medium intensity focused ultrasound. Ultrasonics 94:117–123
Larina IV, Larin KV, Esenaliev RO (2005) Real-time optoacoustic monitoring of temperature in tissues. J Phys D Appl Phys 38(15):2633–2639
Laser Institute of America (2007) American National Standard for safe use of lasers. In: ANSI Z136, vol 1–2007. American National Standards Institute, Inc., New York, NY
Laufer J, Jathoul A, Pule M et al (2013) In vitro characterization of genetically expressed absorbing proteins using photoacoustic spectroscopy. Biomed Opt Express 4:2477–2490
Laufer J, Johnson P, Zhang E et al (2012a) In vivo preclinical photoacoustic imaging of tumor vasculature development and therapy. J Biomed Opt 17:056016. https://doi.org/10.1117/1.JBO.17.5.056016
Laufer J, Norris F, Cleary J et al (2012b) In vivo photoacoustic imaging of mouse embryos. J Biomed Opt 17:061220. https://doi.org/10.1117/1.JBO.17.6.061220
Lediju Bell MA, Guo X, Song DY et al (2015b) Transurethral light delivery for prostate photoacoustic imaging. J Biomed Opt 20:036002
Lediju Bell MA, Ostrowski AK, Li K et al (2015a) Localization of transcranial targets for photoacoustic-guided endonasal surgeries. Photo-Dermatology 3:78–87
Li Y, Chen J, Chen Z (2020) Multimodal intravascular imaging technology for characterization of atherosclerosis. J Innov Opt Heal Sci 13(1):2030001
Li Y, Gong X, Liu C et al (2015) High-speed intravascular spectroscopic photoacoustic imaging at 1000 A-lines per second with a 0.9-mm diameter catheter. J Biomed Opt 20(6):065006
Li Y, Lin R, Liu C et al (2018b) In vivo photoacoustic/ultrasonic dual-modality endoscopy with a miniaturized full field-of-view catheter. J Biophotonics 11(10):e201800034
Li G, Maslov KI, Wang LV (2013) Reflection-mode multifocal optical-resolution photoacoustic microscopy. J Biomed Opt 18(3):030501
Li ML, Oh JT, Xie X et al (2008c) Simultaneous molecular and hypoxia imaging of brain tumors in vivo using spectroscopic photoacoustic tomography. P IEEE 96(3):481–489
Li R, Phillips E, Wang P et al (2016) Label-free in vivo imaging of peripheral nerve by multispectral photoacoustic tomography. J Biophotonics 9(1–2):124–128
Li L, Shemetov AA, Baloban M et al (2018a) Small near-infrared photochromic protein for photoacoustic multi-contrast imaging and detection of protein interactions in vivo. Nat Commun 9(1):2734
Li ML, Wang JC, Schwartz JA et al (2009) In-vivo photoacoustic microscopy of nanoshell extravasation from solid tumor vasculature. J Biomed Opt 14(1):010507
Li PC, Wang CR, Shieh DB et al (2008b) In vivo photoacoustic molecular imaging with simultaneous multiple selective targeting using antibody-conjugated gold nanorods. Opt Express 16(23):18605–18615
Li C, Yang JM, Chen R et al (2014) Urogenital photoacoustic endoscope. Opt Lett 39:1473–1476

Li L, Zemp RJ, Lungu G et al (2007) Photoacoustic imaging of lacZ gene expression in vivo. J Biomed Opt 12:020504. https://doi.org/10.1117/1.2717531
Li L, Zhang HF, Zemp RJ et al (2008a) Simultaneous imaging of a lacZ-marked tumor and microvasculature morphology in vivo by dual-wavelength photoacoustic microscopy. J Innov Opt Health Sci 1:207–215
Li L, Zhu L, Ma C et al (2017) Single-impulse panoramic photoacoustic computed tomography of small-animal whole-body dynamics at high spatiotemporal resolution. Nat Biomed Eng 1:0071
Lin L, Hu P, Shi J et al (2018) Single-breath-hold photoacoustic computed tomography of the breast. Nat Commun 9:2352
Lin J, Wang S, Huang P et al (2013) Photosensitizer-loaded gold vesicles with strong plasmonic coupling effect for imaging-guided photothermal/photodynamic therapy. ACS Nano 7(6):5320–5329
Lin L, Yao J, Li L et al (2016) In vivo photoacoustic tomography of myoglobin oxygen saturation. J Biomed Opt 21(6):61002. https://doi.org/10.1117/1.JBO.21.6.061002
Ma R, Distel M, Deán-Ben XL et al (2012) Non-invasive whole-body imaging of adult zebrafish with optoacoustic tomography. Phys Med Biol 57(22):7227–7237
Ma J, Shi J, Hai P et al (2016) Grueneisen relaxation photoacoustic microscopy in vivo. J Biomed Opt 21(6):66005
Ma R, Taruttis A, Ntziachristos V et al (2009) Multispectral optoacoustic tomography (MSOT) scanner for whole-body small animal imaging. Opt Express 17:21414–21426
Manohar S, Kharine A, Van Hespen JC et al (2004) Photoacoustic mammography laboratory prototype: imaging of breast tissue phantoms. J Biomed Opt 9:1172–1181
Manohar S, Kharine A, Van Hespen JC et al (2005) The Twente photoacoustic mammoscope: system overview and performance. Phys Med Biol 50:2543–2557
Manohar S, Razansky D (2016) Photoacoustics: a historical review. Adv Opt Photonics 8(4):586–617
Manohar S, Vaartjes SE, Van Hespen JC et al (2007) Initial results of in vivo non-invasive cancer imaging in the human breast using near-infrared photoacoustics. Opt Express 15:12277–12285
Maslov K, Stoica G, Wang LV (2005) In vivo dark-field reflection-mode photoacoustic microscopy. Opt Lett 30(6):625–627
Maslov K, Zhang HF, Hu S et al (2008) Optical-resolution photoacoustic microscopy for in vivo imaging of single capillaries. Opt Lett 33:929–931
Matsumoto Y, Asao Y, Yoshikawa A et al (2018) Label-free photoacoustic imaging of human palmar vessels: a structural morphological analysis. Sci Rep 8:786
Matthews TP, Zhang C, Yao DK et al (2014) Label-free photoacoustic microscopy of peripheral nerves. J Biomed Opt 19:16004
Mehrmohammadi M, Yoon SJ, Yeager D et al (2013) Photoacoustic imaging for cancer detection and staging. Curr Mol Imaging 2:89–105
Mercep E, Deán-Ben XL, Razansky D (2018) Imaging of blood flow and oxygen state with a multi-segment optoacoustic ultrasound array. Photo-Dermatology 10:48–53
Miranda C, Barkley J, Smith B (2018) Intrauterine photoacoustic and ultrasound imaging probe. J Biomed Opt 23(4):1–9
Moustakidis S, Omar M, Aguirre J et al (2019) Fully automated identification of skin morphology in raster-scan optoacoustic mesoscopy using artificial intelligence. Med Phys 46(9):4046–4056
Murray TW, Haltmeier M, Berer T et al (2017) Super-resolution photoacoustic microscopy using blind structured illumination. Optica 4(1):17–22
Nagae K, Asao Y, Sudo Y et al (2019) Real-time 3D photoacoustic visualization system with a wide field of view for imaging human limbs. F1000Research 7:1813
Nasiriavanaki M, Xia J, Wan H et al (2014) High-resolution photoacoustic tomography of resting-state functional connectivity in the mouse brain. Proc Natl Acad Sci U S A 111:21–26
Nie L, Chen X (2014) Structural and functional photoacoustic molecular tomography aided by emerging contrast agents. Chem Soc Rev 43:7132–7170
Ning B, Sun N, Cao R et al (2015) Ultrasound-aided multi-parametric photoacoustic microscopy of the mouse brain. Sci Rep 5:18775

Ntziachristos V (2010) Going deeper than microscopy: the optical imaging frontier in biology. Nat Methods 7(8):603–614
Ntziachristos V, Pleitez MA, Aime S, Brindle KM (2019) Emerging technologies to image tissue metabolism. Cell Metab 29(3):518–538
Nuster R, Slezak P, Paltauf G (2014) High resolution three-dimensional photoacoustic tomography with CCD-camera based ultrasound detection. Biomed Opt Express 5(8):2635
Oh JT, Li ML, Zhang HF et al (2006) Three-dimensional imaging of skin melanoma in vivo by dual-wavelength photoacoustic microscopy. J Biomed Opt 11(3):34032
Omar M, Aguirre J, Ntziachristos V (2019) Optoacoustic mesoscopy for biomedicine. Nat Biomed Eng 3:354–370
Omar M, Rebling J, Wicker K et al (2017) Optical imaging of post-embryonic zebrafish using multi orientation raster scan optoacoustic mesoscopy. Light Sci Appl 6:e16186
Oraevsky A, Andreev V, Karabutov A et al (1999) "Laser optoacoustic imaging of the breast: detection of cancer angiogenesis", Proc SPIE 3597, Optical Tomography and Spectroscopy of Tissue III, 352–363
Oraevsky AA, Esenaliev RO, Karabutov AA (1997) "Laser optoacoustic tomography of layered tissue: signal processing", Proc SPIE 2979, Optical Tomography and Spectroscopy of Tissue: Theory, Instrumentation, Model, and Human Studies II, 59–70
Oraevsky AA, Jacques SL, Esenaliev RO et al (1994a) Time-resolved optoacoustic imaging in layered biological tissues. Advances in optical imaging and photon migration 21:161–165
Oraevsky AA, Jacques SL, Esenaliev RO et al (1994b) "Laser-based optoacoustic imaging in biological tissues", Proc SPIE 2134, Laser-Tissue Interaction V; and Ultraviolet Radiation Hazards, 122–8
Oraevsky AA, Jacques SL, Tittel FK (1993) "Determination of tissue optical properties by piezoelectric detection of laser-induced stress waves", Proc SPIE 1882, Laser-Tissue Interaction IV, 86–101
Pan D, Pramanik M, Senpan A et al (2010) Near infrared photoacoustic detection of sentinel lymph nodes with gold nanobeacons. Biomaterials 31:4088–4093
Paproski RJ, Forbrich AE, Wachowicz K et al (2011) Tyrosinase as a dual reporter gene for both photoacoustic and magnetic resonance imaging. Biomed Opt Express 2(4):771–780
Paproski RJ, Heinmiller A, Wachowicz K et al (2014) Multi-wavelength photoacoustic imaging of inducible tyrosinase reporter gene expression in xenograft tumors. Sci Rep 4:5329
Pavlova NN, Thompson CB (2016) The emerging hallmarks of cancer metabolism. Cell Metab 23(1):27–47
Perekatova V, Subochev P, Kleshnin M et al (2016) Optimal wavelengths for optoacoustic measurements of blood oxygen saturation in biological tissues. Biomed Opt Express 7(10):3979–3995
Pleitez MA, Khan AA, Soldà A et al (2020) Label-free metabolic imaging by mid-infrared optoacoustic microscopy in living cells. Nat Biotechnol 38(3):293–296
Pleitez MA, Lieblein T, Bauer A et al (2013) In vivo noninvasive monitoring of glucose concentration in human epidermis by mid-infrared pulsed photoacoustic spectroscopy. Anal Chem 85(2):1013–1020
Pramanik M, Wang LV (2009) Thermoacoustic and photoacoustic sensing of temperature. J Biomed Opt 14:054024
Qin C, Cheng K, Chen K et al (2013) Tyrosinase as a multifunctional reporter gene for photoacoustic/MRI/PET triple modality molecular imaging. Sci Rep 3:1490
Qu Y, Li C, Shi J et al (2018) Transvaginal fast-scanning optical-resolution photoacoustic endoscopy. J Biomed Opt 23(12):1–4. https://doi.org/10.1117/1.JBO.23.12.121617
Razansky D, Buehler A, Ntziachristos V (2011) Volumetric real-time multispectral optoacoustic tomography of biomarkers. Nat Protoc 6:1121–1129
Razansky D, Distel M, Vinegoni C et al (2009) Multispectral opto-acoustic tomography of deep-seated fluorescent proteins in vivo. Nat Photonics 3(7):412
Ripoll J, Koberstein-Schwarz B, Ntziachristos V (2015) Unleashing optics and optoacoustics for developmental biology. Trends Biotechnol 33:679–691

Sethuraman S, Aglyamov SR, Amirian JH et al (2007) Intravascular photoacoustic imaging using an IVUS imaging catheter. IEEE Trans Ultrason Ferroelectr Freq Control 54(5):978–986
Sethuraman S, Amirian JH, Litovsky SH et al (2008) Spectroscopic intravascular photoacoustic imaging to differentiate atherosclerotic plaques. Opt Express 16(5):3362–3367
Shah J, Park S, Aglyamov S et al (2008) Photoacoustic imaging and temperature measurement for photothermal cancer therapy. J Biomed Opt 13:034024
Shami VM, Kahaleh M (eds) (2010) Endoscopic ultrasound, 1st edn. Humana Press, Totowa, NJ. Imprint: Humana
Shi J, Wong TTW, He Y et al (2019) High-resolution, high-contrast mid-infrared imaging of fresh biological samples with ultraviolet-localized photoacoustic microscopy. Nat Photonics 13:609
Song L, Maslov K, Wang LV (2011) Multifocal optical-resolution photoacoustic microscopy in vivo. Opt Lett 36(7):1236–1238
Song KH, Stein EW, Margenthaler JA et al (2008) Noninvasive photoacoustic identification of sentinel lymph nodes containing methylene blue in vivo in a rat model. J Biomed Opt 13:054033. https://doi.org/10.1117/1.2976427
Sowers T, Emelianov S (2018) Exogenous imaging contrast and therapeutic agents for intravascular photoacoustic imaging and image-guided therapy. Phys Med Biol 63(22):22TR01
Steeg PS (2006) Tumor metastasis: mechanistic insights and clinical challenges. Nat Med 12:895–904
Stein EW, Maslov KI, Wang LV (2009a) Noninvasive, in vivo imaging of blood-oxygenation dynamics within the mouse brain using photoacoustic microscopy. J Biomed Opt 14(2):020502
Stein EW, Maslov KI, Wang LV (2009b) Noninvasive, in vivo imaging of the mouse brain using photoacoustic microscopy. J Appl Phys 105(10):102027
Stoffels I, Morscher S, Helfrich I et al (2015) Metastatic status of sentinel lymph nodes in melanoma determined noninvasively with multispectral optoacoustic imaging. Sci Transl Med 7:317ra199
Stritzker J, Kirscher L, Scadeng M et al (2013) Vaccinia virus-mediated melanin production allows MR and optoacoustic deep tissue imaging and laser-induced thermotherapy of cancer. Proc Natl Acad Sci U S A 110(9):3316–3320
Swierczewska M, Choi KY, Mertz EL et al (2012) A facile, one-step nanocarbon functionalization for biomedical applications. Nano Lett 12(7):3613–3620
Tang J, Dai X, Jiang H (2016) Wearable scanning photoacoustic brain imaging in behaving rats. J Biophotonics 9:570–575
Tang J, Xi L, Zhou J et al (2015b) Noninvasive high-speed photoacoustic tomography of cerebral hemodynamics in awake-moving rats. J Cereb Blood Flow Metab 35:1224–1232
Tang M, Zhou Y, Zhang R et al (2015a) Noninvasive photoacoustic microscopy of methemoglobin in vivo. J Biomed Opt 20(3):036007
Taruttis A, Herzog E, Razansky D et al (2010) Real-time imaging of cardiovascular dynamics and circulating gold nanorods with multispectral optoacoustic tomography. Opt Express 18:19592–19602
Taruttis A, Morscher S, Burton NC et al (2012) Fast multispectral optoacoustic tomography (MSOT) for dynamic imaging of pharmacokinetics and biodistribution in multiple organs. PLoS One 7(1):e30491
Taruttis A, van Dam GM, Ntziachristos V (2015) Mesoscopic and macroscopic optoacoustic imaging of cancer. Cancer Res 75(8):1548–1559
Tearney GJ, Brezinski ME, Bouma BE et al (1997) In vivo endoscopic optical biopsy with optical coherence tomography. Science 276:2037–2039
Toi M, Asao Y, Matsumoto Y et al (2017) Visualization of tumor-related blood vessels in human breast by photoacoustic imaging system with a hemispherical detector array. Sci Rep 7:41970
Tsyboulski D, Conjusteau A, Oraevsky A (2014) "Dual modality optoacoustic and laser ultrasound endoscopy system", Proc SPIE 8943, Photons Plus Ultrasound: Imaging and Sensing 2014, 89432S https://doi.org/10.1117/12.2044424
Tzoumas S, Nunes A, Olefir I et al (2016) Eigenspectra optoacoustic tomography achieves quantitative blood oxygenation imaging deep in tissues. Nat Commun 7:12121

van den Berg PJ, Daoudi K, Steenbergen W (2015) Review of photoacoustic flow imaging: its current state and its promises. Photo-Dermatology 3(3):89–99
van den Berg PJ, Daoudi K, Steenbergen W (2016) Pulsed photoacoustic flow imaging with a handheld system. J Biomed Opt 21(2):26004
van Soest G, Marcu L, Bouma BE et al (2017) Intravascular imaging for characterization of coronary atherosclerosis. Curr Opin Biomed Eng 3:1–12
Viator JA, Komadina J, Svaasand LO et al (2004) A comparative study of photoacoustic and reflectance methods for determination of epidermal melanin content. J Invest Dermatol 122(6):1432–1439
Viator JA, Paltauf G, Jacques SL et al (2001) "Design and testing of an endoscopic photoacoustic probe for determination of treatment depth after photodynamic therapy," Proc SPIE 4256, Biomedical Optoacoustics II, 16–27
Vilov S, Arnal B, Bossy E (2017) Overcoming the acoustic diffraction limit in photoacoustic imaging by the localization of flowing absorbers. Opt Lett 42(21):4379–4382
Wang LV (2008) Prospects of photoacoustic tomography. Med Phys 35(12):5758–5767
Wang LV (2009) Photoacoustic imaging and spectroscopy. CRC, Boca Raton
Wang LV, Hu S (2012) Photoacoustic tomography: in vivo imaging from organelles to organs. Science 335:1458–1462
Wang X, Ku G, Wegiel MA et al (2004b) Noninvasive photoacoustic angiography of animal brains in vivo with near-infrared light and an optical contrast agent. Opt Lett 29(7):730–732
Wang P, Ma T, Slipchenko MN et al (2014b) High-speed intravascular photoacoustic imaging of lipid-laden atherosclerotic plaque enabled by a 2-kHz barium nitrite raman laser. Sci Rep 4:6889
Wang L, Maslov K, Wang LV (2013) Single-cell label-free photoacoustic flowoxigraphy in vivo. Proc Natl Acad Sci U S A 110:5759–5764
Wang X, Pang Y, Ku G et al (2003) Noninvasive laser-induced photoacoustic tomography for structural and functional in vivo imaging of the brain. Nat Biotechnol 21:803–806
Wang X, Roberts WW, Carson PL et al (2010a) Photoacoustic tomography: a potential new tool for prostate cancer. Biomed Opt Express 1:1117–1126
Wang B, Su JL, Karpiouk AB et al (2010b) Intravascular photoacoustic imaging. IEEE J Sel Top Quantum Electron 16:588–599
Wang X, Xie X, Ku G et al (2006) Noninvasive imaging of hemoglobin concentration and oxygenation in the rat brain using high-resolution photoacoustic tomography. J Biomed Opt 11(2):024015
Wang Y, Xie X, Wang X et al (2004a) Photoacoustic tomography of a nanoshell contrast agent in the in vivo rat brain. Nano Lett 4(9):1689–1692
Wang B, Yantsen E, Larson T et al (2009) Plasmonic intravascular photoacoustic imaging for detection of macrophages in atherosclerotic plaques. Nano Lett 9:2212–2217
Wang L, Zhang C, Wang LV (2014a) Grueneisen relaxation photoacoustic microscopy. Phys Rev Lett 113(17):174301
Weber J, Beard PC, Bohndiek SE (2016) Contrast agents for molecular photoacoustic imaging. Nat Methods 13:639–650
Weis SM, Cheresh DA (2011) Tumor angiogenesis: molecular pathways and therapeutic targets. Nat Med 17(11):1359–1370
Weissleder R, Pittet MJ (2008) Imaging in the era of molecular oncology. Nature 452:580–589
Weissleder R, Schwaiger MC, Gambhir SS et al (2016) Imaging approaches to optimize molecular therapies. Sci Transl Med 8(355):355ps16
Welch AJ, van Gemert MJC (2011) Optical-thermal response of laser-irradiated tissue. Springer; 2 edition (January 15, 2011)
Wilson KE, Bachawal SV, Tian L et al (2014) Multiparametric spectroscopic photoacoustic imaging of breast cancer development in a transgenic mouse model. Theranostics 4(11):1062–1071
Wilt BA, Burns LD, Wei Ho ET et al (2009) Advances in light microscopy for neuroscience. Annu Rev Neurosci 32:435–506

Wissmeyer G, Pleitez MA, Rosenthal A et al (2018) Looking at sound: optoacoustics with all-optical ultrasound detection. Light Sci Appl 7:53
Wu M, Springeling G, Lovrak M et al (2017) Real-time volumetric lipid imaging in vivo by intravascular photoacoustics at 20 frames per second. Biomed Opt Express 8(2):943–953
Xia J, Li G, Wang L et al (2013) Wide-field two-dimensional multifocal optical-resolution photoacoustic-computed microscopy. Opt Lett 38(24):5236–5259
Xiong K, Wang W, Guo T et al (2019) Shape-adapting panoramic photoacoustic endomicroscopy. Opt Lett 44(11):2681
Xu Z, Li CH, Wang LV (2010) Photoacoustic tomography of water in phantoms and tissue. J Biomed Opt 15(3):036019. https://doi.org/10.1117/1.3443793
Xu M, Wang LV (2006a) Photoacoustic imaging in biomedicine. Rev Sci Instrum 77:041101
Xu Y, Wang LV (2006b) Rhesus monkey brain imaging through intact skull with thermoacoustic tomography. IEEE Trans Ultrason Ferroelectr Freq Control 53:542–548
Yang JM, Chen R, Favazza C et al (2012b) A 2.5-mm diameter probe for photoacoustic and ultrasonic endoscopy. Opt Express 20:23944–23953
Yang JM, Favazza C, Chen R et al (2012a) Simultaneous functional photoacoustic and ultrasonic endoscopy of internal organs in vivo. Nat Med 18:1297–1302
Yang JM, Li C, Chen R et al (2014) Catheter-based photoacoustic endoscope. J Biomed Opt 19:066001
Yang JM, Li C, Chen R et al (2015) Optical-resolution photoacoustic endomicroscopy in vivo. Biomed Opt Express 6(3):918–932
Yang Y, Li X, Wang T et al (2011) Integrated optical coherence tomography, ultrasound and photoacoustic imaging for ovarian tissue characterization. Biomed Opt Express 2(9):2551–2561
Yang JM, Maslov K, Yang HC et al (2009) Photoacoustic endoscopy. Opt Lett 34:1591–1593
Yang X, Skrabalak SE, Li ZY et al (2007) Photoacoustic tomography of a rat cerebral cortex in vivo with au nanocages as an optical contrast agent. Nano Lett 7(12):3798–3802
Yao J, Kaberniuk AA, Li L et al (2015a) Multiscale photoacoustic tomography using reversibly switchable bacterial phytochrome as a near-infrared photochromic probe. Nat Methods 13:67–73
Yao J, Ki M, Zhang Y et al (2011) Label-free oxygen-metabolic photoacoustic microscopy in vivo. J Biomed Opt 16:076003. https://doi.org/10.1117/1.3594786
Yao J, Maslov KI, Shi Y et al (2010b) In vivo photoacoustic imaging of transverse blood flow by using Doppler broadening of bandwidth. Opt Lett 35:1419–1421
Yao DK, Maslov K, Shung KK et al (2010a) In vivo label-free photoacoustic microscopy of cell nuclei by excitation of DNA and RNA. Opt Lett 35:4139–4141
Yao J, Wang LV (2014a) Sensitivity of photoacoustic microscopy. Photo-Dermatology 2:87–101
Yao J, Wang LV (2014b) Photoacoustic brain imaging: from microscopic to macroscopic scales. Neurophotonics 1(1):1877516
Yao J, Wang L, Li C et al (2014) Photoimprint photoacoustic microscopy for three-dimensional label-free subdiffraction imaging. Phys Rev Lett 112(1):014302
Yao J, Wang L, Yang JM et al (2015b) High-speed label-free functional photoacoustic microscopy of mouse brain in action. Nat Methods 12:407–410
Yao J, Xia J, Maslov KI et al (2013) Noninvasive photoacoustic computed tomography of mouse brain metabolism in vivo. NeuroImage 64:257–266
Yaseen MA, Ermilov SA, Brecht HP et al (2010) Optoacoustic imaging of the prostate: development toward image-guided biopsy. J Biomed Opt 15:021310. https://doi.org/10.1117/1.3333548
Yuan Y, Yang S, Xing D (2010) Preclinical photoacoustic imaging endoscope based on acousto-optic coaxial system using ring transducer array. Opt Lett 35:2266–2268
Yun SH, Kwok SJJ (2017) Light in diagnosis, therapy and surgery. Nat Biomed Eng 1:0008
Yun SH, Tearney GJ, Vakoc BJ et al (2006) Comprehensive volumetric optical microscopy in vivo. Nat Med 12:1429–1433
Zhang EZ, Beard PC (2011) "A miniature all-optical photoacoustic imaging probe", Proc SPIE 7899, Photons Plus Ultrasound: Imaging and Sensing 2011, 78991F

Zhang HF, Maslov K, Stoica G et al (2006a) Functional photoacoustic microscopy for high-resolution and noninvasive in vivo imaging. Nat Biotechnol 24:848–851

Zhang HF, Maslov K, Stoica G et al (2006b) Imaging acute thermal burns by photoacoustic microscopy. J Biomed Opt 11(5):054033

Zhang C, Maslov K, Wang LV (2010) Subwavelength-resolution label-free photoacoustic microscopy of optical absorption in vivo. Opt Lett 35:3195–3197

Zhang C, Maslov K, Yao J et al (2012) In vivo photoacoustic microscopy with 7.6-μm axial resolution using a commercial 125-MHz ultrasonic transducer. J Biomed Opt 17(11):116016

Zhang X, Zhang HF, Puliafito CA et al (2011) Simultaneous in vivo imaging of melanin and lipofuscin in the retina with photoacoustic ophthalmoscopy and autofluorescence imaging. J Biomed Opt 16(8):080504

Zhang C, Zhang YS, Yao DK et al (2013) Label-free photoacoustic microscopy of cytochromes. J Biomed Opt 18(2):20504

Zhou Y, Zhang C, Yao DK et al (2012) Photoacoustic microscopy of bilirubin in tissue phantoms. J Biomed Opt 17(12):126019